2003

Synchrotron radiation as a probe of chemical information using novel experimental configurations

George Farquar
Louisiana State University and Agricultural and Mechanical College, gfarqu1@lsu.edu

SYNCHROTRON RADIATION AS A PROBE OF CHEMICAL INFORMATION USING NOVEL EXPERIMENTAL CONFIGURATIONS

A Dissertation

Submitted to the Graduate Faculty of the
Louisiana State University and
Agricultural and Mechanical College
In partial fulfillment of the
Requirements for the degree of
Doctor of Philosophy

In

The Department of Chemistry

By
George R. Farquar
B.S., Humboldt State University, 1997
December 2003

Acknowledgements

I have had an abundance of professional relationships at Louisiana State University over the past six years. If I began to credit those that have been of a great assistance in my scientific endeavors, I would inevitability make regrettable omissions. For all that played a part in this dissertation your assistance has made this document possible.

Dr. Hannah D. Farquar, my wife, is the greatest thing I discovered as a graduate student. Hannah, you have made me smile, dream, and aspire to new heights over the past few years. Without you I would not have been able to tolerate the occasional misfortunes or snafu of graduate school. Hannah, you have given me more support than I could ever ask for. I cannot express in words what you mean to me. I hope a story will suffice. Once in Nicaragua I took your passport and stuffed a bill into it. Along with mine I handed it over to an "agent of the government", in order to expedite our border crossing. You had a look of fear and faith that I will never forget, fear of the unknown and faith that all will be fine. I have the same feeling every day with you. Let us begin a new adventure and with you by my side I know it will have a beautiful outcome.

As this is a chemistry dissertation I must thank those responsible for my deoxyribonucleic acid (DNA). Although it is not always true, in this case two halves do make a whole. I (literately) would not be here without you. Putting chemistry aside my money is on nurture. Thank you.

Table of Contents

List of Figures

List of Equations

Abstract

Determination of chemical information with synchrotron radiation is an area of great scientific interest, and expanding the range of available techniques is the topic of this dissertation. The experimental methods described herein allows for a significant advancement of the availability of subtle chemical information. This dissertation uses ionizing radiation to study three chemical systems.

First, the *l*=3 shape resonance in CO is investigated using a cryogenically cooled gas jet. Shape resonant effects have been studied for many years. Previously, this was accomplished on the vibrational structure of molecules with a limited ability to determine the rotational substructure effects. A dramatic increase in the ability to determine shape resonant effects is shown as a direct result of the reduction in gas temperature.

Second, the ability to use X-ray spectroscopic data to determine the composition of mixed metal oxidation states of significant environmental consequence is described. The major advancement is a combination of *in-situ* data collection with novel data reduction techniques. Results from this study demonstrate that X-ray spectroscopy is a powerful probe of surface reactions relevant to combustion problems.

Finally, the separation of ions with the same chemical composition from two different parent ions is necessary to determine the lineage of the molecule. Preliminary results are presented that demonstrate the ability of a novel use of a time of flight velocity map imaging apparatus to focus a zero energy ion event with mass information. In addition a demonstration of the resolution obtainable is shown, along with the ability to determine the components of a mixture of gases in the range of less than 1%. Eventual applications will allow the study of reactive species such as clusters created in gas jets.

Chapter 1: Introduction

This dissertation focuses on the use of tunable ionizing radiation to learn detailed information regarding molecular systems. It describes three related experiments that use novel techniques to determine chemical information using synchrotron radiation. Many years of research into the advancement of synchrotron radiation techniques has been accomplished for a wide range of fields. The range of disciplines using synchrotron radiation is too large to cover completely but examples include: X-ray near edge spectroscopy[1.1], medicine[1.2], geology[1.3], surface science[1.4], polymer science[1.5], lithography[1.6] and crystallography.[1.7] This dissertation is an extension of prior work conducted by the Poliakoff group.[1.8-18] The contribution of novel methods and instrumentation is of such importance that experimental science has supported a peer-reviewed journal on the subject for over 70 years (*Review of Scientific Instruments*). As with other published works using relatively new techniques, the scope is broader than experimental goals of using a single technique for information gathering and rather focuses on enlarging the horizons of experimental capabilities. The advancements presented include an application of liquid nitrogen cooling to enhance energy dependent rotational structure of molecular photoions (Chapter 2), *in-situ* determination of copper speciation using X-ray absorption on a system of environmental significance (Chapter 3) and the design and construction of a time of flight zero kinetic energy velocity map imaging system (Chapter 4). The following chapters are all related by the new use of ionizing radiation to understand “cutting edge” topics in chemistry.

Chapter 2 studies the ionization process itself, by looking at the internal energy distribution of photoions as the ionizing photon energy is increased. Previous studies were unable to show a substantial change in the populated rotational levels.[1.12] This lack of an effect was attributed to the relatively hot target molecules (18 K). In the current work the target states are reduced through the use of a liquid nitrogen cooled nozzle. This cooling reduced the rotational temperature of the target molecules to 9 K. The results are compared with theory to show that the rotational effects are the result of a $4\sigma \rightarrow k\sigma$ shape resonance.

Chapter 3 uses ionizing radiation to determine the chemical composition of a complex mixture of copper that accelerates the rate of dioxin formation. A sample containing copper (II) oxide was exposed to a known dioxin precursor and elevated to a 375 °C. The procedure simulated the combustion process and allowed for an *in- situ* time dependent measurements of the rate of copper reduction. Along with the percent composition of copper species (Cu(II), Cu(I) and Cu(0)), an analysis of the rate of formation is presented.

Chapter 4 discusses the design and construction of a new instrument, using ionizing radiation, to ultimately determine the spectroscopy and ionizing process for a complex mixture of samples. Included in the design is a discussion on the simulation of the ion optics needed for time of flight and velocity map imaging design. Future experiments using this apparatus are outlined, along with preliminary results verifying the simulations for the ion optic components.

The remainder of this chapter describes the common themes required for the studies. Section 1.1 outlines the scientific background when using ionizing radiation for

these studies. Following the spectroscopic background the introduction lists and describes the common themes required for the use of synchrotron radiation, including a brief history and properties of synchrotron radiation and an overview of detection methods that can be employed for gaining chemical information. In addition, a discussion on vacuum considerations and wavelength selection are included.

1.1 Molecule Photon Interactions

When a photon interacts with a molecule, the photon is either absorbed or scattered. Photon scattering is utilized in X-ray diffraction, not a principal component of this work, and will not be discussed further. Photon absorption leads to a change in the energy of the target molecule and careful observation of the energetics of processes initiated by this absorption can yield valuable information on the state of the target molecule. The experiments presented in this manuscript focus on absorption near or above the binding energy of the electron. Three possible outcomes of an above-threshold photon molecule interaction are shown below (Figure 1.1). The first outcome, fluorescence (A), occurs when a molecule is excited into an ionic state and then relaxes through fluorescence. The second outcome (B) is fragmentation, where the ionized molecule splits into one neutral and one ionic fragment. The final outcome, (C), is the ejection of an electron, as in the other pathways, but without the emission of a fluorescent photon or fragmentation. Pathways A, B and C all involve ejection of an electron, however very different spectroscopic techniques are required for the detection of fluorescence and electrons. Figure 1.1 demonstrates that with an ionization event different products occur and complementary information can be determined.

Fluorescence $AB(v_0=0,\{N_0\}) + h\nu_{exc} \rightarrow$

$$AB^+(v^+, N^+) + e^-$$
$$\downarrow$$
$$AB^+(v'', N'') + h\nu_{v^+v''N^+N''} \quad (A)$$

Fragmentation: $AB + h\nu_{exe} \rightarrow A + B^+ + e^-$ (B)

Ejection of an electron: $AB + h\nu_{exe} \rightarrow AB^+ + e^-$ (C)

Figure 1.1 Three possible outcomes of an above threshold photon molecule interaction. The first pathway (A) occurs when a molecule is placed into an ionic excited state and relaxes through fluorescence. A "0" subscript denotes a target level undergoing ionization, and a double-prime superscript is used to describe the lower level in the fluorescence transition. The notation $\{N_0\}$ indicates that there is a thermal distribution of populated target rotational levels. The second pathway (B) results in a relaxation pathway where the molecule is fragmented. Third (C) is the direct ejection of an electron as in pathway A but without a resulting photon.

In each of these processes, data collection and interpretation vary, depending upon the information desired. The following discussion will be broken down into the origin of the ejected electron, with specifics to follow in the related chapters. The experiments described in Chapter 2 focus on pathway (A); by determining the rotational population resulting from the ionization step, a deeper understanding of the mechanism of electron ejection can be obtained. Specifically, the change in rotational distributions for CO is shown to be the result of a $4\sigma \rightarrow k\sigma$ shape resonance. Chapter 3 involves all three pathways, with detection based on the changes in the photon intensity to determine the chemical species in a complex mixture. The final chapter will describe a combination of pathways B and C to disentangle complicated spectra that are a superposition of simple spectra by using a newly-constructed time-of -flight velocity map imaging detector.

Characterization of photons resulting from fluorescence after the ejection of a valence electron yields rotational and vibrational spectra. Fluorescence mapped as a function of incident photon energy in pathway (A), allows for a deeper understanding of the photoelectron ejection process. It is commonly assumed that the ejection of a photoelectron is rapid compared to the nuclear motion of the molecule. This assumption limits any interaction between nuclear and electronic degrees of freedom resulting from photoionization. Many examples of the failure of this simplification are present in the literature. [1.13-16,1.19-21] In fact, as the photoelectron is ejected it samples the ionic core of the system. A direct measurement of the ejected photoelectron is possible with photoelectron spectroscopy , but is typically restricted to vibrationally resolved spectra. Other techniques such as resonantly enhanced multiphoton ionization are also able to obtain rotationally resolved information, however they are limited in the energy range of the ejected photoelectron that is accessible.[1.22,1.23] This restriction is due to the ultrahigh resolution necessary for rotationally resolved studies. Recent work conducted by the Poliakoff group is challenging the idea that useful photoelectron data can be collected only near the ionization threshold.[1.24] The work outlined in Chapter 2 uses the "trick" of dispersed fluorescence detection to determine the state of an excited ion. By detecting the fluorescence of an excited ion the detection and excitation bandwidth are decoupled yielding rotationally resolved spectra. Interpretation of the resulting fluorescence data is complicated, generally beyond the scope of experimentalists, but a positive consequence of this difficulty has been highly productive collaborations with theorists. Chapter 2 has essential theoretical contributions from V. Mcoy (California Institute of Technology).

By increasing the energy of the ionizing radiation to that required to eject core electrons, more direct interpretation of chemical systems is possible. Core electronic transitions are defined as the ejection of a 1s, 2s or 2p electron (for elements below the second row), and these transitions are referred to as K- and L-edges. These transitions are normally the most intense when the binding energy of the electron and incident photon are equal, resulting in a zero kinetic energy photoelectron. Historically these transitions were termed "white lines", from the intense exposure on photographic film. The two 1s electrons are degenerate (indistinguishable) resulting in a single K-edge for each element, but the non-degenerate L-edge transitions result in three distinct transitions (L_I, L_{II} and L_{III},) corresponding to the 2s, $2p_{1/2}$, and $2p_{3/2}$ electron ejections. The K- and L-edges vary by the oxidation state of the system.[1.1] As the oxidation state increases the energy required to eject an electron also increases. This effect is easily explained; more energy is required to remove an electron from an atom with a higher positive charge. All of these transitions are dependent on the dipole selection rules where $\Delta l = \pm 1$. The K- and L- edge ionization potentials are also quadratic in their relationship to atomic number (Figure 1.2). The increase in ionization potential for elements allows for highly specific elemental transitions to be studied over a large energy range. Entangled in the K- and L-edge transition intensities is a wealth of information ranging from the oxidation state to local chemical geometry. Oxidation states can be determined with XANES (X-ray Absorption Near Edge Spectroscopy)[1.25] and geometry is determined by analyzing EXAFS (Extended X-ray Absorption Fine Structure). The energy range of EXAFS is larger than that of XANES and EXAFS data sets contain the XANES region.

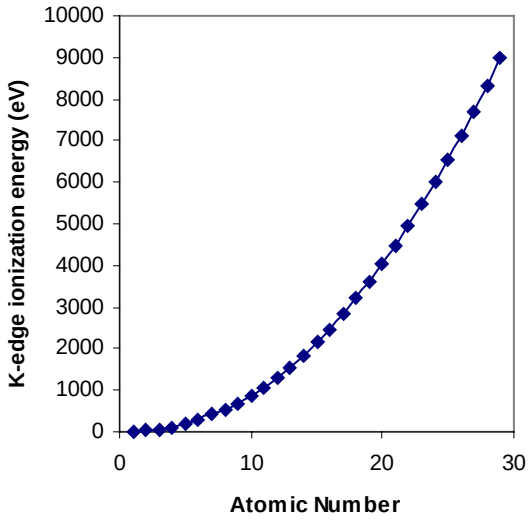

Figure 1.2 The quadratic dependence of atomic number on K-edge ionization energy.

XANES spectra are collected from approximately 50 eV below threshold to 200 eV beyond the white line. In practice, interpretation of XANES is conducted primarily by comparison to reference spectra. This “fingerprinting" technique permits accurate oxidation state and concentration determination. Different chemical species will have a different fingerprint due to backscattering from neighbors and electron shielding (altering the ionization potential). In the near-edge region the ejected electrons have low kinetic energies and multiple back-scattering processes can occur. Multiple back-scattering processes complicate the direct analysis of XANES spectra.[1.26-28] Independent of “fingerprinting”, oxidation states can be directly determined by the position of the white line: oxidized species will have a higher binding energy than the elemental form.[1.1] Just below threshold in XANES spectra is a region where transitions to bound states give direct information about the unoccupied valence orbitals.

Extending several hundred volts beyond the XANES spectral region is the EXAFS region. EXAFS spectral features result from backscattering from surrounding atoms. The backscattering from the energetic EXAFS electrons do not undergo multiple backscattering and make interpretation possible. After ionization the outgoing photoelectron and the backscattered photoelectron from adjacent atoms interact and interfere and in turn create a ripple in absorption spectra that is interpretable in terms of the wavelength (i.e. energy) of the photoelectron. The clearest example of backscattering comes from the comparison of a noble gas such as argon and a species such as an argon cluster. The monatomic argon spectrum appears unstructured in the EXAFS region as no backscattering can occur,[1.29] but as clusters form the number of backscattering species increase with cluster size, producing an EXAFS spectrum with more pronounced ripples. Backscattering also increases significantly by atomic number. By using well-defined analysis procedures that involve Fourier transforms, and comparisons to modeled molecular systems, a highly accurate representation of bond distances is possible.[1.30]

The instrument that has been designed and constructed in Chapter 4 will employ ionization pathways B and C in combination with experimental techniques used in Chapter 2. The goal is focused on the same principles of XANES and EXAFS techniques with a species separation based on the fragmentation of excited ions. By mapping the zero kinetic energy species (non-fragmented) and the exploded fragments, identical chemical species can be separated by molecular origin. For example a cluster in a mixture of clusters of varying size is currently indistinguishable by its molecular origin. Ultimately this apparatus will allow an expansion of spectroscopy by effectively removing the background signal from an unwanted species in a complex mixture. This is

significant in that currently there is no technique to distinguish the origin of a single component arising from a complex mixture that yields identical chemical species.

1.2 Synchrotron Radiation

The first observation of synchrotron radiation occurred at General Electric Research Laboratory in Schenectady, New York, in 1947.[1.31] The theory of synchrotron radiation was originally developed independently by Iwaneko[1.32] of the Soviet Union in 1944 and Schwinger[1.33] of the United States in 1945. Three years later synchrotron radiation was used to explain non-thermal radiation in astronomy.[1.34] The history of synchrotron radiation is as old as the Universe; however, man has only controlled this aspect of nature for less than a century. The evolution of synchrotron radiation use is broken down into three generations of facilities.[1.35] First generation sources were not originally designed to produce usable light but were intended for high-energy particle physics experiments. The use of first generation facilities for radiation studies is termed "parasitic" in nature. The parasitic nature is from the secondary purpose of light production. As the demand continued to grow for dedicated use facilities, second and third generation storage rings were developed. Second and third generation facilities are similar in that they were constructed solely for the production of user light, yet they differ mainly in the brightness of the radiation and the use of insertion devices. Although second generation sources are able to use insertion devices they are not optimized to use insertion devices. The Louisiana State University facility, the Center for Advanced Microstructures and Devices (CAMD)[1.36], is a second generation storage ring. All of the experiments in this document have been designed for use and carried out at or in support

of work conducted at CAMD. The following discussion on light production will be specific to bending and wiggler magnet radiation.

1.2.1 Properties and Production of Synchrotron Radiation

Synchrotron radiation has several unique attributes not found in conventional light sources such as hot filaments and discharge tubes. Unlike conventional VUV and X-ray sources a synchrotron source does not have a line structure and is continuously variable over the entire spectrum emitted by the facility. Synchrotron radiation is bright, polarized and tunable over a wide energy range. There are several texts that cover the theoretical consideration in detail for synchrotron radiation.[1.37,1.38]

It is well known that acceleration of a charged particle results in electromagnetic radiation.[1.39] The most common example of radiation from an accelerated particle is observed daily in the production of radio waves from an antenna. When the charged particle is at relativistic energies and following a curved path, the spectrum of emitted radiation will be shifted to higher energies and appear in a tangent to the radius of curvature. Synchrotron facilities of today are composed of a polygon with bending magnets at the corners to accelerate the electrons around the corners (Figure 1.3). The modern shape allows for a smaller radius of curvature than a circle of the same diameter would and straight sections can be used for insertion devices. The two types of insertion devices are wigglers and undulators, which are placed in the straight sections of a storage ring. Wigglers are wavelength shifters and undulators are intensity amplifiers.[1.37] A wiggler is similar to a bending magnet in that it accelerates the electron a single time or a few times, although through a higher magnetic field and more dramatic radius of curvature. Undulators cause the electrons to travel through a series of periodic magnetic

fields. This periodic acceleration alters the produced X-rays though constructive and destructive interference yielding a high intensity source at selectable wavelengths. For an undulator the wavelengths are selected by altering the distance between the poles of the magnets. The use of polygon storage rings also compresses the radiated photons to small regions of the facility at the corners therefore increasing the photon flux per unit area. The areas of maximum photon flux are the tangent of the curvature for bending magnets and the ends of the straight sections in the case of wigglers. Beamlines are placed at the regions of maximum photon flux. Aside from the storage ring and bending magnets several other components are necessary for the production of synchrotron radiation. These include a source for charged particles, a means to initially accelerate the particles to relativistic energies, bending magnets or insertion devices and an RF cavity to restore the energy lost due to radiation. Other components such as quadrupoles are used as electron focusing optics in many storage rings.

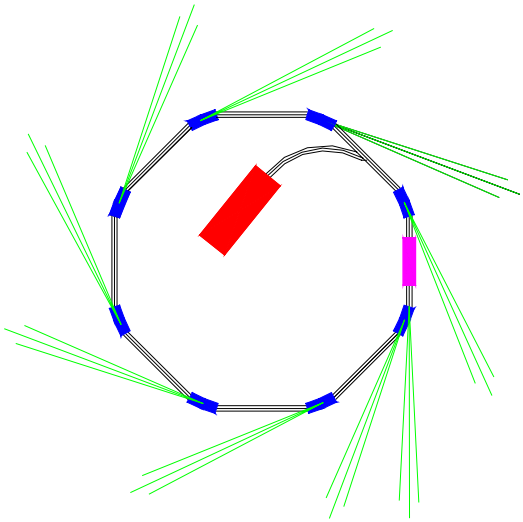

Figure 1.3 Diagram of a synchrotron showing the linear accelerator (red), bending magnets (blue), insertion device (magenta), the resulting X-rays (green). The straight sections contain RF cavities and electron focusing optics.

The journey of an electron at the CAMD storage ring begins with its creation and initial acceleration in the linear accelerator (LINAC). The linear accelerator imparts energies that would be unattainable by a single conventional electric field. This acceleration is accomplished through a series of oscillating electric and magnetic fields in the frequency range know as radio frequency to increase the energy to a value in the MeV range (200 MeV at CAMD). The accelerated electrons are then injected into the storage ring. Once the electrons are injected into the storage ring they are ramped to the final energy. The bending magnets or insertion devices convert the electron kinetic energy into photons by applying the law of conservation of energy. The radiated photon energy must be equal to a loss in electron energy. To prevent the electrons from "winding down" as the energy is lost a standing radio frequency (RF) wave is employed to restore the loss of energy. As a byproduct of the standing wave the electrons are separated into bunches, with the electrons on the leading edge of the wave gaining less energy than those on the trailing edge. Experiments that need fast pulses (picosecond) exploit the property of bunching. The electrons travel a distance of 54 meters in a single revolution and have a bunch length of 2 cm at CAMD. At the speed of light a bunch pulse of light is on the order of 60 ps.

In order to compare storage ring facilities and their relative output, a value called the critical photon energy is used. A universal curve for photon flux is also a useful measure of the relative output of a storage ring. Both bending magnet radiation and wiggler radiation are described by the critical photon energy. The critical photon energy is defined as the dividing line at which half of all radiated power will fall above and half will fall below (Equation 1.1).[1.37] In Equation 1.1 E_e is in joules for the rest energy of an

electron and in GeV when simplified for the ring energy of the electron. It is important to note that the critical photon energy is not the dividing line where one half of the number of photons will fall on both sides but rather the radiated power of the photons is half of the total emitted power.

$$\lambda_c(nm) = \frac{0.559R(m)}{E^3(GeV)} \text{ or}$$

$$E_c(J) = h\nu_c = \frac{3e\hbar B(T)\gamma^2}{2m_e} \text{ where } \gamma = \frac{E_e(J)}{mc^2} \text{ or}$$

$$E_C(keV) = 0.6650E_e^2(GeV)B(T)$$

Equation 1.1 Critical photon energy of synchrotron radiation.[1.37]

CAMD currently uses a storage ring energy of 1.3 GeV and a bending magnet field of 1.47 Tesla yielding critical energy of 1.66 keV. The critical photon energy is a useful measure to determine the upper end of practical excitations for a given facility. At four times the critical photon energy, the photon flux of the emitted radiation drops to approximately 10% of the critical energy flux. For CAMD the value of $4E_c$ is 6.64 keV corresponding to the ejection of a Manganese 1s electron. The value of $4E_c$ is only a guidepost and it is possible to conduct experiments at energies above this point but with increasing difficulty in data collection. From the critical energy the total distribution of photons can be calculated (Equation 1.2).[1.37] To calculate the total distribution of photons, solved values of the universal curve, $G_{1,}$ are corrected for ring current and

storage ring energy. The current storage ring conditions for CAMD are 1.3 GeV (storage ring energy) and 100 mA (stored current). These values and tabulated values of G_1 (Appendix A) can be used to create a photon flux curve (Figure 1.4). Figure 1.3 shows that there is a gradual transition in photon flux from energy to energy with a smooth variation of photon flux.

$$\frac{photons/s}{mrad \ * (0.1\% BW)} = 2.46 * 10^{13} E_e(GeV) I(A) G_1(E/E_c)$$

Equation 1.2 Photons per second per mrad for 0.1% relative spectral bandwidth created from the universal curve G_1 corrected for ring current I, and ring energy E_e.[1.37]

The term white light is used to describe a source with a continuous range of photon energies. It is important to note from the form of Equation 1.2 that a change in the ring current will result in a directly proportional increase or decrease of photon flux at a given energy. This proportional relationship indicates that small changes in the stored ring current will not appreciably alter the photon flux. The low relative change in photon flux is important, as the ring current on a given day should have very little effect on the practicality of an experiment. In order to change the flux curve dramatically for a bending magnet a change in the storage ring energy is needed as can be seen in the cubed term in Equation 1.1. CAMD currently operates at single storage ring energy and the higher energy photons are limited to the current values at the bending magnet beam lines. If higher energies are needed another facility should be used with a higher critical energy.

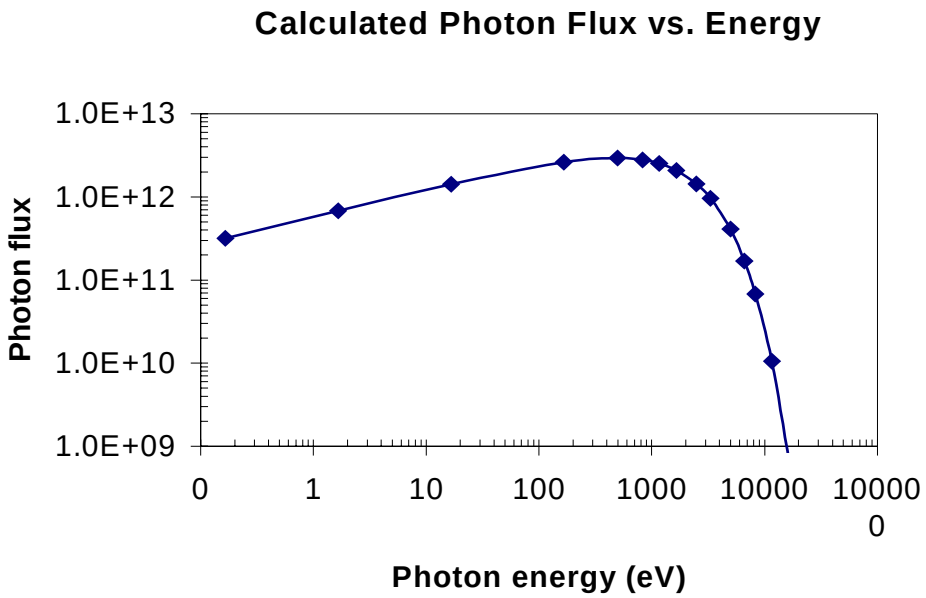

Figure 1.4 Photon flux calculated from Equation 1.2 for typical conditions at CAMD.

1.3 Experimental Considerations for Use with Synchrotron Radiation

Utilization of synchrotron radiation for nearly all experiments requires optimization of monochromators, vacuum conditions, and the selection of a suitable detection method. Good vacuum technique insures that no damage occurs to the facility and a given experiment may not be possible due to contamination if high vacuum is not attained. Finally, this section will cover a brief background of some possible detection methods used for photon molecule interactions.

1.3.1 Monochromators and Beamlines

Beamlines contain all of the necessary optical components for wavelength selection. A monochromator disperses the white light into selectable energies. Monochromators are located in beamlines along with other optical components.

Beamlines can range in complexity from a window in the storage ring to diagnose the ring status to systems with multiple optical components. Typically beamlines that house monochromators have entrance and exit slits and mirrors to direct the photons to the experimental chamber. Low energy beamlines require a high vacuum to reduce interactions with gas molecules. In addition organics could possibly contaminate the optical components and reduce the efficiency. Optical components typically use grazing incidence optical components because with a high angle of incidence the radiation would not be directed but absorbed.

The two principal kinds of monochromators in wide use are crystals and gratings. For low-energy wavelength selection, grating monochromators are used while for high photon energies a crystal monochromator is needed. Grating and crystal monochromators rely on interference to accomplish energy dispersion. A holographic process is used to produce most modern gratings where a series of lines are etched into a photo resist. The areas of exposure are then dissolved and replaced by a reflective surface. The use of holographic etching has improved the quality and reduced the price of high quality gratings.[1.40] Equation 1.3 defines the conditions needed for constructive interference. As can be seen in Equation 1.3 several conditions exist for integer multiples of λ for a given diffraction angle of *r*, leading to higher order light throughput. A diagram of a grating and monochromatic light is shown in Figure 1.5.

$$n\lambda = d(\sin i + \sin r)$$

Equation 1.3 Conditions for constructive interference for a grating.[1.40]

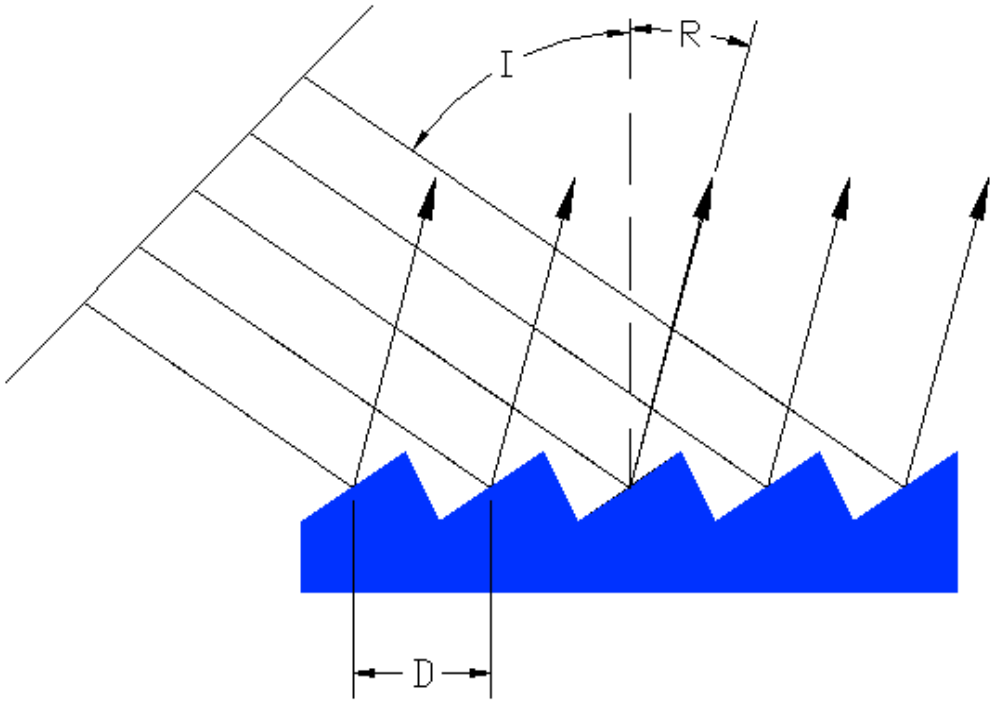

Figure 1.5 Grating with incident monochromatic light.

Bragg developed crystal monochromators in 1912. The operation and wavelength selection are dictated by the Bragg equation (Equation 1.4). In the Bragg equation d is the interplanar spacing of the crystal, θ is the angle of incident and reflected light, and n must be an integer. In practice, the use of Bragg's law is for an ideal case and it does not take into account the loss of intensity due to scattering processes. The use of a single crystal for monochromatic light, although possible, has a serious drawback in that the monochromatic light is displaced in direction, which would require the sample to move in space around the monochromator as energy is changed. To overcome this

difficulty, a second reflection from another parallel crystal provides a fixed exit position for the monochromatic light. In practice a single set of crystals has a finite range of photon energies that can be monochromatized. This range is limited by the angle of the crystal to the incident radiation. This angular dependence is known as the rocking curve. The rocking curve equation is shown in Equation 1.5. The limited range of photons for a given set of crystals dictates that they be changed when a large range (several thousand eV) of photon energies is required. The large energy range of photons available allow XANES and EXAFS data to be collected with a single set of crystals.

$$n\lambda = 2d\sin\theta$$

Equation 1.4 Bragg's law for X-ray wavelength selection.

$$\omega = \frac{2}{Sin2\theta}\frac{r_0\lambda^2}{\pi V}C\mid F_h \mid e^{-m} \qquad \text{where}$$

$$r_0 = \frac{e^2}{mc^2}$$

Equation 1.5 The rocking curve equation for a double crystal monochromator. V=unit cell volume of the crystal, λ is the reflected radiation wavelength, θ_B = the Bragg angle, e^{-m} = the Debeye Waller Factor, and C is the polarization factor.[1.35]

Three monochromators were used to accomplish this work at CAMD. The monochromator used for the rotational studies in Chapter 2 was the plane grating monochromator (PGM).[1.41] Monochromators are rated by the energy range and resolving power (energy/Δenergy). The PGM has a low energy range and a resolving power of 1000. The XANES studies discussed in Chapter 3 were conducted on the double crystal monochromator beamline (DCM); the DCM is capable of monochromatizing over the

energy range of 1-15 keV with a resolution of 0.5 eV at low energies to 2 eV at high energies.[1.42] The experiments of the final chapter use the 6 m toroidal grating monochromator (TGM)[1.43] that has resolving power of 2000 and is effective over the energy range of 15-300 eV, respectively.

Beamline components do not transmit all of the incident photons to the experiment. The efficiency of beamlines varies with the number of optical components. The experiments in Chapters 2, 3 and 4 each use a different beamline with varying efficiencies. The double crystal monochromator beamline (DCM) used in chapter 3 has the least number of optical elements and will be used to demonstrate a calculation of beamline efficiency. The optical elements include an entrance aperture, a beam position detector, entrance slits, monochromator and a window. The efficiency of DCM beamline can easily be determined for the conditions in Chapter 3. The conditions for the DCM are 10^8 photons/s collected with a bandwidth equal to 2eV at 9000 eV. The DCM beamline receives 2 mrad of incident photons from the storage ring. This converts to approximately $1*10^{11}$ photons /s at 9000 eV (Figure 1.4). By converting the photon flux collected to a 0.1% spectral bandwidth yields $5*10^9$ photons/s at the experimental chamber. The final beamline efficiency is 5 percent. Beamlines with more optical elements will naturally have a lower efficiency.

1.3.2 Vacuum Techniques

Vacuum technique is the primary consideration when planning a synchrotron radiation experiment. In order to maintain the storage ring electrons and protect the beamline optics from contaminants, an ultra high vacuum (UHV) is required on the order of $1x10^{-9}$ Torr. The ring current will have a reduced lifetime due to electron collisions

with gas molecules if this pressure is not maintained. There is also the possibility of organic contaminants collecting on the beamline optics if UHV is not maintained. Contaminants degrade the efficiency of the optics. If the experiment requires pressures above this, methods must be employed to allow a pressure differential from the experimental chamber to the beam line. The two methods commonly used are differential pumping and a transmission window, both of which have advantages and drawbacks.

Of the two methods used for obtaining pressure differential, windows are the easiest to implement. The windows employed in this work have been selected for experimental conditions on both ends of this range. The second consideration in selecting a widow is the transmission profile for a given material. When working in the hard X-ray region a window composed of a carbon polymer is the most suitable. Polymers have a transmission profile relatively flat at high energies and strong physical properties. The high strength allows for experiments to be conducted at atmosphere while maintaining the required beam line pressure. In the low energy range window selection must be more rigorous. Various absorption edges must be taken into account in order to find the material that is best suited for the given situation. A plot of two common window materials (aluminum and polyimide) is shown in Figure 1.6. When the two window materials are compared it is clear that at low energies aluminum will have a greater transmission than polyimide. The transmission cut off at 72.5 eV for aluminum corresponds to an L-edge transmission and the sharp decrease in polyimide at 284 eV is due to the carbon K-edge, therefore the spectral characteristics must be taken into account for specific experimental concerns. There is no energy range that cannot be windowed

for with proper selection of materials. A table of K- and L-edges is included in Appendix A for elements of atomic number 1-40.

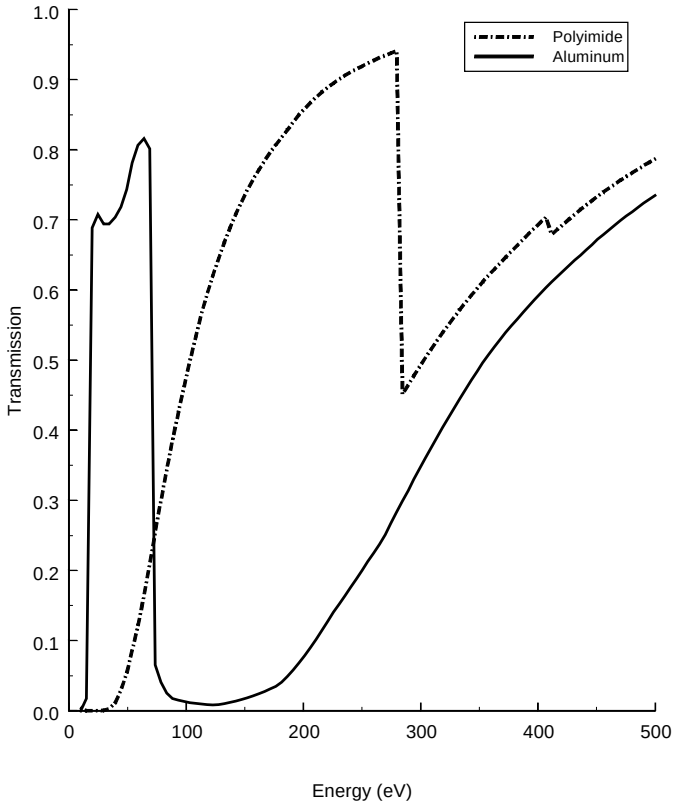

.

Figure 1.6 Transmission for 1500 Å polyimide and aluminum windows.[1.44]

There are many situations when transmission windows are not practical due to the need for a large spectral coverage or a possible chemical reaction with the sample and window material. Conditions where a large energy range is needed for an experiment require a differential pumping system. Differential pumping is accomplished through the use of conductance barriers and a series of pumping stages. Differential pumping is most

effective in the low energy range where the materials for conductance barriers will have a high amount of internal reflection. Although it would be possible to achieve a significant pressure differential with pumping alone, the cost for the pumps and the space requirement would be prohibitive. The fundamental relationships for pumping speed calculations are shown in Equations 1.5, 1.6, 1.7 and 1.8. An extensive body of work on vacuum techniques has been summarized by Dushman.[1.45,1.46] In a differential pumping situation the gas load is dependent on the conductance of the transfer line and pressure of the chamber. By reducing the gas apertures the required pumping speed is dramatically reduced. The incident photon profile from the beam line is of a finite size much smaller than the standard high vacuum flanges. In order to optimize the system a compromise of pumping speed and gas aperture needs to be selected. To reduce the pumping speed requirement a small aperture is required

$$Q(\textit{Torr l/sec}) = S(\textit{l/sec}) * P(\textit{Torr})$$

Equation 1.6 Pumping speed equation, where Q = gas load, S = pumping speed and P = pressure.

$$C(\textit{l/sec}) = 12D^{3}(\textit{cm}) * L^{-1}(\textit{cm})$$

Equation 1.7 Conductance of tube of length L with diameter D, for air at 20 °C.[1.47]

$$C_a = 3.7(T/M)^{1/2}A$$

Equation 1.8 Conductance of a thin aperture: A= area in cm, M is the molar mass.

$$1/S_{effective}=1/S +1/C$$

Equation 1.9 The effective pumping speed of a system with a rated pump of speed S and a conductance C.

The Poliakoff lab currently uses a differential pumping system able to maintain a differential of five to six orders of magnitude. Specifics of the differential pumping employed by the Poliakoff lab will be discussed in Chapter 2. In Appendix B sample calculations are shown for the differential pumping system used in Chapter 2. The above equations are also useful in determining the base pressure of a theoretical system. If a window or differential pumping is used there are a few common requirements to achieve a UHV on the beam line side of the experiment.

In order to achieve a UHV care must be given to several factors not needed in higher-pressure operations. Cleanliness is essential because any oil, such as residual machine oil or that exuding from the skin, will slowly degas, degrading the final desired pressure. Careful cleaning of all parts is required to eliminate machine oils, and the use of latex gloves is required for all operations that may transfer skin oil to the chamber. Once the vacuum has a pressure of ~$1x10^{-7}$ Torr adsorbed species begin to degas from the vacuum chamber walls and limit the rate of pressure drop. The majority of adsorbed molecules are water. To reduce the time needed to achieve UHV a technique called "baking" is used. In a typical bake for the experiments in Chapter 2 and 4 the temperature of the apparatus being employed is raised to 120 $^{\circ}$C. This temperature is well above the boiling point of water yet below the temperature where non-metallic

gaskets will decompose. Once the pressure has fallen to within ten times the desired pressure the bake is turned off. After several hours as the residual gas atoms adsorb onto the now-cooling oven walls, the pressure falls to the desired level ($1x10^{-9}$ Torr) and the beamline can be opened to the experiment.

1.3.3 Detection Methods

In order to collect data over a range of experimental conditions several detection methods are possible. It is important to evaluate the available detection methods and determine the most suitable for a given situation. As described in Figure 1.1, there are three possible photon/molecule interactions to detect. The change in photon flux, fluorescence, ejected electrons, and the energies and trajectories of ions created by the interaction can be measured, each yielding slightly different information related to the interaction. In these experiments detection methods can be combined into groups. Change in photon flux and fluorescence are considered photon detection and electrons and ions can be grouped into charged particle detection.

1.3.3.1 Photon Detection

Transmission determines the relative change in photon intensity before and after a sample, described by the ratio of transmitted to incident light. Historically this method has been employed in some of the most common spectrometers used in labs. The Spec 20 is a commercially available instrument found in most undergraduate chemistry and biology labs and employs the technique of transmission. The traditional model requires a measurement with a sample in place and then a reference measurement to determine the transmission of the sample. Photon detection methods include ion chambers, charged coupled devices, photomultipliers and photodiodes.

Ion chambers are an excellent choice for X-rays. They allow a large percentage of the photons to pass without being absorbed and have a linear response with respect to photon energy.[1.40] When using X-rays it is possible to take both measurements simultaneously. This is accomplished by using a series of ion chambers. Ion chambers consist of a pair of plates with a small (~100 V) voltage across them separated by a gas filled gap. The most common gas is atmospheric nitrogen. Nitrogen has a relatively low cross section in the hard X-ray region and flat absorption profile. When a more sensitive measure is needed a heavy noble gas such as krypton can be used. When a sufficiently energetic photon enters the ion chamber a small percentage will interact with a gas molecule. When this occurs an ion electron pair is formed causing a current across the plates. The ejected electrons have a high kinetic energy and when traveling to the collector plate collide with other gas molecules, yielding an amplification of approximately 100 times. This current is recorded to give a direct indication of the incident photon flux. If a second ion chamber is placed after the sample the sample transmission can be determined. To determine the absorption the negative log of the initial over the final photon flux is taken (Equation 1.10).[1.40]

$$A = -\log \frac{I_o}{I_f}$$

Equation 1.10 Relationship between absorption and transmission.

Photomultiplier tubes, photodiodes and charged coupled devices are similar in that the photons must be absorbed completely and are terminal in the usefulness of the photons. Photomultiplier tubes are based on a photosensitive material that ejects

electrons upon excitation by an incident photon. These electrons are then accelerated to a dynode that in turn ejects multiple electrons for each incident electron. The dynode process is repeated several times yielding a typical amplification of 10^6 for every incident photon. Photodiodes have a variety of design possibilities. The most basic consists of a material that when struck by incident photons allows a current proportional to the photon flux to flow. There is a wide range of detectors available with a large range of quantum efficiencies. Typically charged coupled devices have the highest quantum yield (~80% for high end devices) ranging to a few percent for photomultiplier tubes. Photomultiplier tubes are typically sensitive from 100-700 nm and CCDs are typically sensitive from 100-2000 nm.

Charged coupled devices (CCD) are becoming more common for use in light detection. Major advancements in the available technology have been driven by the consumer electronics market. CCDs consist of a two-dimensional array of photosensitive capacitors. The incident light hits the array and a charge is stored for each detected photon. This charge is then read out in two possible modes. The standard method to collect data is energy versus intensity, where all of the y values from the array are added to create the spectral intensity. It is also possible to limit the spatial range of the collected data through software allowing for a sorting or windowing of the incident photons with respect to location of the interaction. In Chapter 2 the method of windowing is used to collect the center of a supersonic expansion to enhance the rotational cooling of carbon monoxide. It is also possible to use a CCD in three-dimensional mode where the y position information is retained.

1.3.3.2 Charged Particle Detection

When the chemical species of interest is a charged particle a micro channel plate (MCP) or MCP stack is used. A MCP is a series of miniature electron multipliers oriented parallel to each other. MCPs are formed out of lead glass.[1.48] This technology is an advancement of earlier devices called dynodes.[1.49] The channels in the plates range from 10-100 μm and are oriented at an angle of approximately 8° from the surface normal. When a bias of ~1000 V is applied across a plate a high gain electron multiplier is created. Two plates can be placed in a chevron stack to increase the gain. Typical gain for a single plate for a single charged particle is 10^4 and for a chevron stack the gain is 10^6. When using an MCP vacuum considerations are needed. Due to the high potential across the plates a discharge can occur if the pressure is above 10^{-4} Torr, possibly destroying the plates. MCPs have the advantage of excellent detection efficiency for both electrons and ions. MCPs can also be used for fast neutrals and energetic photons. For electrons and ions with energies of 50 eV the detection efficiency is approximately 50 percent.

1.4 References

1.1 Stohr, J. *NEXAFS Spectroscopy*; Sprnger-Verlag: Berlin, 1991; 403.

1.2 Suortti, P.; Thomlinson, W. Medical applications of synchrotron radiation. *Physics in Medicine and Biology* **2003**, *48*, R1-R35.

1.3 Hirschmugl, C. Applications of storage ring infrared spectromicroscopy and reflection-absorption spectroscopy to geochemistry and environmental science. *Reviews in Mineralogy and Geochemistry* **2002**, *49*, 317-339.

1.4 Gunther, S.; Kaulich, B.; Gregoratti, L. Photoelectron microscopy and applications in surface and materials science. *Progress in Surface Science* **2002**, *70*, 187-260.

1.5 Clough, R. High-energy radiation and polymers: A review of commercial processes and emerging applications. *Nuclear Instruments & Methods in Physics Research Section B-Beam Interactions With Materials and Atoms* **2001**, *185*, 8-33.

1.6 Cerrina, F. X-ray imaging: applications to patterning and lithography. *Journal of Physics D-Applied Physics* **2000**, *33*, R103-R116.

1.7 Esposito, L.; Vitagliano, L.; Mazzarella, L. Recent advances in atomic resolution protein crystallography. *Protein and Peptide Letters* **2002**, *9*, 95-105.

1.8 Floriano, P. N.; Noble, C. O.; Schoonmaker, J. M.; Poliakoff, E. D.; McCarley, R. L. Cu(0) nanoclusters derived from poly(propylene imine) dendrimer complexes of CU(II). *Journal of the American Chemical Society* **2001**, *123*, 10545-10553.

1.9 Floriano, P. N.; Schlieben, O.; Doomes, E. E.; Klein, I.; Janssen, J. et al. "A grazing incidence surface X-ray absorption fine structure (GIXAFS) study of alkanethiols adsorbed on Au, Ag, and Cu" (vol 321, pg 175, 2000). *Chemical Physics Letters* **2000**, *327*, 447-447.

1.10 Poliakoff, E. D.; Rao, R. M. Rotational and vibrational effects in photoionization: Bridging the gap from microvolts to kilovolts. *Journal of Electron Spectroscopy and Related Phenomena* **1996**, *79*, 361-366.

1.11 Rao, R. M.; Poliakoff, E. D.; Wang, K. H.; McKoy, V. Molecular photoionization as a probe of vibrational-rotational- electronic correlations. *Journal of Chemical Physics* **1996**, *104*, 9654-9657.

1.12 Poliakoff, E. D.; Choi, H. C.; Rao, R. M.; Mihill, A. G.; Kakar, S. et al. Photoion Rotational Distributions from near-Threshold to Deep in the Continuum. *Journal of Chemical Physics* **1995**, *103*, 1773-1787.

1.13 Miller, J. S.; Poliakoff, E. D.; Miller, T. F.; Natalense, A. P. P.; Lucchese, R. R. Excitation of the symmetry forbidden bending mode in molecular photoionization. *Journal of Chemical Physics* **2001**, *114*, 4496-4504.

1.14 Miller, J. S.; Poliakoff, E. D. On the correlation between photoelectron energy and bending excitation in molecular photoionization. *Journal of Chemical Physics* **2000**, *113*, 899-902.

1.15 Rao, R. M.; Poliakoff, E. D.; Wang, K. H.; McKoy, V. Global Franck-Condon breakdown resulting from Cooper minima. *Physical Review Letters* **1996**, *76*, 2666-2669.

1.16 Wu, C. Y.; Poliakoff, E. D. Vibrationally resolved 2a(2u)(-1) photoionization of C6F6. *Chemical Physics Letters* **1998**, *292*, 167-171.

1.17 Kakar, S.; Choi, H. C.; Poliakoff, E. D. Localization of a Continuum Shape Resonance - Photoionization of Cs2. *Journal of Chemical Physics* **1992**, *97*, 4690-4696.

1.18 Kakar, S.; Choi, H. C.; Poliakoff, E. D. Rotationally Resolved Fluorescence as a Probe of Molecular Photoionization Dynamics. *Journal of Chemical Physics* **1992**, *97*, 6998-7001.

1.19 Piancastelli, M. N. The neverending story of shape resonances. *Journal of Electron Spectroscopy and Related Phenomena* **1999**, *100*, 167-190.

1.20 Holland, D. M. P.; Potts, A. W.; Karlsson, L.; Trofimov, A. B.; Schirmer, J. The influence of shape resonance phenomena on the valence shell photoionization dynamics of silicon tetrafluoride. *Journal of Physics B-Atomic Molecular and Optical Physics* **2002**, *35*, 1741-1757.

1.21 Fohlisch, A.; Hasselstrom, J.; Karis, O.; Vaterlein, P.; Martensson, N. et al. Franck-Condon breakdown in core-level photoelectron spectroscopy of chemisorbed CO. *Chemical Physics Letters* **1999**, *315*, 194-200.

1.22 Xie, Y.; Reilly, P.; Chilukuri, S.; Gordon, R. Perturbations in the Multiphoton Ionization Spectrum of the F-1-Delta State of HCL. *Journal of Chemical Physics* **1991**, *95*, 854-864.

1.23 Bean, B.; Fernandez-Alonso, F.; Zare, R. Distribution of rovibrational product states for the "prompt" reaction H+D-2(nu=0,j=0-4) -> HD(nu '=1,2,j ')+D near 1.6 eV collision energy. *Journal of Physical Chemistry A* **2001**, *105*, 2228-2233.

1.24 Rathbone, G. J.; Poliakoff, E. D.; Bozek, J. D.; Lucchese, R. R. Resonantly amplified vibronic symmetry breaking. *Journal of Chemical Physics* **2001**, *114*, 8240-8243.

1.25 Paktunc, D.; Foster, A.; Laflamme, G. Speciation and characterization of arsenic in Ketza River mine tailings using x-ray absorption spectroscopy. *Environmental Science & Technology* **2003**, *37*, 2067-2074.

1.26 Haack, N.; Ceballos, G.; Wende, H.; Baberschke, K.; Arvanitis, D. et al. Shape resonances of oriented molecules: ab initio theory and experiment on hydrocarbon molecules. *Physical Review Letters* **2000**, *84*, 614-617.

1.27 Dehmer, J. L.; Dill, D. Molecular Effects on Inner-Shell Photoabsorption - K-Shell Spectrum of N-2. *Journal of Chemical Physics* **1976**, *65*, 5327-5334.

1.28 Dehmer, J. L.; Dill, D. Shape Resonances in K-Shell Photoionization of Diatomic- Molecules. *Physical Review Letters* **1975**, *35*, 213-215.

1.29 Ruhl, E.; Heinzel, C.; Hitchcock, A. P.; Baumgartel, H. Ar 2p spectroscopy of free argon cluster. *Journal of Chemical Physics* **1993**, *98*, 2653-2663.

1.30 Teo, B. K. *EXAFS: Basic principles and data analysis*; Springer-Verlag: New York, 1986; 420.

1.31 Elder, F. R.; Gurewitsch, A. M.; Langmuir, R. V. Radiation from Electrons in a Synchrotron. *Physical Review* **1947**, *71*, 829.

1.32 Iwaneko, D.; Pomeranchuk, I. On the Maximal Energy Attainable in a Betatron. *Physical Review* **1944**, *70*, 343.

1.33 Schwinger, J. Electron Radiation in High Energy Accelerators. *Procedings of the American Physical Society*: Berkeley, 1946.

1.34 Alfven, H.; Herlofson Cosmic Radiation and Radio Stars. *Physical Review* **1950**, *78*, 616.

1.35 Koch, E. E. *Handbook on Synchrotron Radiation*; North Holand Publishing Company: New York, 1983; 606.

1.36 Craft, B.; Feldman, M.; Morikawa, E.; Poliakoff, E.; Saile, V. et al. Center for Advanced Microstructures and Devices (CAMD). *Review of Scientific Instruments* **1992**, *63*, 1561-1562.

1.37 Attwood, D. *SOFT X-RAYS AND EXTREME ULTRAVIOLET RADIATION*; Cambridge University Press: Cambridge, 2000; 470.

1.38 Thompson; Attwood, D.; Gullikson *X-Ray Data Booklet*; Lawrence Berkeley Nationl Lab: Berkeley, 2001.

1.39 Cutnell, J.; Johnson, K. Physics; 2nd ed.; John Wiley & Sons, INC.: New York, 1992; pp 695.

1.40 Skoog, D.; Leary, J. *Instrumental Analysis*; 4th ed.; Saunders College Publishing: San Diego, 1992.

1.41 Morikawa, E.; Scott, J. D.; Poliakoff, E. D.; Stockbauer, R. L.; Saile, V. Design of Soft-X-Ray Plane-Grating Monochromator for Camd. *Review of Scientific Instruments* **1992**, *63*, 1300-1304.

1.42 Schilling, P. J.; Morikawa, E.; Tolentino, H.; Tamura, E.; Kurtz, R. L. et al. Installation and Operation of the Lnls Double-Crystal Monochromator at Camd. *Review of Scientific Instruments* **1995**, *66*, 2214-2216.

1.43 Koch, K. D.; Mohan, C. V.; Erskine, J. L.; Sprunger, P. T.; Scott, J. D. CAMD 6-m toroidal grating monochromator beamline. *Nuclear Instruments & Methods in Physics Research Section a- Accelerators Spectrometers Detectors and Associated Equipment* **2002**, *483*, 821-829.

1.44 Gullikson Center for X-ray Optics http://www.cxro.lbl.gov/optical_constants/filter2.html

1.45 Dushman, S. *Scientific Foundations of Vacuum Techniques*; John Wiley and Sons: Schenectady, 1949; 882.

1.46 Lafferty, J. M. *Foundations of Vacuum Science and Techniques*; John Whiley and Sons: New York, 1998; 728.

1.47 Moore, J.; Davis, C.; Copln, M. *Building Scientific Apparatus*; CRC Press: Clevland, 1983; 483.

1.48 Wiza, J. Microchannel Plate Detectors. *Nuclear Instruments and Methods* **1979**, *162*, 587-601.

1.49 Farnsworth Electron Multiplier US Patent# 1969399

Chapter 2: Rotationally Resolved Photoionization: Influence of the $4\sigma \rightarrow k\sigma$ Shape Resonance on $CO^+(B^2\Sigma^+)$ Rotational Distributions

2.1 Introduction

This chapter focuses on experimental results obtained for the rotational distributions of $CO^+(B^2\Sigma^+)$ photoions, made possible by a novel use of a cryogenically cooled supersonic expansion gas jet. Data were collected using synchrotron radiation as an ionization source with dispersed fluorescence as the detection method. The use of dispersed fluorescence is able to determine rotational data over a wide range of ionization energies. Other techniques that are used to obtain rotationally and vibrationally resolved data include photoelectron spectroscopy, resonantly enhanced multiphoton ionization (REMPI), and zero-kinetic-energy pulsed field ionization (ZEKI-PFI). ZEKI-PFI and REMPI are limited to threshold ionization and are not suitable for energy dependent studies.[2.1-5] One of the components studied with photoionization experiments is the breakdown of the Franck-Condon approximation for vibrational degrees of freedom. The Franck-Condon principle predicts that vibrational spectra will not change with a change in the ionization energy. The predicted lack of change is based on the assumption that the time scale for vibrational motion is much greater than the time required for an electron to be ejected.

Molecular photoionization is frequently dominated by a single partial wave in localized regions of the ionization continuum. The outgoing photoelectron partial wave components were calculated and show a strong shape $l = 3$ resonance at 35 eV. An outgoing photoelectron wave is broken down into its angular momentum components to obtain the partial wave ($l = 0,1,2,3\ldots$) components. Because of the coupling between the

angular momentum of the photoelectron and that of molecular rotation during photoionization, measurements of rotational distributions provide insight into the dynamics of the photoelectron escape, i.e., the angular momentum composition of the continuum wavefunction as well as the exchange of angular momentum between the photoelectron and the ion core.[2.6,27] The conservation of angular momentum in the ion core is limited by $\Delta J = J^{+}\text{-}J_0 = (l+3/2),(l+1/2),\ldots,-(l+3/2)$.[2.8] When excluding electronic spin, $\Delta N = N^{+}\text{-}N_0 = (l+1),l,\ldots,-(l+1)$. The total change in J for a system is limited to ±1 and 0. With large values of *l* for an electron, the ion can have large values of J and N. The results section shows that the change in rotational structure is due to an *f*-wave ($l = 3$) giving rise to changes in ΔN as large a 4.[2.9] The changes seen in the experimental data are compared to the results of the calculations allowing the identification of the partial waves responsible for the changes in the experimental spectra. Previously in the Poliakoff group an expansion of the vibrational studies were performed to determine the underlying rotational structure for N_2 and CO.[2.9-11] Previous studies demonstrated that with increasing ionization energy the N_2 rotational population decreased for rotational levels 0-2 and increased for levels 3-5, however no dramatic change was observed in the CO rotational structure with respect to the ionization energy. This result was surprising due to the fact that both CO and N_2 are isoelectronic. With the two molecules having the same electronic configuration it would be expected that a similar process would affect the outgoing photoelectron.

The two effects being studied are the cooper minima and shape resonance. A cooper minima reduces the ionization cross-section and a shape resonance increases the ionization cross-section. In a shape resonance the outgoing photoelectron is temporarily

trapped by a potential barrier and eventually escapes. In particular, it was shown that rotational distributions in N_2 photoionization were strongly influenced by Cooper minima in the $l = 2$ partial wave of the $2\sigma_u \rightarrow k\sigma_g$ channel over a 250 eV range. Shape resonant effects were also present in CO, however the effects were not dramatic. An interesting result from those previous studies was that the rotationally resolved characteristics of N_2 $2\sigma_u^{-1}$ and CO $4\sigma^{-1}$ photoionization were qualitatively different, which was unexpected for these valence isoelectronic systems. The differences were attributed to qualitative differences in their ionization continua. In the case of N_2, there are Cooper minima in the N_2 $2\sigma_u \rightarrow k\sigma_g$ channel at high energies ($h\nu_{exc} > 100$ eV) but no shape resonances, while the situation is reversed for CO, i.e., there is a shape resonance but no Cooper minima. The differences in the ionization continua are attributed to the differences in the partial wave contributions. Calculation for N_2 show a large reduction in the $l = 2$ and $l = 4$ partial wave at high energies. For CO the calculations showed an increase in $l = 3$ partial wave component. The N_2 partial wave reduction was attributed to a Cooper minima and the CO partial wave increase was consistent with a shape resonance. This lack of a conspicuous marker for rotational consequences of a shape resonance was attributed to the relatively hot target molecules ($T_0 \approx 18$ K), which washed out the effects of the shape resonance. The effects on the rotational population will be distributed over the total number of populated target rotational states. By reducing the rotational temperature any shape resonant effects will be amplified by reducing the number of target states.

Vibrational spectra have components of both vibrational and rotational transitions. As the resolution is increased for a vibrational spectrum a large substructure of rotational transitions becomes evident. The rotational transitions consist of two subcategories called "branches". This rotationally resolved study focuses on the effects of the temporary trapping of an out-going photoelectron as it escapes the molecular core, known as a shape resonance.[2.12-15] Shape resonances have the practical effect of amplifying the cross-section of the ionization with respect to energy. High amplitudes in the partial wave of a photoelectron can enhance large ΔN transitions.[2.9] This amplification can have the practical effect of increasing intensity of rotational peaks as the energy increases.

Processes in the ionization continuum frequently span a wide spectral range. For example, Cooper minima[2.16-18] and shape resonances[2.12-15,219-22] typically extend over ranges of 10-50 eV, so it is desirable to study rotational distributions over a comparable energy range. The excitation and fluorescence sequence that was employed for the current study is summarized by Figure 2.1.

$$\mathrm{CO}(X\,^1\Sigma^+, v_0 = 0, \{N_0\}) + h\nu_{exc} \rightarrow \mathrm{CO}^+(B\,^2\Sigma^+, v^+, N^+) + e^-$$

$$\downarrow$$

$$\mathrm{CO}^+(X\,^2\Sigma^+, v'', N'') + h\nu_{v^+v''N^+N''} \quad (1)$$

Figure 2.1 Fluorescence pathway. A "0" subscript denotes a target level undergoing ionization, and a double-prime superscript is used to describe the lower level in the fluorescence transition. The notation $\{N_0\}$ indicates that there is a thermal distribution of populated target rotational levels.

A key aspect of dispersed fluorescence measurements is that the detection bandwidth is decoupled from the excitation bandwidth.[2.23,224] As a result, it is possible to acquire rotational distributions over a very wide spectral range. The disadvantage of the dispersed fluorescence method is that one cannot tell how an ionic level was created, so it is important to restrict the number of target levels undergoing ionization to allow for meaningful comparisons with theory. In this regard, the current investigation works with a colder distribution of target molecules than in the previous work.[2.11] In order to understand the photoelectron dynamics, it is useful to understand how the photoion rotation varies with photoelectron energy, and dispersed fluorescence experiments on molecular photoions provides precisely this type of information.

In this chapter, it is shown that the effects of the CO $4\sigma \rightarrow k\sigma$ shape resonance can be amplified and studied quantitatively if the target molecules are cooled more effectively ($T_0 \approx 9$ K). Novel applications of a cryogenically cooled gas jet relating to rotationally resolved spectra are discussed in this chapter. This new use of a supersonic expansion was the key element in allowing a notable change in rotational temperature versus the earlier studies. By reducing the temperature a dramatic reduction in populated rotational states was caused and a comparison of the experimental data with theory was allowed. The theoretical calculations were performed over a range of temperatures and the best fit is shown (9K). Theoretical results from the research lab of V. McKoy (California Institute of Technology) will be presented to give a comparison of the experimental results to theory.[2.25] The rotational distributions for the $v^+ = 0$ and $v^+ = 1$ vibrational levels were determined after photoionization by monochromatic synchrotron radiation. The primary motivation of this study was to determine how the relative rotational

populations are modulated by the ionization energy, in the low energy region, and if a liquid nitrogen cryogenically cooled nozzle would increase the effects of the shape resonance. My specific contributions to this project include the optimization of the liquid nitrogen cooling and experimental optimization for rotationally resolved studies.

2.1.1 Theory

This section contains the details for the calculations and theoretical background provided by V. McKoy (California Institute of Technology).[2.25]

The formulation of rotationally resolved photoelectron spectroscopy (used for comparisons with dispersed fluorescence experiments) has been described previously.[2.7,29] The necessary background is briefly reviewed. These calculations were performed over a wider spectral range than is typical to obtain the ion distributions needed for comparison with the present experiments. Since the fluorescence experiment integrates over all initial rotational levels J_0, Mckoy considers all the transitions terminating in a specific ion level J^+. In the present case, ionization originating from each of the $(2J_0 + 1)$ magnetic sublevels of the ground state of CO forms an independent channel. The total cross section σ for ionization of a J_0 level of the state leading to a J^+ level of the ion is dependent on the matrix element $r_{fi}^{l\lambda\mu}(R)$ and which can be expanded in angular momentum partial waves (Equation 2.1)

$$r_{fi}^{l\lambda\mu}(R) = \sum_{l',l_0} \langle g_{l,l'\lambda}(k,r,R) Y_{l'\lambda}(\hat{r}) \,|\, rY_{l\mu}(\hat{r'}) \,|\, \phi_{l_0} \times (r,R) Y_{l_o\lambda_0}(\hat{r'}) \rangle$$

Equation 2.1 Matrix element as a sum of *l* partial waves.

This is significant for the current study, because the R-dependence provides information on how the rotational substructure will differ between the $v^+ = 0$ and $v^+ = 1$ levels. In the calculation of the photoelectron matrix element, $r_{fi}^{\ell\lambda\mu}(R)$, one considers both *l*-conserving and *l*-changing collisions. Whereas only $l = l'$ would be allowed for the central fields of atomic systems, where the angular momentum of the photoelectron must be conserved, $l \neq l'$ terms arise in molecules due to angular momentum coupling brought about by the nonspherical molecular ion potential. These *l*-changing collisions strongly influence the ion rotational distributions in molecular photoionization. The present fluorescence measurements allow us to see how this underlying dynamical behavior evolves with energy.

There are two dipole-allowed channels for photoionization of the 4σ orbital of the ground state CO. An electron from the 4σ orbital can be ejected into $k\sigma$ or $k\pi$ continuum channels. Ionization into the $k\sigma$ and $k\pi$ continua results in an electron-ion complex of $^1\Sigma^+$ and $^1\Pi$ total final-state symmetries, respectively. The procedures for determining the continuum wavefunctions are described in detail elsewhere.[2.26] Our calculations are performed at the Hartree-Fock level, which is sufficient to identify and account for the key dynamical aspects here. The ground state wave function of CO is obtained at the self-consistent-field (SCF) level and the Gaussian basis functions employed are described elsewhere.[2.27] The partial wave angular momentum composition of the 4σ orbital of CO is 14.56 % *s*, 62.35 % *p*, 15.67 % *d*, 3.09 % *f*, 2.72 % *g* ($\ell_0 = 4$), 0.36 % *h* ($\ell_0 = 5$), and 0.57 % *i* ($\ell_0 = 6$) at R_e=2.1322 a.u. This 4σ orbital also evolves with internuclear distance. For example, it has a dominant *s*, *p*, and *d* composition at small internuclear distance

(29.76 % *s*, 43.55 % *p*, 23.60 % *d*, 1.04 % *f*, 1.62 % *g* (ℓ_0 = 4), 0.12 % *h* (ℓ_0 = 5), and 0.18 % *i* (ℓ_0 = 6) at R = 1.5 a.u.), a dominant *p* character at *R* = 2.6 a.u. (11.93 % *s*, 71.83 % *p*, 5.51 % *d*, 4.75 % *f*, 2.70 % *g* (ℓ_0 = 4), 0.62 % *h* (ℓ_0 = 5), and 0.96 % *i* (ℓ_0 = 6), and a strong *s* and *p* admixture at larger internuclear distance (19.84 % *s*, 60.37 % *p*, 5.82 % *d*, 6.45 % *f*, 1.49 % *g* (ℓ_0 = 4), 0.84 % *h* (ℓ_0 = 5) and 1.11 % *i* (ℓ_0 = 6) at *R* = 3.5 a.u.). For the final state, McKoy assumes a frozen-core Hartree-Fock model in which the ion orbitals are taken to be that of the ground state of CO and the photoelectron orbital is obtained as a solution of a one-electron Schrodinger equation. All matrix elements arising in the solution of the Lippmann-Schwinger equation were evaluated via single-center expansions at the center of mass.

2.1.2 Dispersed Fluorescence Vs. Photoelectron Spectroscopy

Rotationally resolved spectra can be collected with dispersed fluorescence and photoelectron spectroscopy. Photoelectron spectroscopy determines the fate and energy of the ejected electron and this technique has been used extensively in the collection of vibrationally resolved spectra.[2.28,229] The key drawback of photoelectron spectroscopy for rotationally resolved studies is that the excitation bandwidth is large compared to the rotational spacing. The utilization of photoelectron spectroscopy for rotationally resolved spectra has typically been limited to the near threshold region, although significant progress has been made for highly resolved studies.[2.30] Dispersed fluorescence is able to circumvent the resolution problems associated with photoelectron spectroscopy by effectively decoupling the excitation and collection bandwidth.[2.23] This is accomplished

by collecting the fluorescent photons and determining the rotational structure though an optical monochromator.

2.1.3 Experimental Method Background and Theory

Temperature control of the target gas was employed in order to achieve the smallest number of rotational states populated in the target. This was accomplished through the use of a cryogenically cooled supersonic expansion gas nozzle. A series of preliminary experiments were performed to determine the coldest portion of the supersonic expansion. In addition to the rotational cooling, a technique of optical windowing was employed to only detect the coldest part of the molecular beam. Rotational cooling is discussed in the next section and optical windowing is discussed in the experimental section. The optical windowing was made possible by the use of a charged coupled device (CCD) detector. With the use of a mirror, the photons from the width of the molecular beam are imaged vertically onto the CCD. By limiting the range of vertical pixels read out, the coldest part of the beam can be detected. This was previously explained in Dr. H.C. Chois dissertation.[2.31] In addition, extreme care was taken to ensure proper alignment of the optics used for detection, as any misalignment would have hindered the desired level of rotational resolution.

2.1.3.1 Rotational Cooling

Rotational cooling is accomplished through the use of a supersonic expansion gas jet.[2.32] The gas jet is a small hole (nozzle) used to introduce sample at selectable pressures. The technique of free jets has been widely applied to spectroscopy of neutral and ionic species.[2.33,234] The term supersonic refers to a condition when the velocity of the sample gas exceeds the local speed of sound in the experimental chamber. Under

supersonic conditions, the expanding gas encounters a shock boundary along the edges of the expansion and is compressed to the center of the expansion. The cooling effects are greatest in the center of the gas jet. As the gas continues to expand along this path the cooling effect increases until the mach disk is reached. The mach disk is the location where the local speed of sound is surpassed and the cooling effects no longer take place.

To achieve a supersonic expansion several conditions must be met, including a large pressure gradient, a small nozzle diameter and a sufficient region of space for the gas to expand. The need for a large expansion region is evident if the free mean path of a molecule is considered. In order for a mach disk to form the gas must interact with another gas molecule before the chamber wall is encountered. If the gas molecules do not interact with another molecule there is no change in the temperature. The mach disk is also the largest distance from the nozzle where spectroscopy of cooled molecules should be performed (Equation 2.2). Beyond the mach disk the only change in the properties of the gas jet is reduced density, effectively reducing count rates for an experiment. The pressure differential of the gas jet and the initial temperature have an effect on the final temperature of the gas. The pressure ratios are selected by experimental constraints such as pumping speed and nozzle diameter. The initial temperature is limited by the condensation or freezing point of the sample gas. In the current study a compromise between temperature and pressure was required to prevent the plugging of the gas jet by frozen CO. The initial temperature was the only available parameter left to reduce the temperature. To increase the cooling of the sample a LN2 cooled copper block was employed which reduced the initial temperature.

$$X_{mach} = 0.67D\left(\frac{P_O}{P_F}\right)^{1/2}$$

Equation 2.2 Distance from the nozzle aperture to the mach disk. D is the nozzle diameter. P_o and P_F are the stagnation pressure and post expansion pressure.[2.35]

2.1.3.2 Detection Method

The detection method used for the following data collection was a CCD. CCDs were briefly discussed in Chapter 1 and a more detailed explanation of the properties and specific advantages exploited for this study will be outlined here. The specific advantages discussed will include optical windowing, alignment issues, and collection of a spectrum as a simultaneous event. Optical windowing and the ability to collect a spectrum as a single event are key elements that made this study possible.

A CCD consists of a two-dimensional array of photodiodes with the ability to store a charge. When an incident photon interacts with one of the photodiodes the light is converted into a single charge.[2.36] As subsequent photons hit the detector they are converted to additional charge. At the end of the user defined collection time the charge is read out by control hardware. There are two distinct ways to read out a CCD. The first method allows for the collection of a spectrum of energy versus wavelength and the second allows for a two-dimensional image to be read out. In order to discuss the two methods of CCD readout, it is necessary to cover the features of the incident radiation. The fluorescence from the experimental chamber is dispersed by an optical monochromator in two directions. The light is dispersed along the x-axis of the detector

according to energy and the vertical axis contains the photons with respect to the location of the initial event. When the data is read out it is converted to an energy versus intensity spectrum. CCDs have the ability to read out selected pixels. This selective readout allows for the technique of optical windowing. In the two-dimensional readout mode each pixel is read out individually.

Optical windowing is a technique used to selectively collect photons from the ionization event.[2.36] This allows for the collection of photons that originate from the coldest part of the molecular beam. The interaction region is defined in distance from the gas nozzle by the width of the incident photons; however, the ionization region is limited perpendicular to the molecular beam only by the sample density. By orienting the collection monochromator entrance slit perpendicular to the incident photons the vertical dispersion on the detector corresponds to the distance from the axis of the gas expansion. In order to collect the coldest part of the beam, the top and bottom of the dispersed signal is not read out, reducing the average temperature of the collected events from the target molecules. The fringes of the gas jet contain the shock boundary molecules and molecules from the background pressure. Both of these sets of molecules are not cooled by the expansion. Figure 2.2 shows how the photons from an ionization event are channeled to the CCD detector. As the photons are collected the photons from the coldest molecules, involved in interactions, are centered about the vertical axis of the CCD. There is a second optical translation that is not shown; light is shifted in the monochromator from the top to bottom of the CCD and vice versa. This translation has no practical effect in selecting the center of the beam.

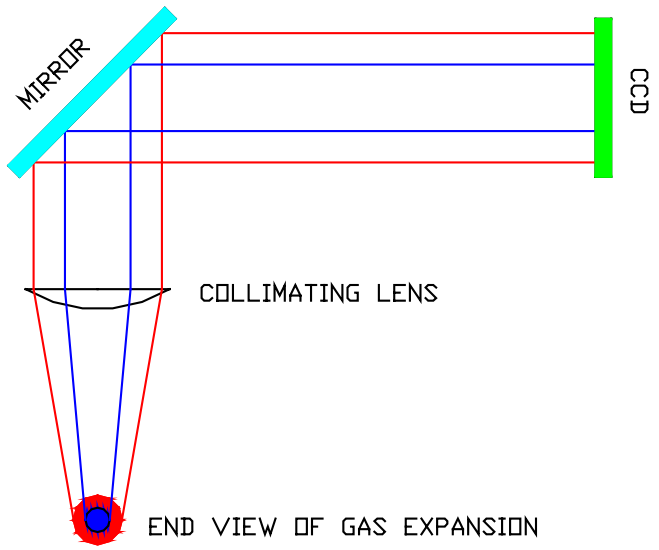

Figure 2.2 Diagram showing the relationship of the ionization event position to the final vertical position on the CCD.

Alignment is made much less tedious with the use of the two-dimensional readout property of a CCD. This is extremely important in studies that require rotationally resolved spectra. It is almost impossible to completely align all of the optical components with respect to small angular variations. By collecting the dispersed light in a two-dimensional readout any small angular rotations are evident in the orientation of the spectral features. Large deviations need to be corrected by realigning the optics and small deviations are corrected by rotating the detector.

2.2 Experimental

Data were collected using a vacuum chamber with optical components suited for dispersed fluorescence collection. A schematic of the apparatus is shown in Figure 2.3. Typical stored ring current parameters for the synchrotron during this study were 200 mA and the beam energy was 1.3 GeV. The resulting radiation was monochromatized ($\Delta h\nu \approx 0.4$ eV) by a 6 m plane grating monochromator.[2.37] The resulting monochromatic light is used to ionize the target gas molecules. Data collection times were typically 30

minutes per incident energy. The incident photons were channeled into the experimental chamber using a capillary light guide which was differentially pumped in two stages. The first stage consists of a 60 l/s turbo molecular pump at the split in the capillary light guide. Finally a 200 l/s turbo pump was used at the entrance to the beam line. The use of differential pumping is critical to maintain an ultrahigh vacuum in the beamline and storage ring (10^{-9} Torr), while maintaining the chamber at *ca.* 10^{-4} Torr. The gas jet for the supersonic expansion was 100 μm with a stagnation pressure of 4 psig. To enhance the rotational cooling, liquid nitrogen was used to refrigerate a copper jacket surrounding the gas jet. This enhancement significantly reduced the number of populated rotational target states. Obtaining rotational resolution is demanding for the $CO^+(B^2X^+ \rightarrow X^2X^+)$ transition, as rotational transitions are closely spaced (<4 cm^{-1}).[2.9] To achieve the required resolving power, a 1-meter optical monochromator was used (Instruments SA model THR-1000) with a 3600 g/mm grating. The slit width was set at 50 μm, resulting in a fluorescence bandwidth of 0.13 Å. For fluorescence detection a CCD-based OMA detector was used (Princeton Instruments LN/CCD-134/400-ES1).

The raw data consisted of a series of florescence spectra (Figure 2.4). The first step in reducing the data to useable form was the removal of cosmic ray artifacts. Cosmic rays refer to any spectral feature of an unknown origin typically with high intensity and very narrow spatial width (1 pixel). In most cases, as the name implies, cosmic rays come from extraterrestrial events. When working with synchrotron radiation there is also the possibility of stray radiation producing "cosmic radiation artifacts". Due to the 30 minute collection time for the raw data the problems associated with cosmic radiation were amplified. The removal of cosmic radiation was accomplished with

software developed by Dr. Scott J. Miller, through the averaging of adjacent spectral intensities.[2.36] To determine the rotational populations of the data, background subtraction and relative populations, calculations were performed using a Visual Basic program. Data were taken over the range from 20-140 eV. Data sets were collected with better counting statistics over a limited spectral range (20-40 eV) to allow for a detailed comparison for the rotational substructure between the $v^+ = 0$ and $v^+ = 1$ vibrational levels.

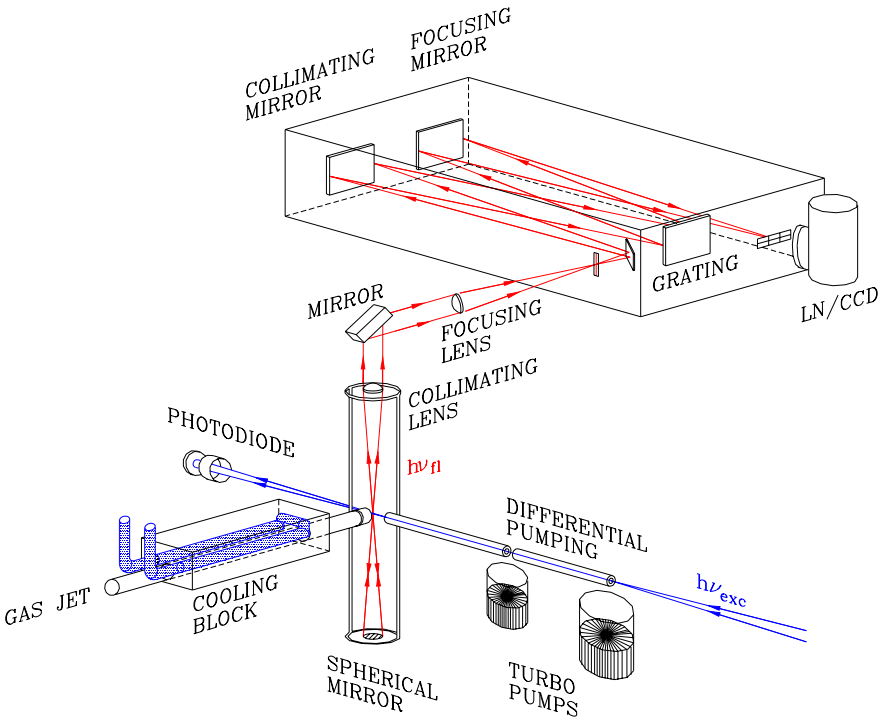

Figure 2.3 Schematic of experimental chamber. Details included are the turbo pumps, sample cooling and optical systems for data collection.[2.36]

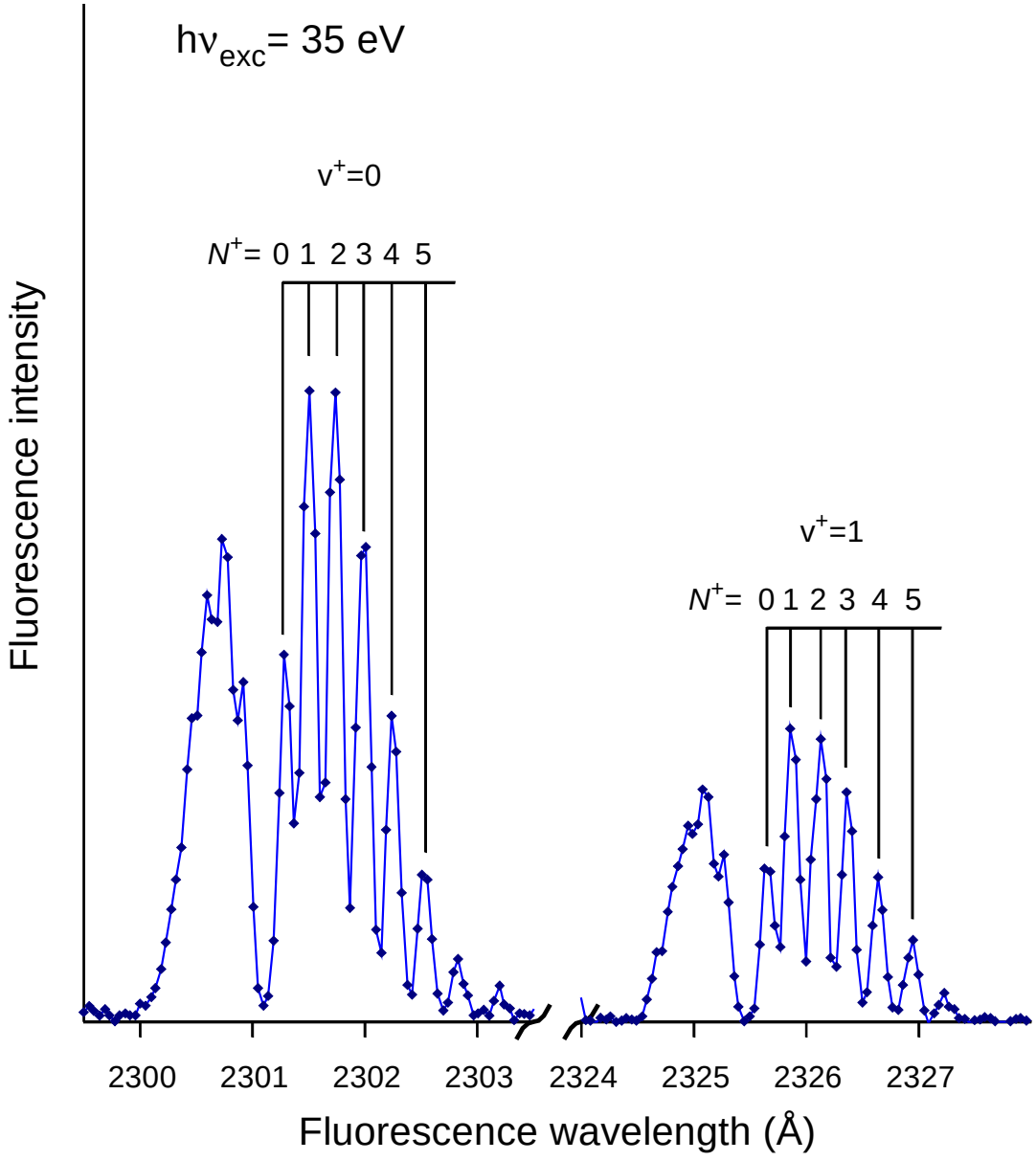

Figure 2.4 Typical CO fluorescence spectra showing the $v^+ = 1$ and $v^+ = 0$ transitions. The axis is split to conserve space however both spectral features were collected together.

2.3 Discussion

A typical $CO^+(B^2\Sigma^+ \rightarrow X^2\Sigma^+)$ fluorescence spectrum is shown in Figure 2.4. The quality of the data is higher than for those reported previously[2.10], in terms of both resolution and overall counting statistics. This is largely a result of the increased quantum efficiency of the CCD detector employed in the current study. The cooling was able to amplify the effects of the shape resonance independent of the counting statistics. The horizontal axis is split to display results for both $v^+ = 0$ and $v^+ = 1$. Both bands are obtained in a single exposure at each incident energy, so variations in experimental conditions have minimal effects when comparing results for these two vibrational levels. The intensities of the P-branch transitions were determined more precisely because of the greater separation between the peaks, so these intensities were used in the data analysis. To determine the relative populations, the intensity of each rotational transition was integrated, corrected for the rotational line strength and the normalized totals were reported.[2.9,211] A plot of the relative populations as a function of photon energy is shown in Figure 2.5. In addition to the current results, data from the previous study is shown on the right-hand side for comparison. The differences between the data sets demonstrate that the sample is rotationally colder for the present study. To see this, note that the relative populations of the lower rotational levels are enhanced while the higher rotational levels are reduced in the current study, which shows that the ionic rotational distribution is colder (Figure 2.5). The temperature was determined by comparing the rotational distributions to calculations of the rotational populations at a range of temperatures. The final estimated temperature was 9 K, a 50 percent reduction from the previous work at 18 K.[2.11] The ionic rotational distribution is a reflection of the target distribution with the

photoionization rotational transitions folded in; therefore Figure 2.5 also demonstrates that the neutral target distribution is colder as well.

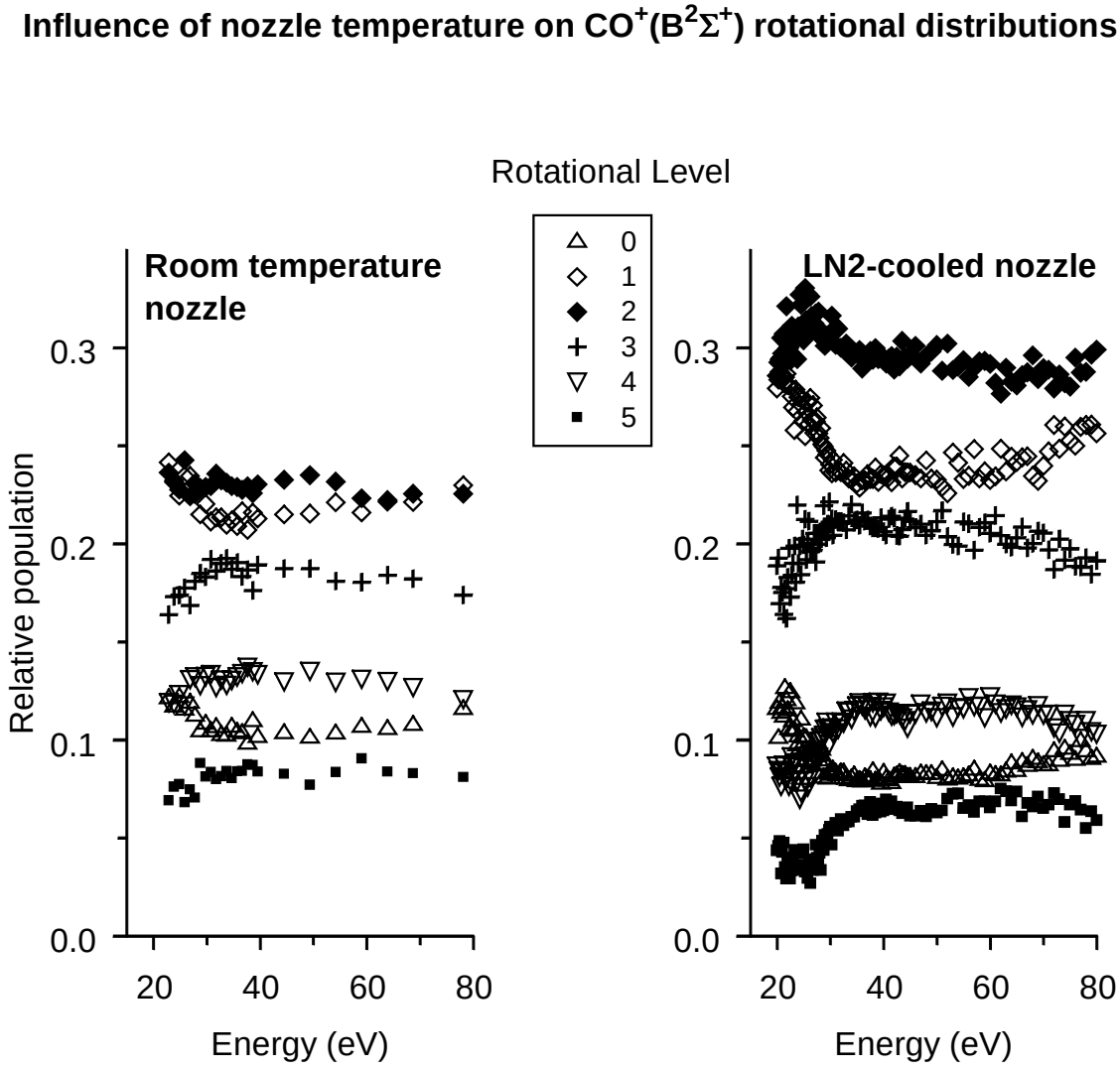

Figure 2.5 Comparison of rotational population. Left: Rotational populations from previous study.[2.11] Right: Results obtained using cryogenically cooled supersonic nozzle. This figure illustrates that the improved cooling amplifies the magnitude of the variations in rotational populations.

More importantly, Figure 2.5 shows that the energy dependence for each rotational level population has more pronounced excursions in the present investigation. This indicates that fewer target rotational levels are populated and averaged over in the rotational distributions that are observed. In the previous study the shape resonant effects were masked by contributions from higher excited states. The most pronounced features in these curves are observed for photon energies below 50 eV. These excursions in the rotational distributions are the result of the shape resonance in the $4\sigma \rightarrow k\sigma$ $l = 3$ channel.[2.38,239]

In Figure 2.6 the energy dependence of each rotational level population is plotted in a separate frame and the trends are evident. The lower rotational levels ($N^+ = 0$ and $N^+ = 1$) exhibit a sharp decrease near threshold, followed by a broad minimum between 30-60 eV photon energy. The $N^+ = 2$ and $N^+ = 3$ levels are comparatively flat, except for a sharp maximum near threshold (i.e., at $h\nu_{exc} \approx 30$ eV). This is particularly apparent in the $N^+ = 2$ curve. Finally, the higher rotational levels ($N^+ = 4$ and $N^+ = 5$) exhibit a minimum near threshold ($h\nu_{exc} \approx 25$ eV), followed by a maximum at 45 eV and a broad minimum at $h\nu_{exc} \approx 100$ eV. Also shown in Figure 2.6 are the results from theory for the $v^+ = 0$ rotational populations, which permit a comparison with experiment. There is excellent agreement between calculated and experimentally determined rotational populations. As discussed above, the relative rotational populations depend on the initial temperature of the target molecule undergoing photoionization. McKoy performed calculations for several target rotational temperatures and the agreement between experiment and theory was best when a target temperature of 9 K was used for the calculations.[2.25]

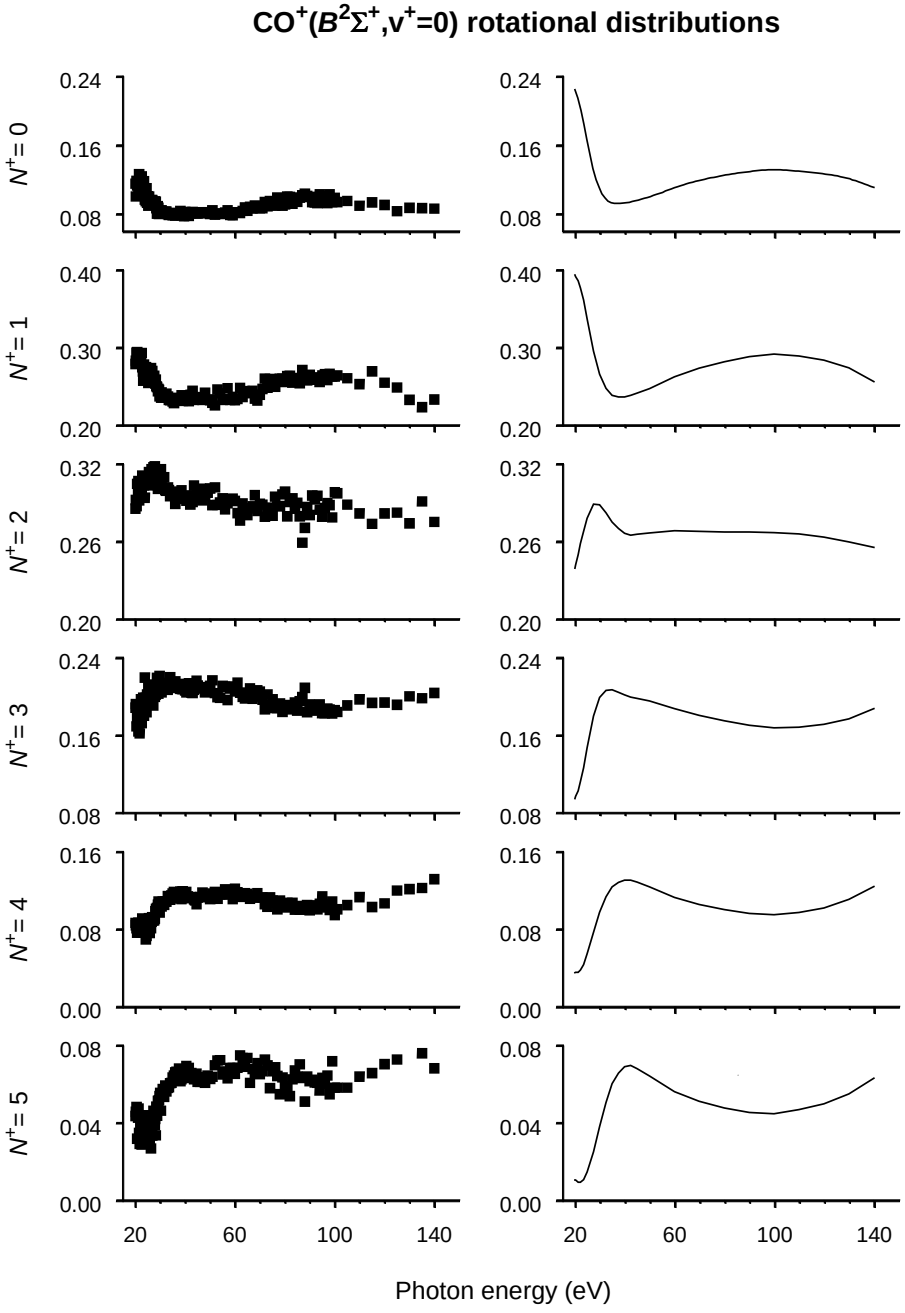

Figure 2.6 Rotational populations as a function of energy (experimental and theoretical). Note the offset baselines.

The primary motivation of this study was to see how the relative rotational populations are modulated in the low energy region and if a cryogenically cooled nozzle would increase the effects. The results clearly demonstrate the resonant enhancement in the $k\sigma$ channel $l = 3$ component. The calculated dipole amplitudes for the $4\sigma \rightarrow k\sigma$ channel are shown in Figure 2.7 and it is clear that the strong resonance in the $l = 3$ component coincides with the more pronounced excursions in the rotational populations in Figure 2.6.

It is also instructive to examine the higher energy behavior. In the earlier study, the relative populations were comparatively flat over a broad range. The present results demonstrate that the rotational populations for the lower (upper) rotational levels are clearly decreasing (increasing) at the highest photon energies. In fact, this is expected, as it is intuitively obvious that increasing photoelectron energies imply larger angular momentum continuum components. Large amplitudes for high-l partial waves make possible larger ΔN transitions. Thus, it is probably true that as the photon energy is increased over a broad enough range, all molecules will exhibit the same qualitative behavior – lower rotational levels decreasing and upper rotational levels increasing with increasing energy – as is observed in Figure 2.6. The previous N_2 $2\sigma_u^{-1}$ results exhibited similar behavior. However, while the global trends are similar to those of the N_2 results, it is important to note that the approach to this limiting behavior is much different for these valence isoelectronic systems. Thus, the limiting behavior might be similar, but if the approach to that limit is sufficiently gradual, then even the broad range behavior (i.e., dynamics over a range of hundreds of eV) for these two systems can appear distinctly different.

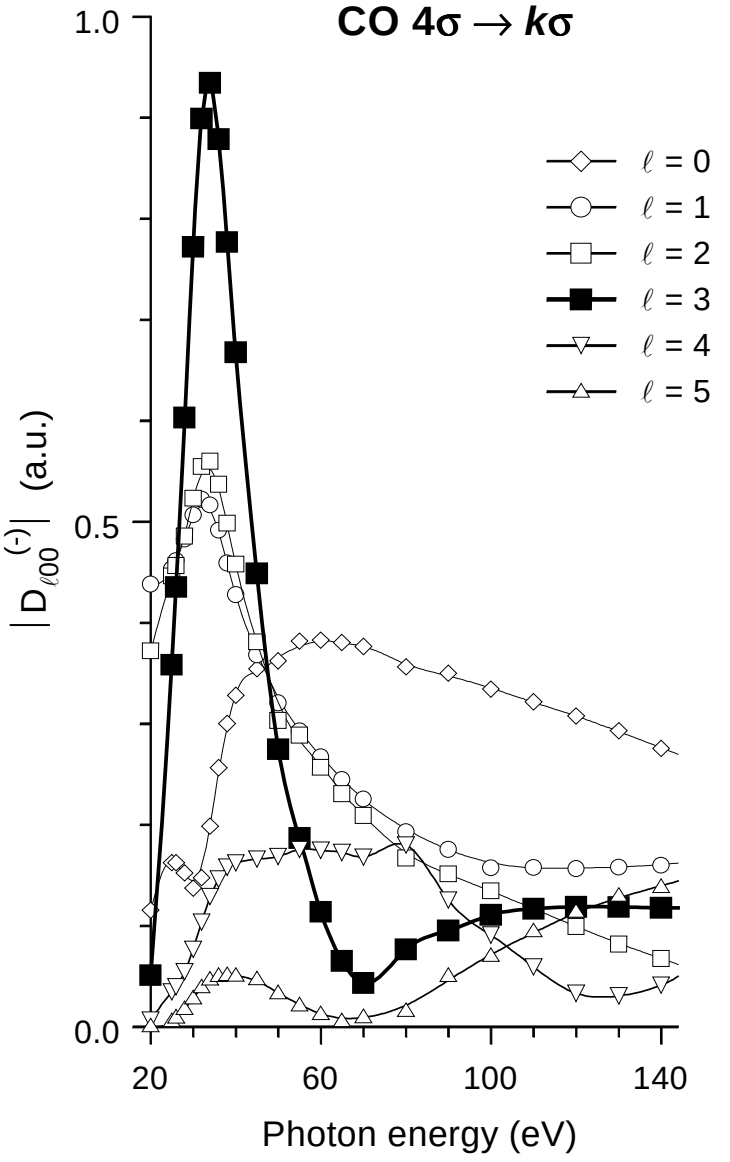

Figure 2.7 Calculated partial wave amplitudes for the 4σ → *k*σ continuum channel.

The fluorescence spectrum (Figure 2.4) displays transitions originating from the $v^+ = 1$ level as well as from the $v^+ = 0$ level. Thus, it is possible to compare the rotational substructure between the two bands as a function of incident photon energy, analogous to a previous study on vibrational-rotational-electronic (V-R-E) correlations in $2\sigma_u^{-1}$ photoionization of N_2.[2.40] It is well known that the effects of shape resonances are influenced by the bond length for diatomic systems[2.41,242], so it is reasonable to inquire if the rotational substructure would be affected, particularly in the lower energy region where the shape resonant effects are dominant. This comparison has been generated, and the results are shown in Figure 2.8. The effects are relatively small, so the data are presented in a way to highlight the differences. Specifically, each frame in Figure 2.8 corresponds to a specific rotational level of the ion, and the vertical axis represents the ratio of the relative population for that rotational level for the $v^+ = 1$ level relative to that of the $v^+ = 0$ level. The qualitative trends are reproduced well by theory, although the experimental results display significantly more scatter. Specifically, for a photon energy of $h\nu_{exc} \approx 27$ eV, these ratios display peaks for the lower rotational levels and dips for the upper rotational levels. This is because the shape resonance shifts to *lower* energy as the bond length is increased. On average, the $v^+ = 1$ level samples greater internuclear separations than the $v^+ = 0$ level and as a result, extrema in the rotationally-resolved vibrational branching ratios are shifted to lower energy from the shape resonance position seen for the $l = 3$ resonance displayed in Figure 2.7. In general, the agreement between experiment and theory is very good for all of the results shown in Figures 2.5 and 2.7, lending credibility to both the underlying theory and the experiment.

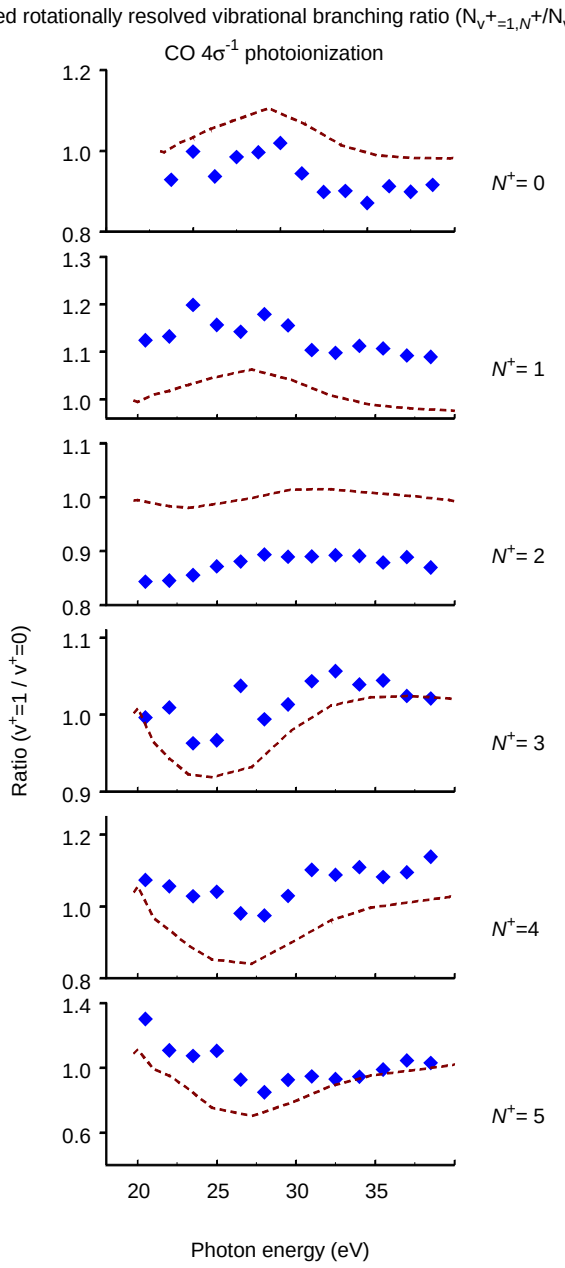

Figure 2.8 Comparison of rotational structure for both vibrational levels. Specifically, each frame corresponds to a specific rotational level of the ion, and the vertical axis represents the ratio of the relative population for that rotational level for the $v^+ = 1$ level relative to that of the $v^+ = 0$ level.

2.4 Conclusions

Rotationally resolved results are presented for $4\sigma^{-1}$ photoionization of CO. Specifically, experiment and theory have been used to determine the relative rates of production of specific rotational levels of the $CO^{+}(B^{2}\Sigma^{+})$ state. Experiments were performed by measuring the dispersed fluorescence from electronically excited photoions, and calculations were performed using Schwinger variational methods. The dependence of the rotational distributions as a function of incident photon energy have been determined over a very wide range, and the effects of a $4\sigma \rightarrow k\sigma$ shape resonance are clearly discernible in the data and in the theory. In fact, the agreement between experiment and theory is excellent. By comparing the present experimental results to previous data, it is demonstrated that improved rotational cooling of the neutral target molecules has significantly amplified the effects which are now visible.

2.5 References

2.1 Wiedmann, R. T.; White, M. G.; Wang, K.; McKoy, V. Single-Photon Threshold Photoionization of No. *Journal of Chemical Physics* **1993**, *98*, 7673-7679.

2.2 Mullerdethlefs, K.; Schlag, E. W. High-Resolution Zero Kinetic-Energy (Zeke) Photoelectron-Spectroscopy of Molecular-Systems. *Annual Review of Physical Chemistry* **1991**, *42*, 109-136.

2.3 Braunstein, M.; McKoy, V.; Dixit, S. N.; Tonkyn, R. G.; White, M. G. Shape Resonance Effects in the Rotationally Resolved Photoelectron-Spectra of O-2. *Journal of Chemical Physics* **1990**, *93*, 5345-5346.

2.4 Pratt, S. T.; Dehmer, P. M.; Dehmer, J. L. Photoionization of Excited Molecular-States - H2 C-1-Pi-U. *Chemical Physics Letters* **1984**, *105*, 28-33.

2.5 Wilson, W.; Viswanathan, K.; Sekret, A.; Reilly, J. Rotationally Resolved Laser Photoelectron-Spectrum of Gas-Phase NO. *Journal of Chemical Physics* **1984**, *88*, 672-673.

2.6 McKoy, V.; Carlson, T. A.; Lucchese, R. R. Photoelectron Dyncamics of Molecules. *Journal of Physical Chemistry* **1984**, *88*, 3188-3196.

2.7 Wang, K. H.; McKoy, V. High-Resolution Photoelectron Spectroscopy of Molecules. *Annual Review of Physical Chemistry* **1995**, *45*, 275-304.

2.8 Tonkyn, R. G.; Winniczek, J. W.; White, M. G. Rotationally Resolved Photoionization of O-2+ near Threshold. *Chemical Physics Letters* **1989**, *164*, 137-142.

2.9 Poliakoff, E. D.; Choi, H. C.; Rao, R. M.; Mihill, A. G.; Kakar, S. et al. Photoion Rotational Distributions from near-Threshold to Deep in the Continuum. *Journal of Chemical Physics* **1995**, *103*, 1773-1787.

2.10 Rao, R. M.; Poliakoff, E. D.; Wang, K. H.; McKoy, V. Molecular photoionization as a probe of vibrational-rotational- electronic correlations. *Journal of Chemical Physics* **1996**, *104*, 9654-9657.

2.11 Choi, H. C.; Rao, R. M.; Mihill, A. G.; Kakar, S.; Poliakoff, E. D. et al. Energy-Dependence of Photoion Rotational Distributions of N2 and Co. *Physical Review Letters* **1994**, *72*, 44-47.

2.12 Piancastelli, M. N.; Keller, P. R.; Taylor, J. W.; Grimm, F. A.; Carlson, T. A. et al. Trend of Shape Resonance-Induced Features in the Angular- Distribution Parameter as a Function of Photon Energy for Carbon, Silicon and Germanium Tetrachlorides. *Journal of Electron Spectroscopy and Related Phenomena* **1984**, *34*, 205-214.

2.13 Dehmer, J. L.; Dill, D. Molecular Effects on Inner-Shell Photoabsorption - K-Shell Spectrum of N-2. *Journal of Chemical Physics* **1976**, *65*, 5327-5334.

2.14 Dehmer, J. L.; Dill, D. Shape Resonances in K-Shell Photoionization of Diatomic- Molecules. *Physical Review Letters* **1975**, *35*, 213-215.

2.15 Dehmer, J. L. Evidence of Effective Potential Barriers in X-Ray Absorption-Spectra of Molecules. *Journal of Chemical Physics* **1972**, *56*, 4496-&.

2.16 Carlson, T. A.; Krause, M. O.; Svensson, W. A.; Gerard, P.; Grimm, F. A. et al. Photoelectron Dynamics of the Cooper Minimum in Free Molecules. *Zeitschrift Fur Physik D-Atoms Molecules and Clusters* **1986**, *2*, 309-318.

2.17 Manson, S. T. Systematics of Zeros in Dipole Matrix-Elements for Photoionizing Transitions - Nonrelativistic Calculations. *Physical Review A* **1985**, *31*, 3698-3703.

2.18 Carlson, T. A.; Fahlman, A.; Krause, M. O.; Keller, P. R.; Taylor, J. W. et al. Angle Resolved Photoelectron-Spectroscopy of the Valence Shells in Hi and Ch3i as a Function of Photon Energy from 13 to 90 Ev. *Journal of Chemical Physics* **1984**, *80*, 3521-3527.

2.19 Kelly, L. A.; Duffy, L. M.; Space, B.; Poliakoff, E. D.; Roy, P. et al. Vibrationally Resolved Shape Resonant Photoionization of N2o. *Journal of Chemical Physics* **1989**, *90*, 1544-1550.

2.20 Kakar, S.; Choi, H. C.; Poliakoff, E. D. Rotationally Resolved Fluorescence as a Probe of Molecular Photoionization Dynamics. *Journal of Chemical Physics* **1992**, *97*, 6998-7001.

2.21 Piancastelli, M. N. The neverending story of shape resonances. *Journal of Electron Spectroscopy and Related Phenomena* **1999**, *100*, 167-190.

2.22 Loomba, D.; Wallace, S.; Dill, D.; Dehmer, J. L. Pictures of Un-Bound Molecular Electrons, Including Shape-Resonant States - Eigenchannel Contour Maps. *Journal of Chemical Physics* **1981**, *75*, 4546-4552.

2.23 Poliakoff, E. D.; Ho, M. H.; Leroi, G. E.; White, M. G. Non-Franck-Condon 2-Sigma-U-1 Vibrational Distributions in N-2+ - an Interchannel-Coupled Shape Resonance Observed by Dispersed Fluorescence. *Journal of Chemical Physics* **1986**, *84*, 4779-4785.

2.24 Poliakoff, E. D.; Rao, R. M. Rotational and vibrational effects in photoionization: Bridging the gap from microvolts to kilovolts. *Journal of Electron Spectroscopy and Related Phenomena* **1996**, *79*, 361-366.

2.25 Farquar, G. R.; Miller, J. S.; Poliakoff, E. D.; Wang, K. S.; McKoy, V. Rotationally resolved photoionization: Influence of the 4 sigma -> k sigma shape resonance on CO+(B (2)Sigma(+)) rotational distributions. *Journal of Chemical Physics* **2001**, *115*, 9764-9770.

2.26 Lucchese, R. R.; Takatsuka, K.; McKoy, V. Applications of the Schwinger Variational Principle To Electron Molecule Collisions and Molecular Photoionization. *Physics Reports* **1985**, 147-221.

2.27 Kong, W.; Rodgers, D.; Hepburn, J.; Wang, K.; McKoy, V. Pulsed-Field Ionization Threshold Photoelectron-Spectroscopy With Coherent Extreme-Ultraviolet Radiation- A Comparison Of CO and N(2). *Journal of Chemical Physics* **19993**, *99*, 3159-3165.

2.28 Braunstein, M.; McKoy, V. Vibrational Branching Ratios and Shape Resonant Photoionization Dynamics in N2o. *Journal of Chemical Physics* **1989**, *90*, 1535-1543.

2.29 Yates, B. W.; Tan, K. H.; Bancroft, G. M.; Coatsworth, L. L.; Tse, J. S. Photoelectron Study of the Valence Levels of Cf4 and Sif4 from 20 to 100 Ev. *Journal of Chemical Physics* **1985**, *83*, 4906-4916.

2.30 Ohrwall, G.; Baltzer, P.; Bozek, J. Synchrotron radiation excited photoelectron spectrum of H-2(+) with rotational resolution. *Journal of Physics B-Atomic Molecular and Optical Physics* **1999**, *32*, l51-l65.

2.31 Choi, H. C. Energy dependence of photoion rotational distributions. In *Chemisrty*; Louisiana State University: Baton Rouge, 1994; pp 94.

2.32 Hayes, J. M.; Small, G. J. Supersonic Jets, Rotational Cooling, and Analytical-Chemistry. *Analytical Chemistry* **1983**, *55*, A565-&.

2.33 Engelking, P. C. Spectroscopy of Jet-Cooled Ions and Radicals. *Chemical Reviews* **1991**, *91*, 399-414.

2.34 Tuckett, R. P. Fluorescence-Spectra of Fluorobenzene Cations Excited in a Supersonic Molecular-Beam. *Chemical Physics* **1981**, *58*, 151-162.

2.35 Scoles, G. *Atomic and Molecular Beam Methods*; Oxford University Press, 1992; 552.

2.36 Miller, J. S. State-resolved molecular photoionization dynamics of polyatomic systems: effects of non-lineat changes in molecular geometry. In *Department of Chemistry*; Louisaiana State University: Baton Rouge, 2000; pp 257.

2.37 Morikawa, E.; Scott, J. D.; Poliakoff, E. D.; Stockbauer, R. L.; Saile, V. Design of Soft-X-Ray Plane-Grating Monochromator for Camd. *Review of Scientific Instruments* **1992**, *63*, 1300-1304.

2.38 Das, R.; Wu, C. Y.; Mihill, A. G.; Poliakoff, E. D.; Wang, K. S. et al. Photoion Alignment - Chemical Signatures 200 Ev above-Threshold. *Journal of Physical Chemistry* **1995**, *99*, 1741-1747.

2.39 Das, R.; Wu, C. Y.; Mihill, A. G.; Poliakoff, E. D.; Wang, K. S. et al. Alignment of Photoions Far from Threshold. *Journal of Chemical Physics* **1994**, *101*, 5402-5405.

2.40 Rao, R. Vibrational-rotational-electronic correlations in molecular photoionization. In *Department of Chemistry*; Louisiana State University: Baton Rouge, 1996; pp 77.

2.41 West, J.; Parr, A.; Cole, B.; Ederer, D. Shape-Resonance-Induced Non-Franck-Condon Vibrational Intensities in 3-Sigma-G Photoionization of N-2. *Journal of Physicas B-Atomic Molecular and Optical Physics* **1980**, *13*, L105-L108.

2.42 Dehmer, J. L.; Dill, D.; Wallace, S. Shape-Resoncance-Enhanced Nuclear-Motion Effects in Molecular Photo-ionization. *Physical Review Letters* **1979**, *43*, 1005-1008.

Chapter 3: X-ray Studies of Cu(II) Reduction by 2-Chlorophenol

3.1 Introduction

The work presented in this chapter demonstrates how X-ray spectroscopic data can be used to determine the oxidation states and composition of mixed-metal materials of significant environmental consequence employing a combination of *in-situ* data collection and novel data reduction techniques.[3.1] In this case we considered a mixture of copper (II) oxide and silica that was prepared to serve as a model for fly-ash that results from industrial-scale combustion, and this material was then exposed to 2-chlorophenol, which models incompletely-combusted organic materials in the incinerator. This mixture was heated to temperatures on the order of 300 °C, quenched and subjected to X-ray absorption near edge spectroscopy (XANES).

This experiment had two closely-related goals. The first was developing an *in-situ* probe to determine the fate of the copper after dioxin pollutant precursors react on the copper/silica fly-ash model surface. The second goal was to demonstrate the utility of XANES spectroscopy for mechanistic and kinetic studies of heterogeneous reactions. Both goals are based upon the expectation that X-ray spectroscopic data can provide elementally specific data, that is, that one can study a specific element of interest in a complex mixture. This degree of detail is typical of the standard catalysis literature, but ours is the first report of *in-situ* elementally-resolved studies of air pollution formation.[3.2] Our results are consistent with the contention that copper is reduced by chlorinated phenols, and reactive surface-bound species are formed that can form polychlorinated dibenzo-*p*-dioxins and polychlorinated dibenzofurans (PCDD/F or “dioxins”). The fabrication of several experimental items was required to complete this project. These and modifications made to the existing experimental cell to enable X-ray studies, trouble-shooting of

the original cell's heating system, all data analysis software development, the data analysis and the methodology development was a direct product of my work.

3.1.1 Environmental Background

There has been a growing consensus within the combustion research community that surface-mediated reactions are responsible for a significant fraction of toxic air pollutants emitted from combustion and thermal processes.[3.3] Research in this area has been driven by the discovery that emissions of polychlorinated dibenzo-*p*-dioxins and polychlorinated dibenzofurans are nearly ubiquitous and that their formation is largely due to surface-mediated reactions involving transition metals, hydrocarbons and a chlorine source.[3.4-6] Incinerators have all of the above components necessary for dioxin formation.

PCDD/F formation pathways have been proposed that involve: i) gas-phase formation from precursors such as chlorinated phenols; ii) so-called *de novo* formation from reaction of chlorine and oxygen with carbon in soot and char; and iii) transition-metal mediated reactions of precursors, such as chlorinated phenols/benzenes on the surfaces of combustion-generated particulate matter.[3.7,3.8] It is generally felt that gas-phase formation contributes no more than 30% of the total PCDD/F emissions[3.9,3.10] and recent results have suggested a 90 percent reduction of *de novo* reaction products when using reaction inhibitors.[3.11] Under the original *de novo* theory, it was suggested that PCDD/F-like species were contained in fly-ash/soot/char and were merely liberated after heating and further reaction under appropriate conditions, while the precursor theory focused on reaction of specific precursors such as chlorinated phenols and benzenes with transition metals. It is now recognized that the *de novo* and surface precursor pathways probably involve many of the same reaction intermediates, specifically the reactions of chlorinated phenols on transition metal surfaces.

Various studies presented in the literature presume that the catalytic transition metals are reduced or oxidized as chlorophenols are converted to PCDD/F.[3.12] However, the change in oxidation state has not been studied directly nor confirmed by direct experimental observation due to the unsuitability of existing techniques and methods for *in situ* metal oxidation/reduction reaction study.

Reasonable models for the chemisorption of 2-chlorophenol on Cu(II)O/silica are depicted in Figure 3.1. It is known from FTIR studies of phenol and 2-chlorophenol on Cu(II)O/silica that phenols chemisorb at surface hydroxide sites through elimination of water to form surface bound phenoxylates.[3.13] Packed bed flow reactor studies also indicate that PCDFs are formed by a Langmuir-Hinshelwood (LH) mechanism involving two surface-bound species while PCDDs are formed by an Eley-Rideal (ER) mechanism in which only one species is surface bound.[3.13] The LH pathway implies that reactions of two phenolates occur at geminal or vicinal copper sites.

EPR studies indicate the existence of a surface bound phenoxyl radical, and the existence of this radical implies electron transfer that results in the reduction of copper. If two molecules of 2-chlorophenol are chemisorbed to the same geminal copper site and two phenoxyl radicals are formed, then Cu(II)O is reduced to Cu(0) via pathway **a** in Figure 3.1 but, if only one 2-chlorophenol is chemisorbed to each copper, then reduction to Cu(I) is implied via pathway **b** in Figure 3.1. An Eley-Rideal mechanism that results in the reduction to Cu(0) requires desorption of the 2-chlorophenoxyl radical and subsequent adsorption of a second 2-chlorophenol to continue the reduction in a second cycle, or the formation of a quinone-type intermediate as shown in pathway **c** of Figure 3.1. The ultimate yield of PCDD/F is dependent upon the number of copper sites that are available for reaction as well as the number of geminal and vicinal

adsorptions. While most of the 2-chlorophenol is oxidized, oxidation nevertheless requires chemisorption and formation of reaction intermediates such as those depicted in Figure 3.1. The following studies distinguish among the possible mechanisms of 2-chlorophenol precursor reactions through the use of *in-situ* XANES.

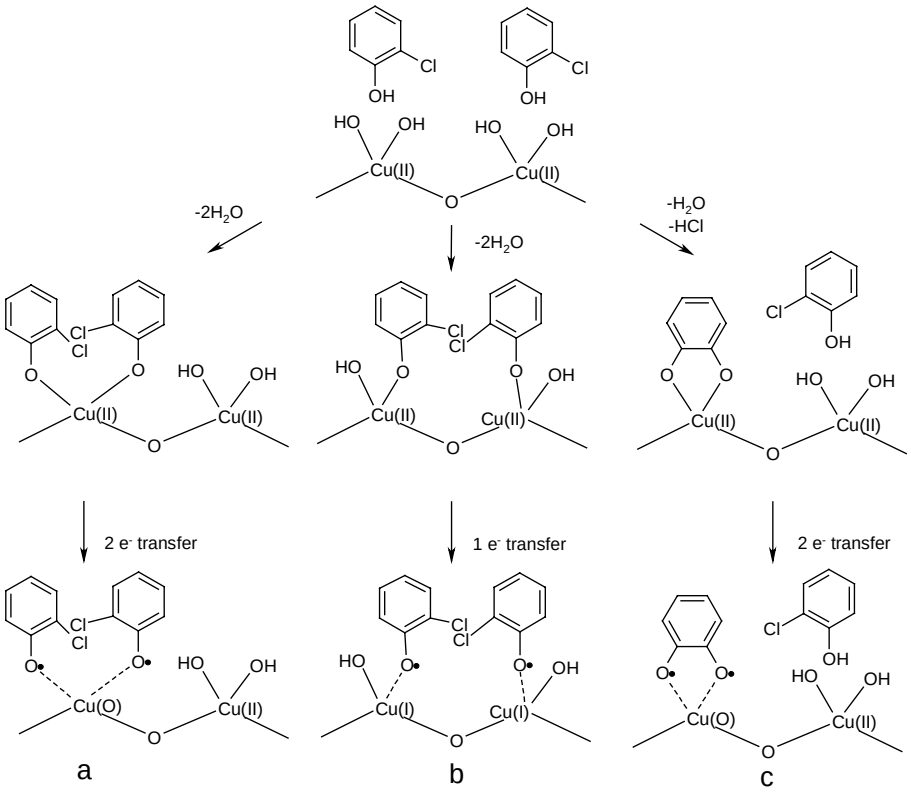

Figure 3.1 Possible mechanisms for the adsorption of 2-chlorophenol and reduction of Cu(II)O in a silica matrix. Pathway **a** invokes geminal chemisorption of two 2-chlorophenols and 2e- transfer to form Cu(0). In pathway **b**, two 2-chlorophenols are chemisorbed at vicinal sites and result in formation of Cu(I) by 1e- transfer reaction at each site. In pathway **c**, a single 2-chlorophenol forms a bidentate ligand with copper by eliminating H_2O and HCl. 2e- transfer results in the formation of Cu(0)

3.1.2 Experimental Methods

Two critical components are required for *in-situ* oxidation speciation. The first is a suitable experimental technique; the second is proper data analysis. A discussion of the spectroscopic advantages of XANES is first; the requisite data handling and analysis techniques that yield reliable and reproducible results follows.

3.1.2.1 XANES

X-ray Absorption Near Edge Spectroscopy (XANES) is a powerful probe of the oxidation state of the target molecule; the available unfilled valence orbitals and the identity of chemical bonds can be discerned.[3.14,3.15] The work about to be described is an example of XANES' power, particularly the ability to determine the oxidation state of an element in a complex mixture. XANES' ability to determine an unfilled orbital is also evident in the spectra, as is apparent in a forbidden 3s -to- 3d Cu(I) spectroscopic transition that is seen below the white line at 8982 eV. The oxidation state of a target species is evident in any shift of the white line, with more oxidized species having higher white line energies. As stated in Chapter 1, XANES spans the energy range from approximately 50 eV below the edge to several hundred volts beyond. This narrow range allows for a large number of data sets to be collected in a relatively short time, typically 15 minutes for the entire spectrum range. Recent years have seen significant advances in rapid spectrum scanning methods reducing the difficulty in collecting large data sets over a greater energy range.

XANES "fingerprinting" methods may at first seem to be quite straightforward, but several experimental hurdles are involved in determining a target atom's oxidation state.[3.16,3.17] Experimental aspects critical to successful data reduction include the ability to accurately calibrate data sets with respect to energy, and the proper selection of standards. Spectra

calibration is of utmost importance in the final data reduction, because the three oxidation states of copper have very similar spectral features that would be easy to confuse in pure samples, let alone in samples of unknown, mixed-oxidation states. This calibration is best accomplished with the simultaneous collection of sample and reference data; for our copper oxide experiments, pure copper foil is used as the Cu(0) reference. The final product mixture has a possibility of three oxidation states: Cu(0), Cu(I) , and Cu(II), and of these three possibilities, only Cu(I) will have an unknown chemical composition. (Any Cu(II) species is presumed to be the starting material and Cu(0) is of course metallic copper.) There are a limited number of possibilities for the Cu(I) species, restricted by the species present in the starting materials (2-chlorophenol and Cu(II)O). The most likely Cu(I) species are the oxide and chloride. Data for the two most likely Cu(I) species were collected and run thorough the data analysis routine (described in the next section) and the species with the lowest residuals (Cu(I)O) was used for the final analysis. The analysis when using the copper chloride yielded data fits of poor quality.

3.1.2.2 Data Analysis

Data analysis consisted of four operations conducted with commercially available software in conjunction with custom Visual Basic programs. All data sets underwent identical data treatment. The initial two steps, energy calibration and background correction, were conducted with WinXas.[3.18] The final steps, interpolation and percent component extraction, were conducted with in-house software. A final check of the data quality was conducted with Excel[3.19], in order to visually check the validity of the calculated data fits.

Each data set had a corresponding reference data spectrum of metallic copper (binding energy of 8979 eV[3.20]) that was collected simultaneously. Acquiring simultaneous reference

spectra allowed small deviations in monochromator calibration to be corrected for after the data was collected. The first derivative of the reference spectra was taken and used for calibration. This was accomplished by taking the maximum of the first derivative of the metallic copper spectrum and comparing it to the known value. The known value of 8979 eV is the energy of the maximum slope of the white line. Other techniques to determine the white line energy could be used such as the second derivative. The corresponding sample spectra were then corrected by the difference in the reference and known values. The various oxidation states of copper are separated by small binding energy shifts, making this energy calibration critical to the successful determination of the component concentrations.

The second step in data reduction is the normalization of the spectral intensity. It has emerged, through trial and error, that consistency in normalization is more critical than accuracy. A truly accurate normalization would require the pre-edge region to be flat and with a value of the slope of zero and the post-edge region oscillations to have 50 percent above and below the normalized value of one. This ideal case for normalization was a large consideration in normalization, however a greater emphasis was placed on the consistency of the technique itself yielding the highest quality data in the final analysis of copper species concentrations.

The energy-corrected normalized spectra were interpolated to a standard interval on the energy axis. In practice, the beamline monochromator selected energies were not regular. That is, in practice, an energy was selected using the beamline control software, but the monochromator did not move exactly to that energy; small deviations occured in the final crystal positions and the user-requested value which was stored to the data file. The same Visual Basic software package also limited the scope of the data sets to a selected energy range. The form of

χ^2 used is shown in Equation 3.1. The reduced χ^2 analysis was conducted by calculating a series of linear combinations of the reference spectra. As an example spectrum, consider a mixture of 1/3 of each component; in this case 0.33 times the spectra of each component would be summed to construct a new spectrum. The new summed spectrum would be compared with the experimental spectrum and the χ^2 analysis would be performed for each data point for the entire spectrum. The lowest value of the reduced χ^2 corresponded to the best fit. As a final verification of the quality of the data fit, an Excel spread sheet was used to visually graph the calculated and experimental data for each time dependent spectrum.

$$\chi^2 = \frac{(O-E)^2}{E}$$

Equation 3.1 Equation for χ^2 analysis. O=observed from calculations, E=expected from experimental data.

3.2 Experimental

The XANES spectra were collected using the CAMD double crystal monochromator beam line.[3.21] The time-dependent reduction of Cu(II)O by 2-chlorophenol was monitored at 375 ^{o}C by X-ray absorption spectroscopy using a temperature-controlled dosing cell. The electron storage ring was operated with *ca.* 150 mA of beam current at injection, and the beam decayed over time with lifetimes of 4-8 hours. The monochromator provided photon flux of

~10^8 s^{-1}. The photon bandwidth was 2 eV, and the minimum monochromator energy step size in the region of the K-edge was approximately 0.3 eV. For these experiments the synchrotron radiation was monochromatized using a pair of Ge(220) crystals.

3.2.1 Dosing Cell

The temperature controlled dosing cell is shown in Figure. 3.2.[3.22] The cell consists of a stainless steel cube with six ports that accept 2.75 inch Conflat flanges at each face. In the center of the cell is a 6 cm^2 tungsten mesh (Buckbee-Mears) fastened between two copper posts that extend from the high current electrical feedthroughs. The mesh is composed of 0.05 mm diameter wire spaced in 0.22 mm intervals, with an optical transmission of approximately 80%. Substrate samples are supported on the grid and resistively heated. The surface temperature is measured with a 0.08 mm type K thermocouple spot-welded to the top center of the grid. A 22 amp variable transformer generates the current for resistive heating and is regulated by a temperature controller (Love Controls, Series 16 A) and a solid-state relay. Surface temperatures from ambient to 900 °C can be achieved. The transmission windows are 100 μm thick Kapton film sealed between flat Viton gaskets. The 2-chlorophenol dosant was introduced to the substrate via a septum capped dosing port. The base pressure of the cell was 10^{-6} Torr. One significant feature of this apparatus is the ability to rapidly heat and cool the sample, owing to the low heat capacity of the tungsten grid. The sample can be heated or cooled (i.e., quenched) in less than 5 seconds, permitting time dependent spectral studies in which the reaction was rapidly quenched, a spectrum was acquired, and the reaction was resumed by rapid heating to the original temperature.

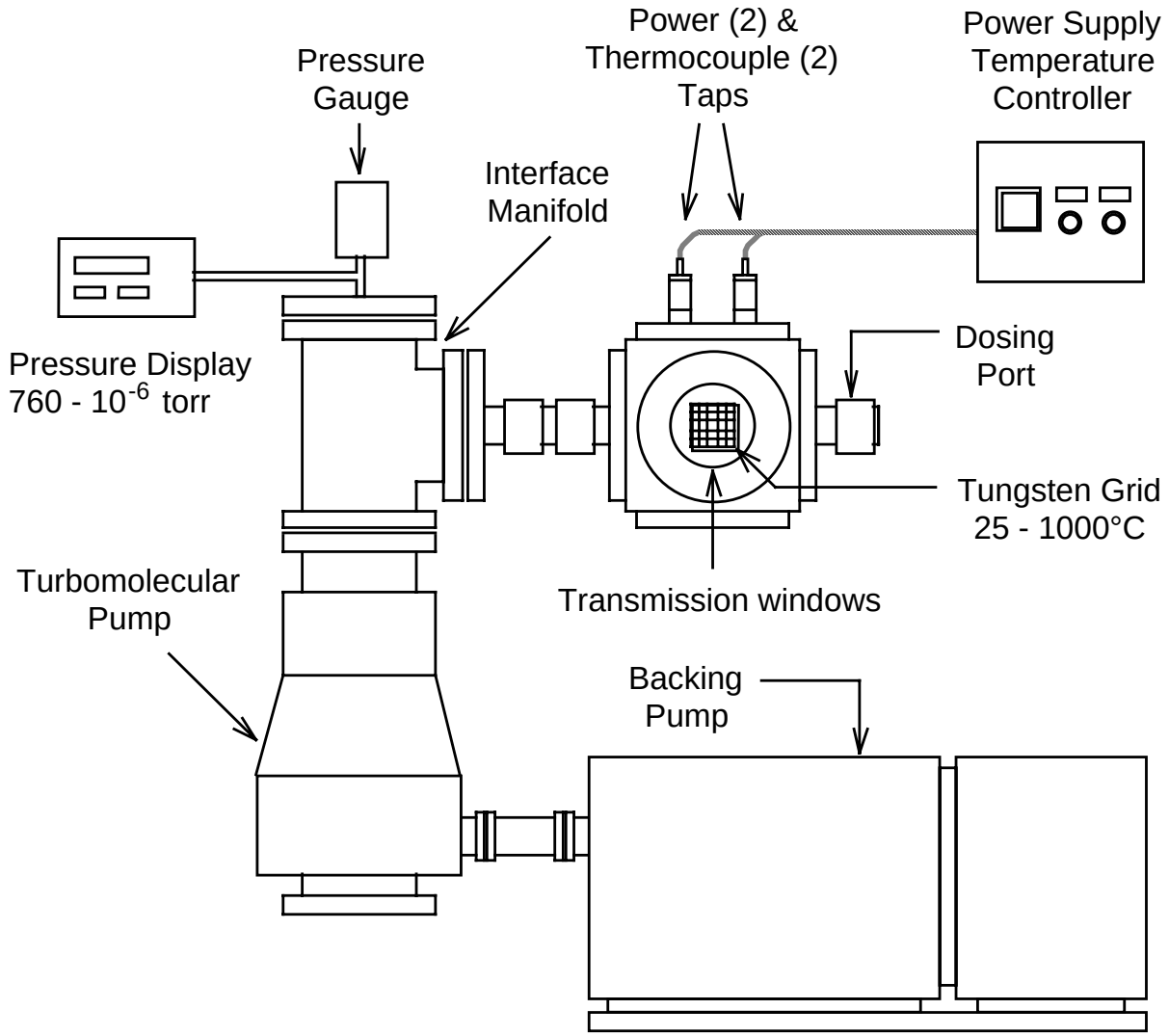

Figure 3.2 Experimental schematic of the endstation used at the end of the X-ray monochromator beam line.

3.2.2 Sample Preparation

The surrogate fly-ash substrate was composed of a mixture of Cab-O-Sil (Cole-Parmer) and <5 micron particle size Cu(II)O (Aldrich). Cab-O-Sil is a high purity, fumed silica with a surface area of approximately 250 m^2/g. An acetone slurry containing 0.17 g of each component was prepared using an ultrasonic bath. An atomizer was then used to evenly coat the entire tungsten mesh with a fine mist of the suspension. By heating the grid surface to ~70 °C the solvent was flash-evaporated leaving behind a uniform layer of the substrate over the voids in the very fine-mesh grid.[3.22] The total amount of powder deposited over the entire grid was typically 20-25 mg, and resulted in a sample of approximately 40% by weight copper in silica. Although this value is higher than typical fly-ash copper concentrations, the resulting large attenuation of the X-ray beam provided for high quality XANES spectra, thereby permitting precise determinations of chemical speciation in the substrate.

To ensure pseudo-first-order kinetics of adsorption with respect to the reactant, an excess of gas-phase 2-chlorophenol was used (0.68 Torr). Before acquiring spectra, the substrate was heated in air at 375 °C for 20 minutes to remove any remaining solvent and organic impurities in the material. It was determined that consistent data resulted if the substrate was first exposed to 2-chlorophenol at 375 °C for 20 minutes, then subjected to another surface cleaning cycle by heating in air at 350 °C for an additional 20 minutes, thus removing any chemisorbed reactant. The cell was evacuated to 10^{-5} Torr after each 20 minute exposure step. The reasons this 2-chlorophenol pretreatment is needed are not known, and quite clearly further investigations are needed to clarify how the substrate is affected by such a procedure. Whatever the cause, it is clear that the experimental protocol described above does result in consistent and reproducible data.

After completion of the substrate pre-treatment procedure, the cell was evacuated to 10^{-5} Torr and a XANES spectrum was taken of the unreacted Cu(II)O. Then, 60 μl of 2-chlorophenol was introduced through the dosing port. The sample temperature was rapidly raised to 375 °C and held for 2 minutes. The sample was then quickly cooled (<5 seconds) and a XANES spectrum taken. The heating, cooling, spectral acquisition cycle was repeated in 2-minute intervals until no further reduction in copper was observed-about 10 minutes. Prior to performing duplicate experimental measurements, the sample chamber was evacuated to 10^{-5} Torr to remove excess 2-chlorophenol and any volatile reaction products. The substrate sample was then exposed to air and held at 350 °C for 20 minutes in order to clean the surface of any adsorbed reaction products and to re-oxidize the reduced copper back to Cu(II). XANES spectra showed this treatment was sufficient to restore the copper to its original Cu(II) oxidation state .

3.3 Results

Representative transmission spectra taken at T = 375 °C during the course of reaction are shown in Figure 3.3. These data were acquired at the Cu K-edge, which illustrates a key point, i.e., X-ray spectroscopy allows one to obtain elementally specific information even under conditions where the element of interest is present in a complex mixture. The X-ray absorption edges of the other elements in the reaction mixture (i.e., C, O, Cl) are sufficiently distant in energy that they do not influence the Cu K-edge spectra. Only a few spectra are required to illustrate the trends in the evolving system, namely, a shift in the binding energy towards lower values, indicating a reduction of the Cu oxidation state as the experiment proceeded. The quality of the data permits the extent of the reaction to be quantified, and it will be shown it can determine substrate composition. It is possible to acquire data even more efficiently using rapid

scanning methods described elsewhere,[3.23,3.24] and using rapid scanning techniques could allow for closer time spacing of the data.

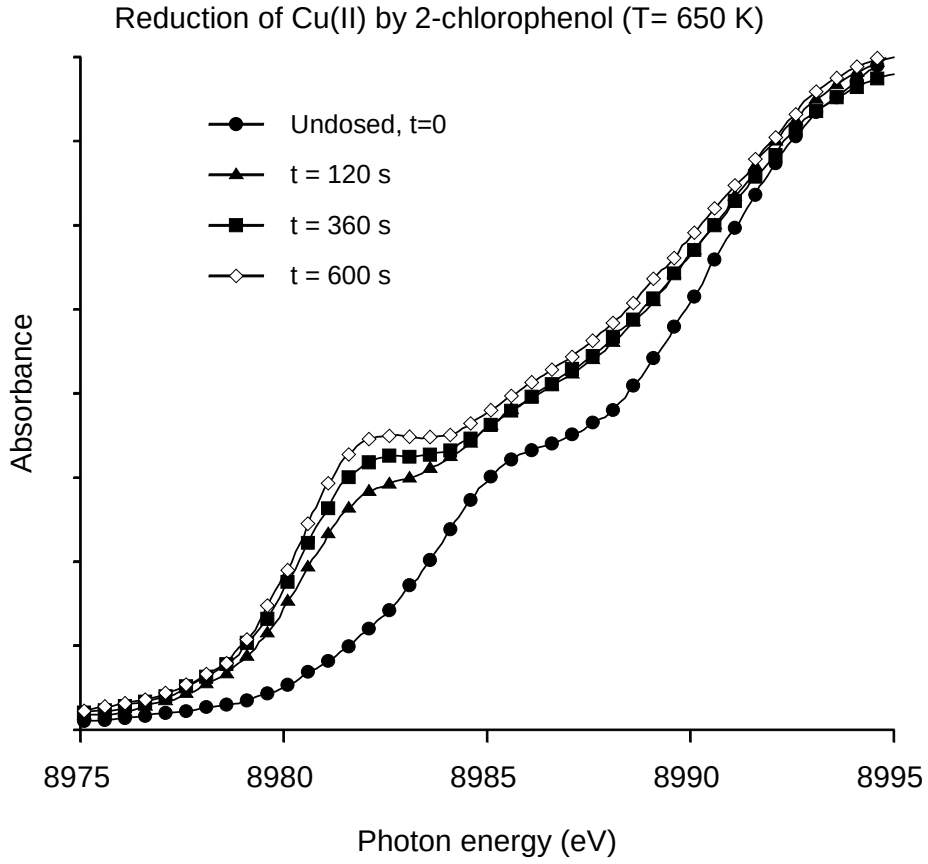

Figure 3.3 Absorption spectra of the CuO/Cab-O-Sil/2-chlorophenol mixture acquired at the Cu K-edge as a function of time following exposure to 2-chlorophenol.

The spectrum obtained for each time in the course of the reaction can be fitted to a superposition of spectra for Cu in three oxidation states as described in Section 3.1.2.2. At each

time in the reaction that a spectrum is obtained, the spectrum is fit, as shown in Figure 3.4, and the composition for each Cu species is plotted as a function of time (Figure 3.5).

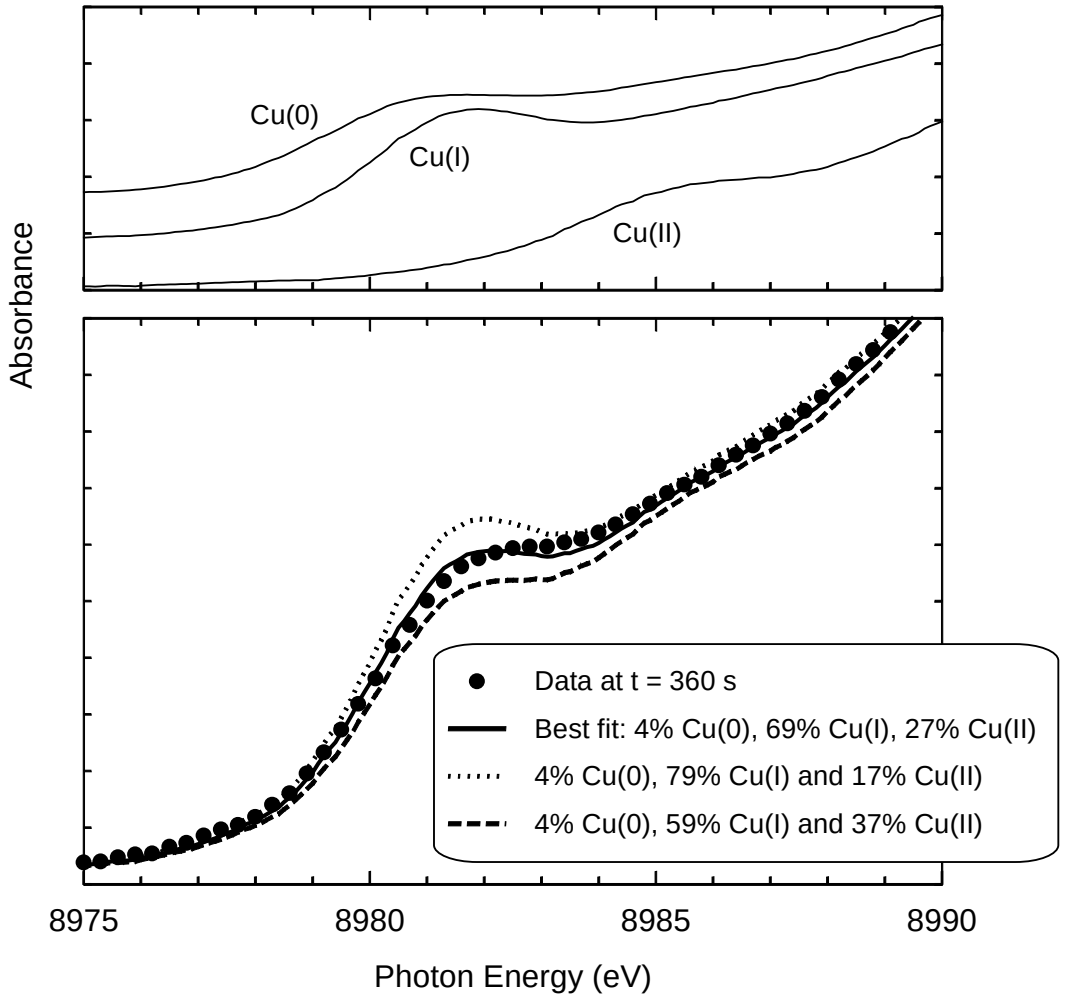

Figure 3.4 Top frame: Absorption spectra of standards (Cu metal, $Cu(I)_2O$, and Cu(II)O). Bottom frame: A typical spectrum with different fits. It is clear that we can estimate the composition to within a few percent with good accuracy. Fits such as those shown in the bottom frame are performed for each time point in the reaction and are plotted to chart the course of the reaction.

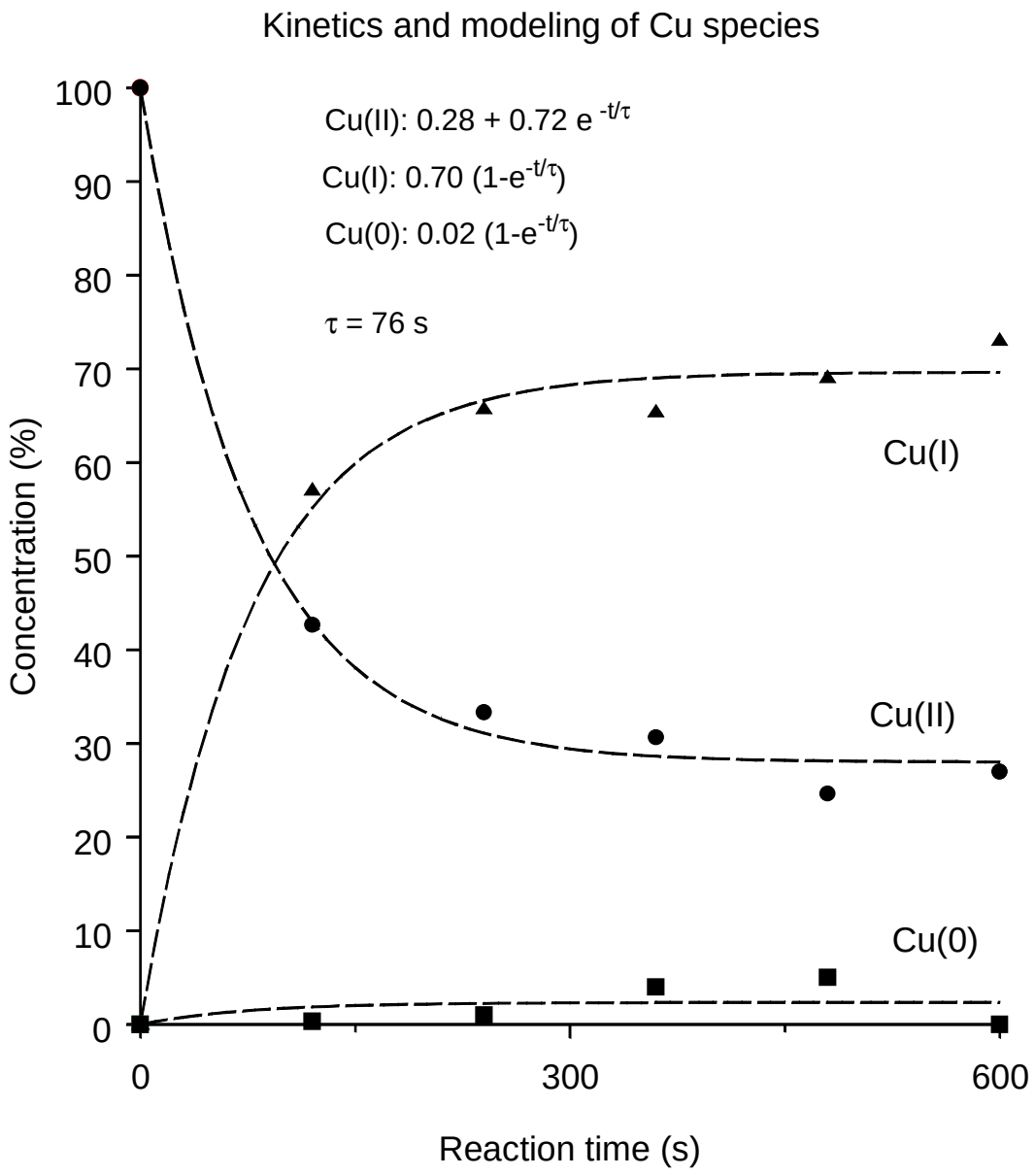

Figure 3.5 Experimental compositions as a function of time following exposure of Cu(II)O to 2-chlorophenol.

The data were fitted with a commercial least-squares fitting program. The equations used for the fit are shown in Figure 3.6, and the errors are reported to two standard deviations. The fit was performed with a first-order kinetic model (Figure 3.6) that is consistent with the data in Figure 3.5.

$$f_2(t) = (1 - f^{reac}) + f^{reac} \exp [-t/\tau]$$

$$f_1(t) = f^{reac} f^{12} [1- \exp [-t/\tau]]$$

$$f_0(t) = f^{reac} (1- f^{12}) [1- \exp [-t/\tau]]$$

where: $f_2(t)$ = fraction of Cu present as Cu(II) at time t,

$f_1(t)$ = fraction of Cu present as Cu(I) at time t,

$f_0(t)$ = fraction of Cu present as Cu(0) at time t,

f^{reac} = fraction of Cu(II) that is available for reaction = 0.72 ± 0.02,

f^{12} = fraction of the available Cu(II) that reacts to form Cu(I) = 0.97 ± 0.02,

τ = time constant for depletion of Cu(II) = 76 ± 12 s

Figure 3.6 Kinetic model equations used for least-squared analysis of the copper concentration.

Three important outcomes have resulted from these XANES studies. *First*, it appears that most, but not all, of the copper reacts. This is evident from the observation that some residual Cu(II) remains unreduced even after the reaction has proceeded to apparent completion. In the case of the samples studied here, 72% of the Cu(II) was converted to Cu(I) or Cu(0) with 28% left unreacted. The large extent of reaction implies that as 2-chlorophenol reacts at surface oxide sites; additional copper oxides migrate from the interior to replenish the reacted surface oxides. Repeating the experiment with larger grains of Cu (II) oxide, whose lower surface-to-

volume ratio may limit the extent of reaction, are warranted to determine why the extent of reaction was so large, but still incomplete.

Second, it appears that there are two reaction pathways involving electron transfer to copper, as the Cu(II) is being reduced to both Cu(I) and Cu(0). It is clear that most of the reacted copper is forming Cu(I) rather than Cu(0). The percentage of Cu(0) is small, and consequently, is not precisely determined. As a result, it is unclear if the rate of formation of the Cu(I) and Cu(0) are characterized by the same time constant. Since the simplest kinetic model assumes the same time constant and this reduces the number of adjustable parameters, a single time constant was used for data reduction. The point is that not too much significance should be ascribed to the use of a single time constant.

Third, the data indicate that the dominant surface-mediated mechanism is consistent with a single electron transfer mechanism, rather than a 2-e^- pathway, as 2-e^- pathways would result in reduction to Cu(0). Thus the proposed pathway that is most consistent with the observed data is pathway b in Figure 3.1.

In summary, these XANES data provide critical information, and can help in understanding the detailed microscopic mechanism of PCDD/F formation via surface-mediated processes. This is the first report of this XANES application, which has provided the first *in-situ* probe of copper reduction by a PCDD/F precursor. While the current data do not definitively select one of the proposed mechanisms, they do provide useful guideposts for informed speculation regarding likely reaction pathways in analogy to the way in which methanol-induced reduction of CuO provided clear and useful information on related catalytic mechanisms.[3.25,3.26] It has been shown that 2-chlorophenol reacts with Cu(II)O/silica under conditions that are known to be favorable to formation of PCDD/F. Cu(II) is reduced primarily to Cu(I) which in

conjunction with other reported studies [3.12,3.13] implies the formation of a surface-associated phenoxyl species that can react to form PCDDs or PCDFs, depending upon whether the reaction is with a gas-phase chlorophenol or another surface-associated phenoxyl species, respectively. Additional XANES and EXAFS studies of these surfaces are needed to better understand the nature of the binding and local environment of PCDD/F precursors. The demonstration project described here will be extended to temperature-dependent measurements, as well as studies of other precursors, other substrates, and related X-ray absorption methods, including EXAFS spectroscopy to provide detailed structural information.

3.4 References

3.1 Farquar, G. R.; Alderman, S. L.; Poliakoff, E. D.; Dellinger, B. X-ray spectroscopic studies of the high temperature reduction of Cu(II)0 by 2-chlorophenol on a simulated fly ash surface. *Environmental Science & Technology* **2003**, *37*, 931-935.

3.2 Yamaguchi, A.; Shido, T.; Inada, Y.; Kogure, T.; Asakura, K. et al. Time-resolved DXAFS study on the reduction processes of Cu cations in ZSM-5. *Catalysis Letters* **2000**, *68*, 139-145.

3.3 Wehrmeier, A.; Lenoir, D.; Sidhu, S. S.; Taylor, P. H.; Rubey, W. A. et al. Role of copper species in chlorination and condensation reactions of acetylene. *Environmental Science & Technology* **1998**, *32*, 2741-2748.

3.4 Fiedler, H. Thermal formation of PCDD/PCDF: A survey. *Environmental Engineering Science* **1998**, *15*, 49-58.

3.5 Addink, R.; Altwicker, E. R. Role of copper compounds in the de novo synthesis of polychlorinated dibenzo-p-dioxins/dibenzofurans. *Environmental Engineering Science* **1998**, *15*, 19-27.

3.6 Altwicker, E. R. Relative rates of formation of polychlorinated dioxins and furans from precursor and de novo reactions. *Chemosphere* **1996**, *33*, 1897-1904.

3.7 Stieglitz, L. Selected topics on the de novo synthesis of PCDD/PCDF on fly ash. *Environmental Engineering Science* **1998**, *15*, 5-18.

3.8 Xhrouet, C.; Pirard, C.; De Pauw, E. De novo synthesis of polychlorinated dibenzo-p-dioxins and dibenzofurans an fly ash from a sintering process. *Environmental Science & Technology* **2001**, *35*, 1616-1623.

3.9 Sidhu, S. S.; Maqsud, L.; Dellinger, B.; Mascolo, G. The Homogeneous, Gas-Phase Formation of Chlorinated and Brominated Dibenzo-P-Dioxin from 2,4,6-Trichlorophenols and 2,4,6-Tribromophenols. *Combustion and Flame* **1995**, *100*, 11-20.

3.10 Evans, C. S.; Dellinger, B. Mechanisms of dioxin formation from the high-temperature pyrolysis of 2-chlorophenol. *Environmental Science & Technology* **2003**, *37*, 1325-1330.

3.11 Xhrouet, C.; Nadin, C.; De Pauw, E. Amines compounds as inhibitors of PCDD/Fs de novo formation on sintering process fly ash. *Environmental Science & Technology* **2002**, *36*, 2760-2765.

3.12 Lomnicki, S.; Dellinger, B. Formation of PCDD/F from the pyrolysis of 2-chlorophenol on the surface of dispersed copper oxide particles. *Proceedings of the Combustion Institute* **2003**, *29*, 2463-2468.

3.13 Lomnicki, S.; Dellinger, B. A detailed mechanism of the surface-mediated formation of PCDD/F from the oxidation of 2-chlorophenol on a CuO/silica surface. *Journal of Physical Chemistry A* **2003**, *107*, 4387-4395.

3.14 Doomes, E. X-Ray Spectroscopy of Geometrically Constrained Systems. In *Chemistry*; Louisiana State University: Baton Rouge, 2003; pp 141.

3.15 Sinfelt, J. H.; Meitzner, G. D. X-Ray Absorption-Edge Studies of the Electronic-Structure of Metal-Catalysts. *Accounts of Chemical Research* **1993**, *26*, 1-6.

3.16 Sarret, G.; Connan, J.; Kasrai, M.; Eybert-Berard, L.; Bancroft, G. M. Characterization of sulfur in asphaltenes by sulfur K- and L- edge XANES spectroscopy. *Journal of Synchrotron Radiation* **1999**, *6*, 670-672.

3.17 Kasrai, M.; Brown, J. R.; Bancroft, G. M.; Yin, Z.; Tan, K. H. Sulphur characterization in coal from X-ray absorption near edge spectroscopy. *International Journal of Coal Geology* **1996**, *32*, 107-135.

3.18 Ressler, T. WinXAS: a program for X-ray absorption spectroscopy data analysis under MS-Windows. *Journal of Synchrotron Radiation* **1998**, *5*, 118-122.

3.19 www.microsoft.com.

3.20 Attwood, D. *SOFT X-RAYS AND EXTREME ULTRAVIOLET RADIATION*; Cambridge University Press: Cambridge, 2000; 470.

3.21 Schilling, P. J.; Morikawa, E.; Tolentino, H.; Tamura, E.; Kurtz, R. L. et al. Installation and Operation of the Lnls Double-Crystal Monochromator at Camd. *Review of Scientific Instruments* **1995**, *66*, 2214-2216.

3.22 Basu, P.; Ballinger, T. H.; Yates, J. T. Wide Temperature-Range Ir Spectroscopy Cell for Studies of Adsorption and Desorption on High Area Solids. *Review of Scientific Instruments* **1988**, *59*, 1321-1327.

3.23 Floriano, P. N.; Noble, C. O.; Schoonmaker, J. M.; Poliakoff, E. D.; McCarley, R. L. Cu(0) nanoclusters derived from poly(propylene imine) dendrimer complexes of CU(II). *Journal of the American Chemical Society* **2001**, *123*, 10545-10553.

3.24 Bornebusch, H.; Clausen, B. S.; Steffensen, G.; Lutzenkirchen-Hecht, D.; Frahm, R. A new approach for QEXAFS data acquisition. *Journal of Synchrotron Radiation* **1999**, *6*, 209-211.

3.25 Gunter, M. M.; Ressler, T.; Jentoft, R. E.; Bems, B. Redox behavior of copper oxide/zinc oxide catalysts in the steam reforming of methanol studied by in situ X-ray diffraction and absorption spectroscopy. *Journal of Catalysis* **2001**, *203*, 133-149.

3.26 Gunter, M. M.; Bems, B.; Schlogl, R.; Ressler, T. In situ studies on the structure of copper oxide/zinc oxide catalysts. *Journal of Synchrotron Radiation* **2001**, *8*, 619-621.

Chapter 4: Coincidence Time of Flight Zero Kinetic Energy Velocity Map Imaging

4.1 Introduction

This chapter is concerned with the design of, and preliminary results from, a time of flight (TOF) zero kinetic energy velocity map imaging (VMI) system. There are no examples in the literature where the unambiguous lineage of two chemically identical daughter ions (the same atomic mass) produced from different parent molecules have been determined. The ambiguity resulting from this limitation has hindered the study of decompositions of clusters larger than dimers.[4.1,4.2]

This limitation becomes clear in the following thought experiment: Consider the ionization of a 50/50 mixture of Ar_5 and Ar_6. These gas clusters are cooled with a gas jet expansion as described in Chapter 2. A mass spectrum of this mixture shows clusters of all sizes, from the Ar monomer though the Ar hexamer. The lower mass Ar species result from fragmentation of larger clusters that are a consequence of the ionization required of mass spectrometry. One of the products of this fragmentation is the Ar_5/Ar ion pair resulting from Ar_6 fragmentation. If the desired information is the spectra of initially present Ar_5 parent molecules, or its fragmentation products, current mass spectrometry would yield ambiguous information because of the presence of many daughter clusters. One view to take is that this limitation is based on the fact that the ions in a conventional mass spectrometer are resolved by ion mass not by any feature of the initial parent.

In this thought experiment no kinetic energy information was collected about the fragmented ions. In fact, the Ar_5 daughter of Ar_6 will have additional energy and thus velocity from the exploding of the cluster. This energy is the key to the proposed method

to determine the parentage of the ion. The details of how this is done will be discussed in section 4.1.2. By focusing on zero kinetic energy results as opposed to the energetic fragments, a spectrum of non-fragmented ions can be obtained.

The apparatus we describe combines techniques developed in Chapter 2 and Chapter 3 with a TOF-VMI reported by Eppink *et al*.[4.3] Specifically, supersonic gas jets used in Chapter 2 will be combined with the use of a skimmer which allows only the center of the expanding gas to enter the downstream chamber, greatly lowering the temperature of the target gas (and reducing the gas load on the interaction region vacuum chamber).

The goals of this work are to design and construct an apparatus to conduct zero kinetic energy velocity map imaging experiments. To accomplish these goals several intermediate results are presented: ion focus simulations, benchmarks for zero kinetic focusing spots, calculating detection limits and a demonstration of the instrument resolution. The project's final goals require a modified application of the XANES technique described in Chapter 3. Combining these techniques will create a novel application of mass spectrometry. Several other applications may also be possible by using this technique in other areas, such as the positive identification of parent ions in biological time of flight mass spectrometry. The work presented here is the first step toward the ultimate goal of this project, which is the application of VMI to identify the molecular origin of the various constituents in daughter ion mixtures.

4.1.1 Time of Flight Mass Spectrometry

Mass spectrometry separates species of chemical interest by their mass-to-chargeratio. A large variety of experimental techniques are used to accomplish this mass

separation, including quadrupole, ion cyclotron, ion trap, and time of flight mass spectrometry (TOF). Quadrupole, ion cyclotron and ion trap mass selection techniques alter the trajectory of the ions and are not suitable for velocity map imaging techniques. Time of flight is currently the only mass-selective technique suitable for VMI and will be the principal technique discussed in this chapter.

The first mass spectrum was observed by J. Thompson in 1912 with the use of an apparatus similar to a cathode ray tube with electric fields perpendicular to the ions' trajectories to alter their paths. Deflection is obviously related to the atomic mass.[4.4] Time of flight mass spectrometry was first used in 1946 by Stephens.[4.4]. In this method the speed of the molecule and so its time of flight to the detector is related to the mass of the ion. The use of time of flight mass spectrometry as a practical tool was not realized until 1955 with the advent of space focusing optics by Wiley and McLaren at the Bendix Avation Company.[4.5] Space focusing allowed for a dramatic improvement in resolution by focusing ions onto the detector in time, and independent of the initial point of creation. Space focusing imparts energy on the ions depending on the location of the formation in the source, in conjunction with a second optical element to add a constant acceleration to all created ions. The combined effect of the two optical elements reduces the time spread of ion detection for a given mass by causing ions created further from the detector to gain more energy and "catch up" to those with less distance to travel. From the advent of the first space focused time of flight mass spectrometer a dramatic revolution in resolution and the upper end of mass determination has occurred.[4.6] The original space focusing article reported a resolution of 200. One of the issues involved in the use of the various methods is resolution, which is defined as detected mass over the change in mass, in

atomic mass units (amu). Current commercially available instrumentation achieves a resolution of greater than 10,000.[4.7]

Theoretical considerations for time of flight mass spectrometry are based on the fact that when a particle is accelerated to a given energy and allowed to travel a known distance the mass of the particle can be determined using the time of travel. In practice the particle is created in a region with a constant field and the time measurement is started when the ion is created. The start time can be determined though detection of the incident photons in a pulsed source or the detection of an electron from the ionization event. For synchrotron studies, and any continuous ionization source, the preferred method is to use the photoelectron as the start signal. This method is termed coincidence, based on the use of electrons and ions as start and stop signals, as opposed to using an event external to the creation of the photoion photoelectron pair. With the collection of a flight time and a known flight distance the mass of an ion can be determined. A representation of a time of flight apparatus is shown in Figure 4.1.

The kinetic energy equation (Equation 4.1) is the basis for the determination of mass from time and distance. A brief derivation of the time of flight equation from the kinetic energy follows. By solving Equation 4.1 for velocity and replacing velocity by distance per time, an expression for time of flight is shown to be dependent on the square root of mass (Equation 4.2). Equation 4.2 can be represented in volts and number of charges for multiply charged species. This form of the equation allows for a more practical representation of the time of flight, i.e. the common experimenter does not apply joules of energy but rather an electric potential (Equation 4.3).

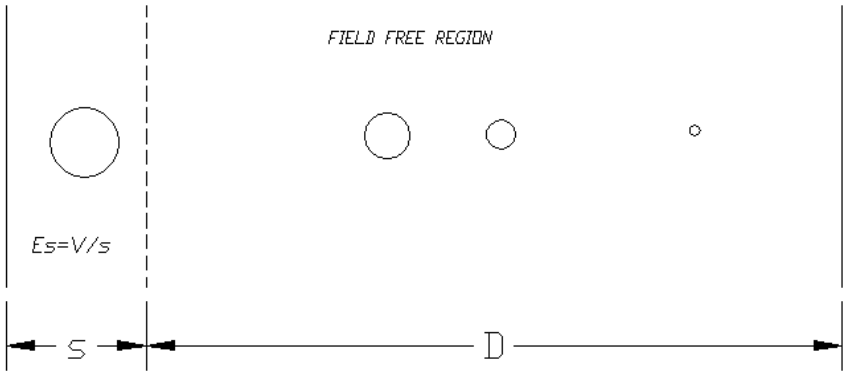

Figure 4.1 Schematic of TOF showing the extraction region (s), field free region (D), and relative ion spacing (shown with circles). Smaller circles represent lower mass ions with higher velocities and lower times.

$$E(j) = \frac{1}{2} m(kg) v^2 (m/s)$$

Equation 4.1 The equation for kinetic energy.

$$t = \left(\frac{m(kg)}{2E(j)} \right)^{\frac{1}{2}} D(m)$$

Equation 4.2 Mass dependent equation for the flight time of an ion through a field free region of distance (D).

$$t(s) = \left(\frac{m(kg)}{2zeEs(V)} \right)^{\frac{1}{2}} D(m)$$

Equation 4.3 Time of flight equation in practical units: the number of charges on an ion (z), electric field in volts (Es), mass in kg (m), distance in m (D) and e= 1.603×10^{-19}C.

In summary, if all particles in a system are given the same energy, the lighter ones will travel faster. This fundamental property can be used to separate ions by mass. To determine the mass of the ion, the velocity along the flight tube needs to be known. The velocity is determined by the time of flight and the distance traveled. If the ion has a velocity perpendicular to the flight tube the flight time will not change. The apparatus in this chapter uses TOF coupled to the VMI technique described in section 4.1.2.

4.1.2 Velocity Map Imaging

Velocity map imaging separates ions based on the velocity perpendicular to the flight tube. If an ion has a velocity perpendicular to the flight tube it will not strike the center of the detector. By selecting only the ions that strike the center of the detector a spectrumof zero kinetic (perpendicular) energy ions is collected. The remainder of this section will discuss the history of ion imaging and the ion optics needed to focus the ions.

Ion imaging techniques have dated from the early days of cathode ray tube development. When a stream of charged particles is exposed to a magnetic or electric field the position of impact on a phosphor screen is dependent on the mass of the gas molecule in the tube.[4.8] This early method used an image to determine the velocity imparted on an ion by an external field perpendicular to the main direction of travel in order to determine the mass. More modern advancements have used the application of a field free drift tube and focusing image ion optics to determine the initial velocity of an ion.[4.3] With these advancements all ions with initial velocities perpendicular to the axis of the flight tube are mapped onto the same radial position on a two-dimensional detector. The power of VMI has created a lot of interest in many possible new applications in recent years.[4.9-15]

The most significant difference between conventional TOF and VMI is in the design of the acceleration optics. In conventional TOF the acceleration optics serve as the energy source for the ions. VMI uses the acceleration optics as electrostatic lenses for focusing as well as the energy source. Electrostatic lenses have been studied in great detail with the emphasis on a small focal spot size.[4.16,4.17]

The need for focusing arises because there is a finite ionization volume for all photon ionization events. In a perfect system where all ions are created at a point in space there would be no need to focus. When ionizing a gas sample with incident photons the ionization volume is defined by the overlap of the gas beam and photon source. Any spread of the initial ionization volume would have the effect of blurring the image on the detector. To overcome the problem of blurring a focusing system of ion optics is used. The focusing effectively removes the initial position dependence on the final detection location. All ions of the same initial velocity will be mapped the same distance from the center of the detector. Ions with an initial velocity of zero will impact the center and higher energy ions will be detected further from the center.

Imaging optics requires the absence of an acceleration grid, allowing the field lines to penetrate the adjacent field. Acceleration grids are composed of a wire mesh with a high transmission used in place of open apertures. The use of an acceleration grid limits field line penetration. Field penetration occurs when the electric field of one region “spills over” into the adjacent region. Without field line penetration there would be no focusing properties. This penetration causes curves in the field that can be optimized for image focusing conditions. A simulated ion-focusing lens is shown in Figure 4.2. The representation of the focusing optics and flight tube are a slice through

the middle of the tube along the flight axis. The elevations shown represent the potential energy or electric field in the corresponding region.

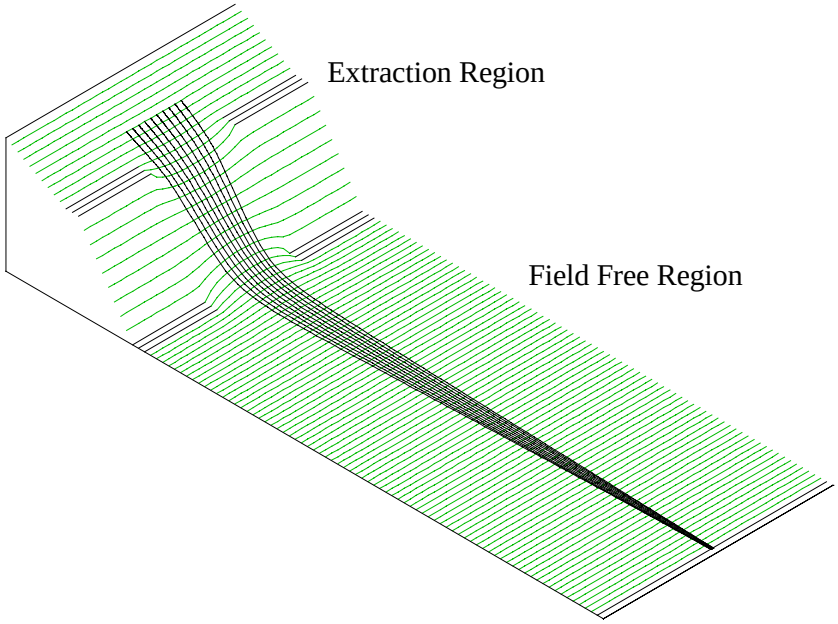

Figure 4.2 Simulated ion focusing lens. Ions are represented as black lines with zero kinetic energy perpendicular to the flight tube. Potentials for the flight tube are from left to right: ground, -100V,-370V. Simulations were performed with the commercially available program SimIon 3D 7.0.[4.18]

As can clearly be seen in Figure 4.2 the ions are in focus at the end of the field free region. It is apparent that the field lines from the extraction region penetrate adjacent fields. The field line penetration can be seen in the curves near the acceleration optics (in the field free region the field lines are straight). The shape of this penetration is similar to a conventional optical focusing element. The ability to focus ions onto a 2-dimensional plane with initial energy distributions being preserved was originally shown to be possible in 1997.[4.3] This can be clearly shown for ions having an initial kinetic energy perpendicular to the flight tube (Figure 4.3). By rotating the two-dimensional plane

about the length of the flight tube it is clear that the image of an ion with a given perpendicular kinetic energy will form a ring on the two-dimensional detector.

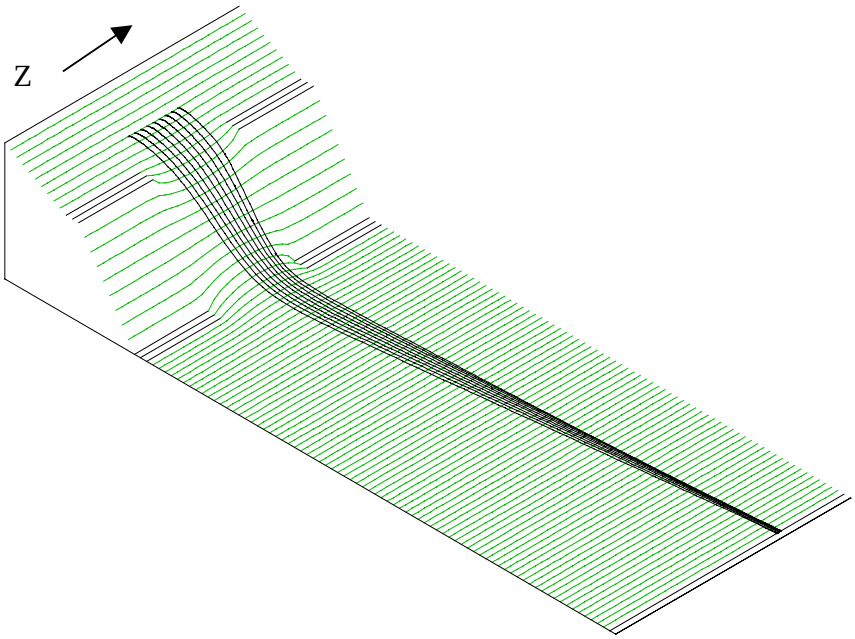

Figure 4.3 Ion flight simulation with an initial kinetic energy in the Z direction of 1.5 eV.

Before any construction of the experimental apparatus, it was deemed necessary to conduct a series of simulations to aid in the complete characterization of the apparatus. In order to determine the conditions available for focusing the flight tube, a series of simulations were conducted. The simulations showed that an infinite number of focusing conditions existed (Figure 4.4). The advantage of being able to change focusing conditions occurs when there is a need to change the total energy imparted on the ions. This change in energy changes the flight time and also changes the mapping position for an energetic ion. With a higher total energy an ion will have its perpendicular energy mapped closer to the flight tube axis. This is an effect of reducing the time available for

the ion to travel to the detector. The direct application of this technique will allow for ions close to the center of the detector to be mapped further out and simplify the data reduction. The simulations showed that the ability to map energetic species extended beyond 1 eV.

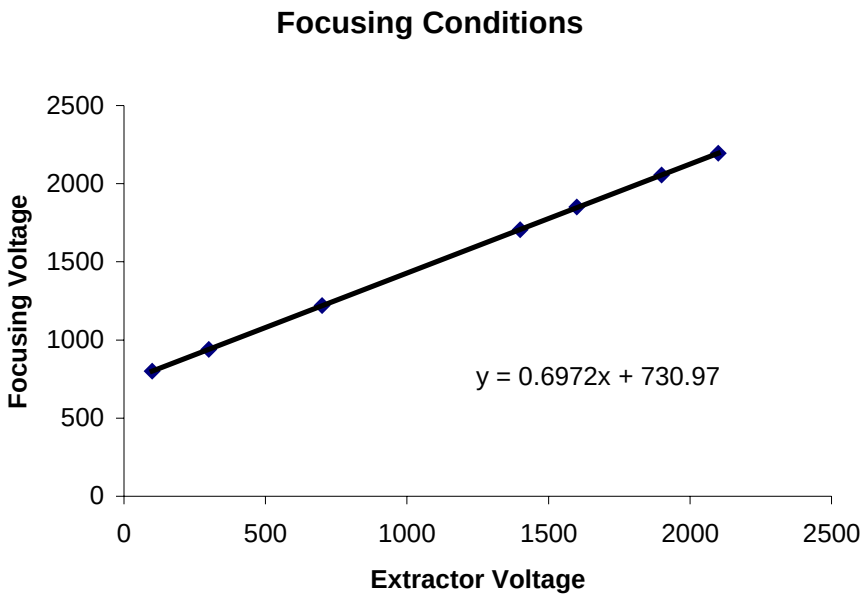

Figure 4.4 Simulated focusing conditions. As the extractor voltage decreases, the ion flight time will increase, allowing for lower energy ions to be mapped further from the center of the detector. Any value from the above plot will have the ions in focus, allowing the experimenter to select from a range of acceleration voltages.

4.1.3 Position Sensitive Detector

To determine the position of the imaged event, a position sensitive delay line anode was used. The delay line consists of two pairs of copper wires supported by a ceramic mount directly behind a micro channel plate stack. Each pair of wires consists of a signal and reference line for X and Y outputs. The reference line was held at ~25 volts above the signal line. When a signal reached the delay line the electrical charge traveled

to both ends of the wire. To determine the position of an electron cascade a time was determined for each pulse pair for a single wire. The time for a signal to travel a distance on a given wire was a constant.[4.19] A single wire example of the delay line detection method is shown in Figure 4.5. For each electron cascade, four stop pulses were produced: X1, X2, Y1, and Y2 stop. The difference in arrival time was used to determine the X and Y positions of the original event. For the application of TOF-VMI the start time for the delay line was the start of the TOF. The delay line stop pulses were also used to determine the total time of flight. This was done by dividing the sum of the stop times by four, yielding a TOF.

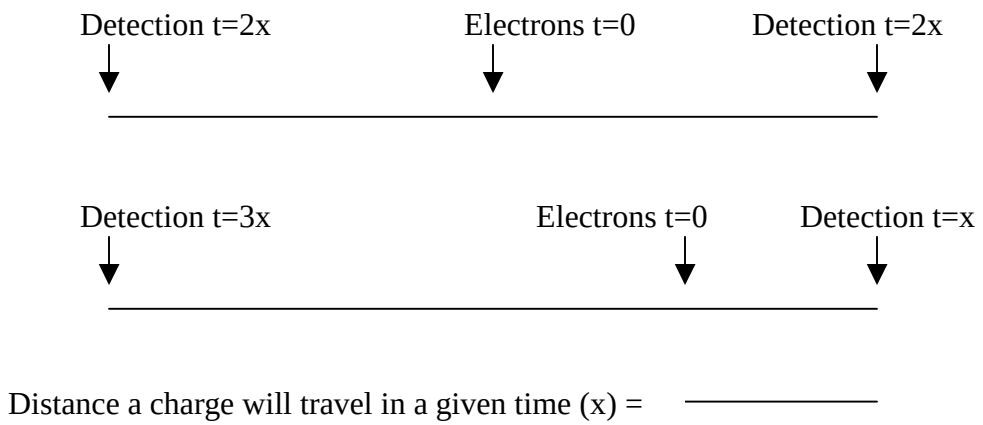

Figure 4.5 Illustration showing position determination on a delay line detector. In the top illustration a charge hit the center of a wire and is detected at the same time at both ends. Below a charge hits ¾ down a wire and the charge is detected at different times. Determining the time of detection events can determine the initial position of the charge.

4.1.4 Experimental Goals

The ultimate experimental goal will not be to determine the velocities of energetic species but to use a combination of the above techniques to sort out zero energy species from energetic ones. This new use will allow the separation of parent ions from daughter

ions of the same chemical species. The results presented here demonstrate the ability of the apparatus to effectively focus a zero energy ion event and to produce calibration spectra for use in subsequent experiments. In addition a demonstration of the resolution obtainable is shown, along with the ability to determine the components of a mixture of gases in the range of 1-4%. All of the initial goals of this experiment have been achieved with great success as can be clearly seen in the results section. The results also provide a set of benchmarks for future use. The preliminary results will allow many future graduate students to have a prosperous experimental experience.

4.2 Experimental

Focusing and time of flight calibration spectra were collected using the 6-m toroidal grating monochromator at CAMD.[4.20] Gases used for the initial calibration were Ar, He and air. For calibration the incident photons were 17 eV. Typical ring current was 80 mA and the lifetime was ~8 hours.

The TOF-VMI optics were modeled on designs by Eppink and Parker. The time of flight tube and mounting system were new and custom designed. Several other components were also newly constructed, including the thin window pumping chamber, experimental chamber, skimmed beam chamber, and the ion optic mounting system.

The experimental chamber used has three distinct regions: skimmed molecular beam, interaction region and ultra high vacuum region. Technical drawings for the TOF-VMI and skimmed molecular beam region are included in Appendix C. A skimmed molecular beam region allows for the introduction of gasses under high pressure and high throughput while limiting the pressure in the interaction region chamber. Without the use of a skimmer the pressure in the interaction region chamber would be above the operating

pressure of the MCPs. Downstream from the molecular beam production is the interaction region with time of flight and imaging capabilities. Finally, an ultra high vacuum region with an aluminum window is used to maintain the beam line pressure and allow the incident photons to enter the interaction region.

In the skimmed molecular beam region sample gas was introduced with a gas jet (typical size = 30 μm) on an xyz translator. To remove the skimmed gas a 1500 l/s turbo molecular pump was used. To accomplish the beam skimming a 1.5 mm type A skimmer (Beam Dynamics Inc.) was mounted on a flange before the interaction region.

The heart of the experiment is the interaction region, where sample gas and photons interact and the resulting ions are imaged with time resolution. A schematic of the TOF-VMI is shown in Figure 4.6. The gas from the skimmer was introduced at 90° to the incident photons. A 500 l/s turbo molecular pump was employed for vacuum conditions. The base pressure was 10^{-8} Torr. Gas and photons crossed in the interaction region between the extraction and focus electrodes. The space separation between the extraction, focus and field free optics was 15 mm each. All focusing optics were 2 mm thick with a 20 mm aperture. To provide a uniform field between the interaction region and the electron detector a high transmission mesh was used in place of an open aperture. To further reduce any field distortions the optic spacers were shielded by metallic tubes with an electrical break 7.5 mm from each plate. Electron detection was accomplished with a chevron MCP stack. Ion detection was performed with an 80 mm chevron MCP stack coupled to a delay line anode from Roentdek.[4.21] A schematic of the detailed electronic connections and voltages is shown in Figure 4.7.

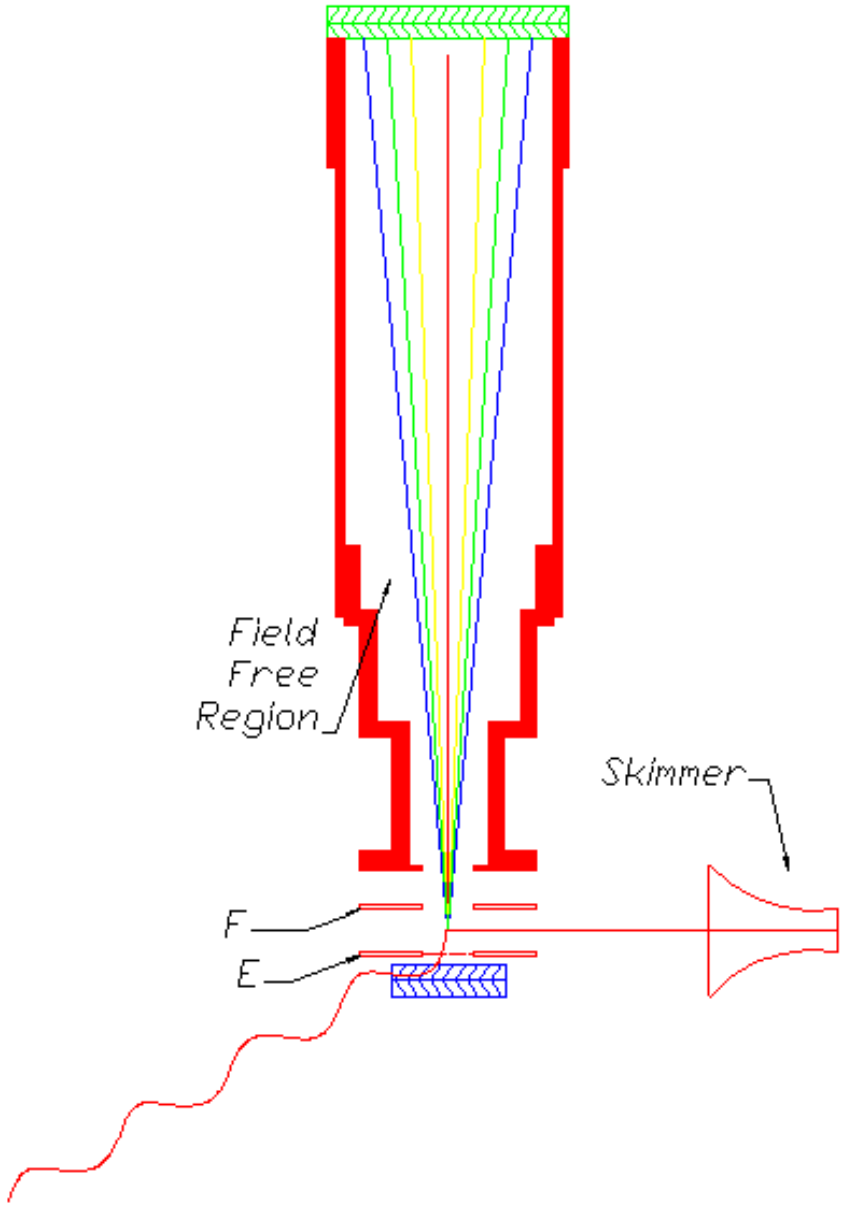

Figure 4.6 TOF imaging flight tube with all major components shown. The sample gas and photons are shown as red lines. Ion and electron detectors are shown in green and blue, respectively. Field regions are extraction (E), focusing (F) and field free region. Ion separation is illustrated with red (low energy ions) to blue (high energy ions) lines.

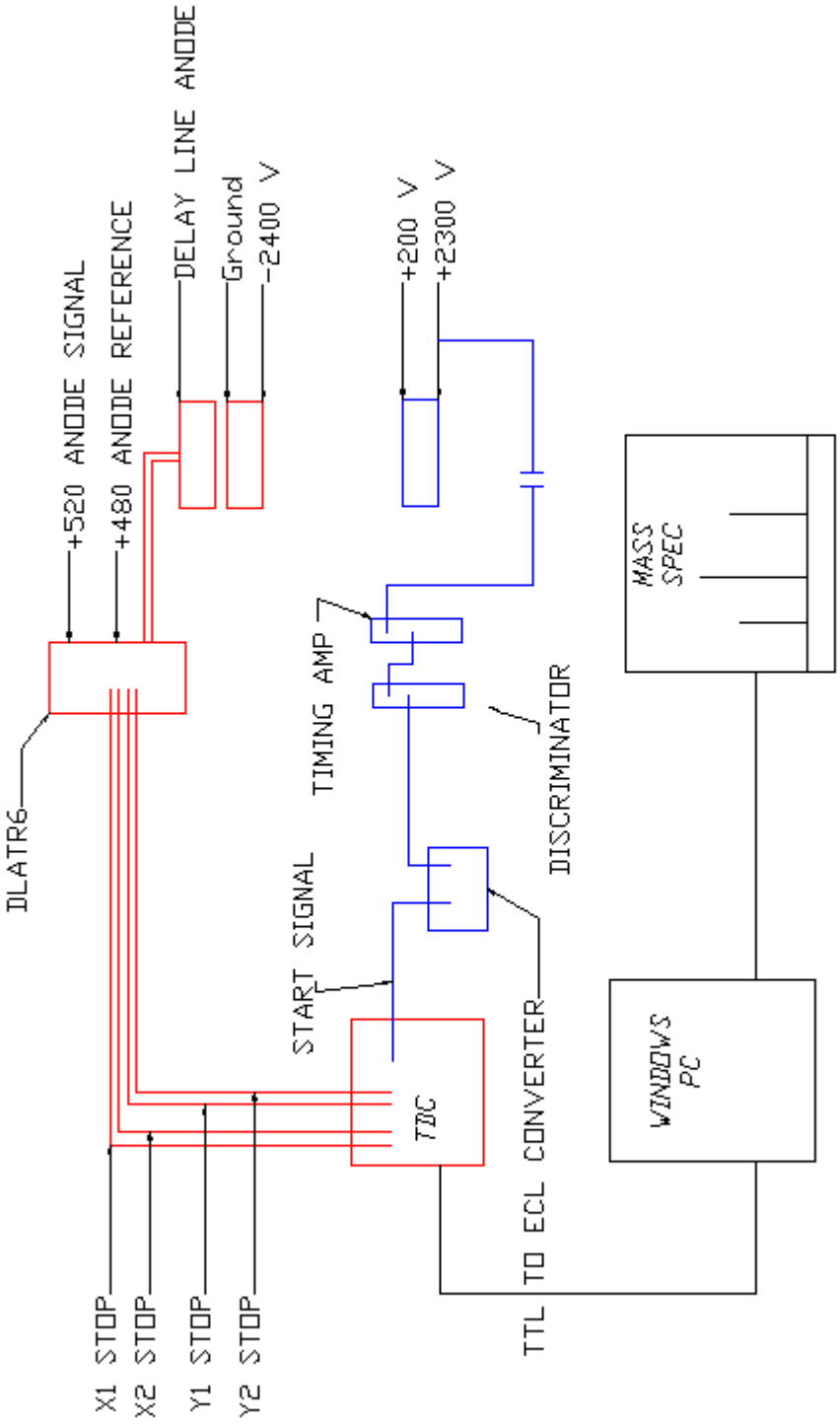

Figure 4.7 Detailed schematic of ion and electron electronics. Ion detection is shown in red and electron detection is shown in blue.

To couple the experimental apparatus to the beam line an aluminum window was used (Luxel Corporation). This region had a small gas load due to the chamber walls and was pumped by a 60 l/s turbo pump to achieve an operating pressure of 10^{-9} Torr. To accomplish baking in a quick manner a solid 2.75 inch gate valve isolated the ultra high vacuum region. The location of the valve was between the experimental chamber and the thin window.

The TOF data collection system is best explained by breaking it down into the principal components of ion and electron signals. As mentioned above a photoion photoelectron pair is generated in the interaction region and directed to their respective MCP detectors. Electron detection was done through a combination of commercially available stand-alone electronic components. Once the electron cascade from the MCP was collected onto the anode, the signal was picked off the high voltage supply line through a capacitor. The capacitor was necessary for the subsequent electronics, as they are not rated for high voltages. The electron signal was then amplified through a series of timing amplifiers. The amplified signal was directed to a gateable constant fraction discriminator for signal processing. Signal processing at the discriminator selects a set voltage peak height to process for output. By selecting a signal height above the noise, false signals are filtered out. The discriminated pulses were then internally converted to a TTL signal and routed to a TTL to ECL converter. The electron ECL pulse was used as the timing start in the time to digital converter.

Ion collection was accomplished through a purchased position sensitive detector (Roentdek, Geramny, DLD80). After the ions traveled the length of the flight tube they interacted with the ion MCP stack. The MCP stack amplified the ion signal in the form

of an electron cascade. The electron cascade was collected on the delay line detector. The initial pulses from the delay line detector were sent to an amplification and discrimination module (DLATR6). From this point the ion stop signals were transmitted in ECL format to a time to digital converter and routed to a Windows based PC. The time to digital converter was the route along the signal path that the electron start and detector stop pulses were converted to time information. The time information corresponding to an event was converted to a two-dimensional image and time of flight spectra by COBALDT 2002 software.

4.3 Results

This results section is centered on the initial goal of verifying all necessary conditions for future work. These items include focusing conditions, mass resolution and demonstrating a lower limit on percent composition detection. First, the focusing voltages were experimentally verified. Second the mass resolution was tested with a mixture of gases. Finally, the detection limits were verified with the use of argon isotopes.

In order to distinguish ions of high kinetic energy from zero energy ions, initial focusing conditions are paramount. A noble gas was ideal to determine the focusing conditions due to the fact that upon ionization no chemical bond was available to "explode", yielding only ions with zero or extremely low initial energies. Initial setup spectra were taken with argon as the sample gas to verify the position of the incident photons through the center of the interaction region. No attempt was made to focus the image. The initial out-of-focus ions can be seen below as a diagonal high intensity region on the detector (Figure 4.8)

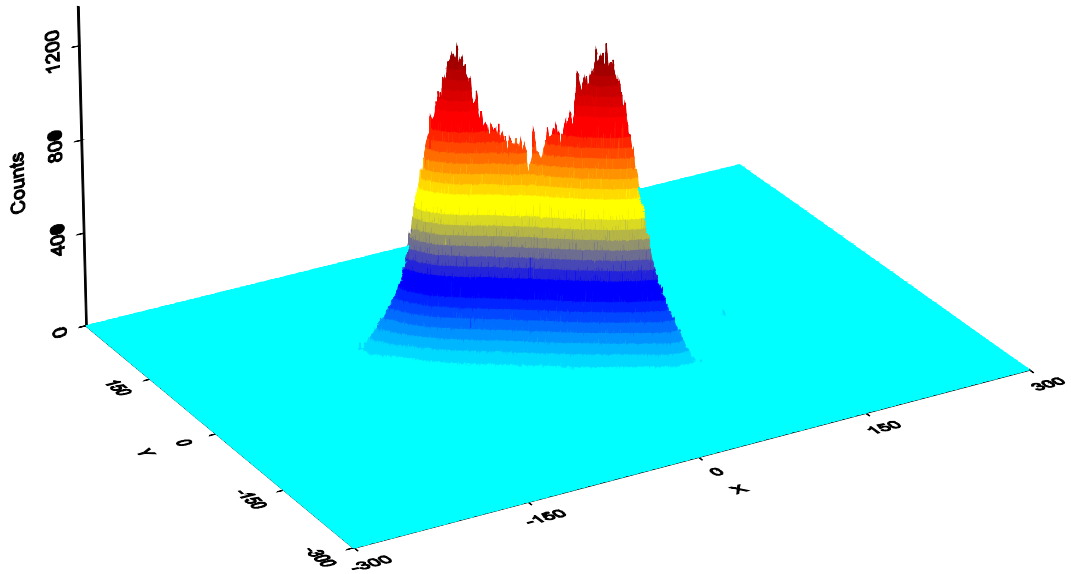

Figure 4.8 An initial out-of-focus image of argon ions is shown. The high intensity region at a diagonal is from the photon beam intersecting the gas sample. The narrow dimension defines the width of the photons.

Although extensive simulations were preformed to determine the proper conditions for focusing, small deviations and unknowns require the simulated focusing conditions to be refined through experimentation. Some examples of possible unknowns are the length of the flight tube (due to small adjustments made for alignment) and the actual voltages applied to the ion optics. Focusing was performed by monitoring the image and slowly raising the negative voltage on the focusing electrode until a minimum spot size was obtained. A focused image is shown below with a total acceleration

potential of 2100 V (Figure 4.9). The voltages for the system are -300 V extractor, -950 V focusing optic and –2400 V for the ion MCPs and flight tube.

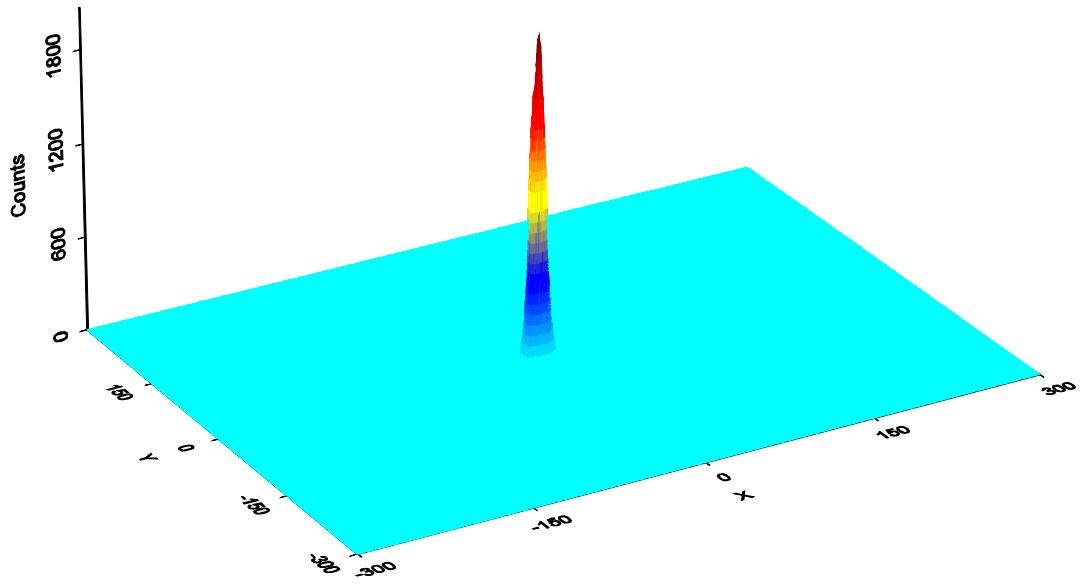

Figure 4.9 A focused ion image of argon ions with total energy of 2100 V.

It is important to note that alterations in the focus voltage do not significantly alter the total energy transferred to the ions. By changing the focus potential the only change is how the voltage is divided between the initial and final optic of the system. It was experimentally determined that a focused image is obtained with a focus potential of –950 V. The theoretical value had been determined to be -940 V.

In order to calibrate the species present in a mixed gas beam, time of flight calibration was necessary. As an image was collected a mass spectrum was collected simultaneously. A mixture of argon and atmospheric nitrogen and oxygen were used for calibration. A sample calibration spectrum is shown in Figure 4.10. The calibration spectrum demonstrates the resolution obtained was acceptable for later studies of complex mixtures. Knowing the principal components and the time of flight allowed for a calibration equation for mass to be determined (Equation 4.4).

$$Mass = \left(\frac{y - 4.0113}{2575.8} \right)^2$$

Equation 4.4 Calibration of mass versus time.

With a focused image and time of flight calibration, determination of detection limits was performed. The initial goal of this study was to detect mixed species in the low percent range (1-4%). Argon was used for the trace analysis as is contains a well-known mixture of natural isotopes. The most abundant isotopes of argon are Ar 40, Ar 38, and Ar 36 with a percent composition of 99.6, 0.337, and 0.063 percent, respectively.[4.22] An expanded argon time of flight spectrum is shown in Figure 4.11. As can clearly be seen from the expanded argon spectrum, the goals of 1-4% mixture detection have been exceeded. Ar 38 is seen as a fully resolved peak and Ar 36 is a shoulder below the main argon isotope.

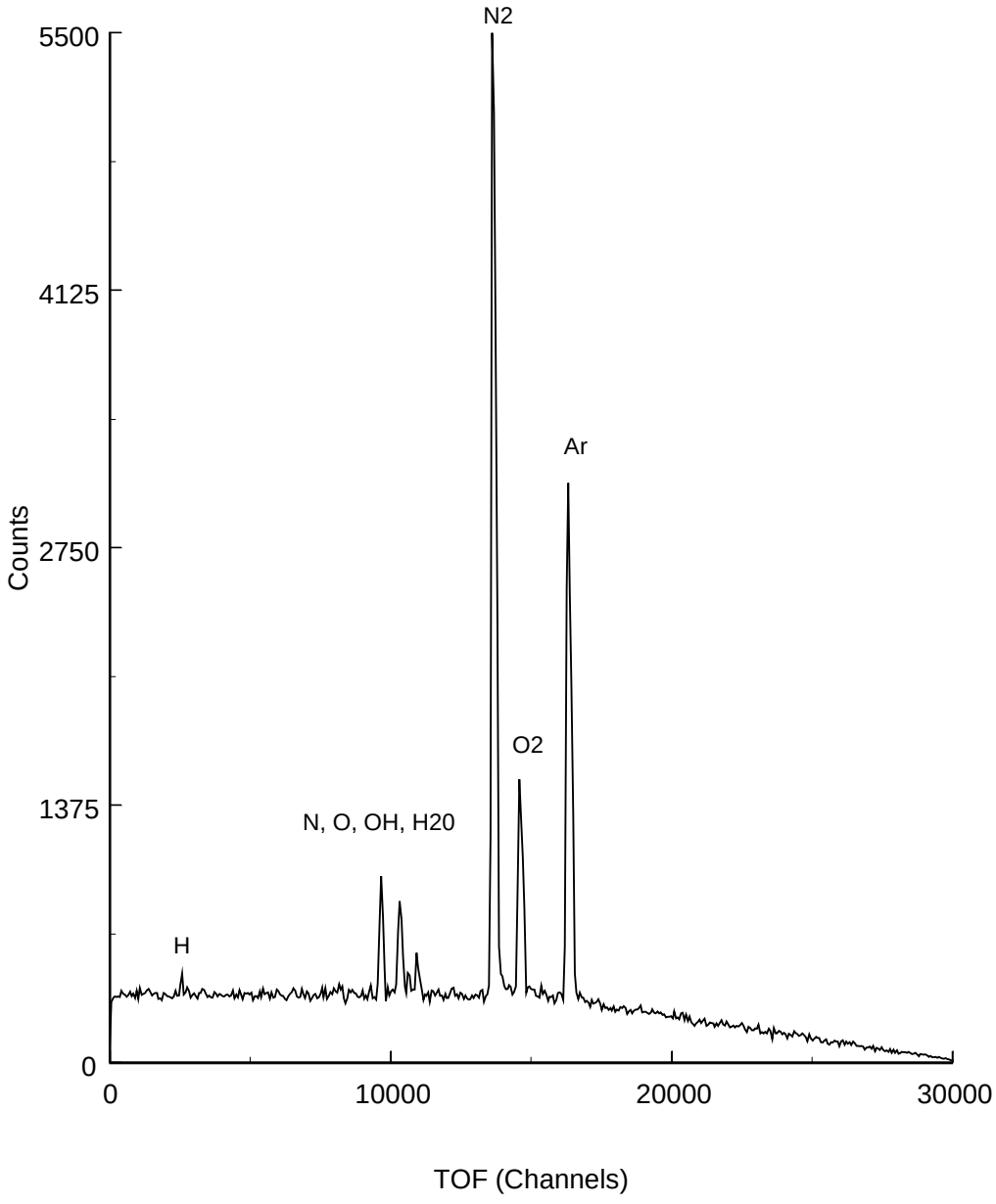

Figure 4.10 Calibration time of flight spectra with Ar, O_2, N_2 and trace atmospheric components. Ionization energy = 17 eV.

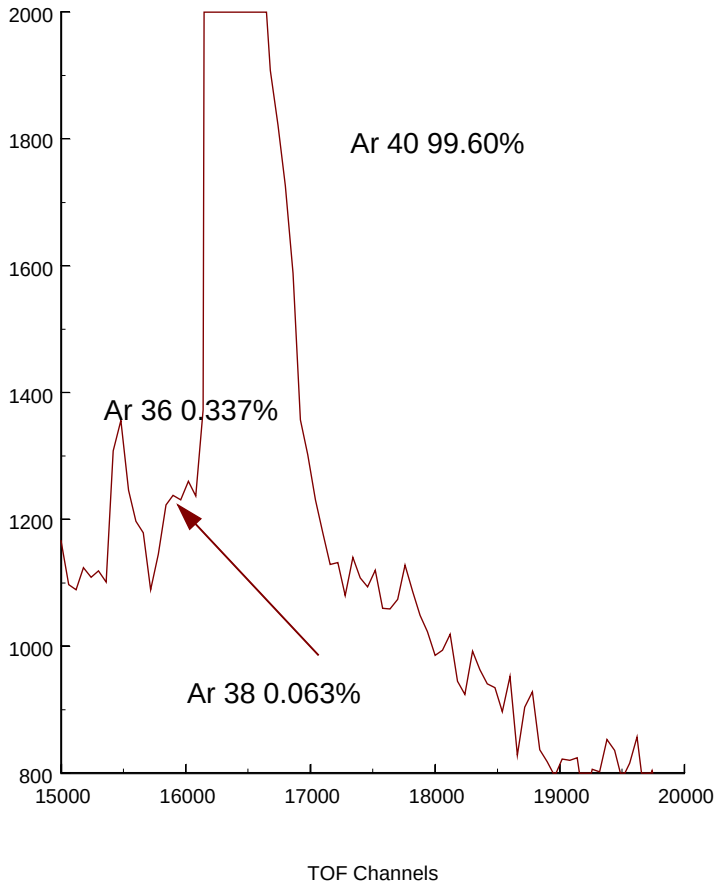

Figure 4.11 Expanded spectrum of argon time of flight showing trace isotopes Ar 38 and Ar 36. Excitation energy =17 eV.

4.4 Future Work

Significant progress has been made in the characterization and calibration of the time of flight and optical components. However, there are several items to be accomplished in order to validate the accuracy of the experimental method. This final section will attempt to cover the most obvious ones with the intent of aiding the next experimentalist. Along with specific troubleshooting issues a few brief thoughts on the future of this project are included.

The issue of troubleshooting is foremost in priority in the list of things that needs to be accomplished. The long term stability of the electronics needs to be resolved as this issue has surfaced in the attempts to calibrate the system. One of the more pressing issues of electronic nature is the effective reduced background in Figure 4.10 after channels 18000. There are two obvious possible explanations for a variable level of background counts: false starts and false stops.

For both false starts and false stops, it is assumed that a high percentage of events are counted accurately. This assumption is based on the fact that excellent signal to noise is achieved. The first possibility, false starts, is described briefly. A false start begins the timer and would not trigger a valid event unless a true event occurred causing a photoion to hit the detector or a false stop occurred. The case of a false stop after a false start should be random in nature and would cause a sloped background only if the false stop frequency was high compared to the total open time of the counter. A true event triggering a stop would tend to add signal to the background beyond the largest peak in the spectrum. This delay is induced by the fact that the flight time of a true event would be the same regardless of whether a true or false start was recorded. In the case where a true event triggered a stop after a false start the time would be the sum of the flight time of the ion and the delay between the false start and the ionization event.

The other possibility is that a true event is started and a false stop terminates the timing. In this case a sloping background would be present. A number of true events would be stopped prematurely yielding a high background in the lower time regions, and this effect would diminish after a valid event stopped the timer. Other possibilities are feasible such as a combination of false starts and stops.

The scientific future of this work resides in the ability to determine zero kinetic energy ions from others. I recommend that to validate the experimental possibilities an experiment be performed on a gas mixture. The basic outline of the proposed experiment is as follows: two gases must be selected, such as CO and CO_2, where the first gas is a fragment of the second. An energy dependent total ion yield experiment would be conducted on the lightest gas and recorded. Next an energy dependent zero kinetic energy scan would be performed on a mixture of the two gases. In this scan the mass selection should be set to the lighter gas and recorded. The energy dependent scan on the mixture would contain CO ions from both CO and CO_2. By extracting the zero kinetic species and comparing the data with that taken with CO alone, the soundness of the technique would be proven. Once the validity of the technique is without doubt, further investigations of other systems may be pursued.

4.5 References

4.1 Ruhl, E.; Heinzel, C.; Hithcock, A. P.; Baumgartel, H. Ar 2p spectroscopy of free argon clusters. *Journal of Chemical Physics* **1993**, *98*, 2653-2663.

4.2 Poliakoff, E. D.; Dehmer, P. M.; Dehmer, J. L.; Stockbauer, R. The photoelectron spectrum of Xe3 by the photoelectron-photoion coincidence technique. *Journal of Chemical Physics* **1981**, *75*, 1568-1569.

4.3 Eppink, A.; Parker, D. Velocity Map imaging of ions and electrons using electrostatic lenses: Application in photoelectron and photofragment ion imaging of molecular oxygen. *Review of Scientific Instruments* **1997**, *68*, 3477-3484.

4.4 Siuzdak, G. *Mass Spectrometry for Biotechnology*; Academic Press: New York, 1996; 161.

4.5 Wiley; McLaren Time of Flight Mass Spectrometer with Improved Resolution. *Review of Scientific Instruments* **1955**, *16*, 1150-1157.

4.6 Cotter, R. Time of flight Mass Spetrometry for the Structural Analysis of Biological Molecules. *Analytical Chemistry* **1992**, *64*, 1027-1039.

4.7 Bruker Daltonics; http://www.Bruker.com, 2003.

4.8 Dempster, A. J. A new method of positive ray analysis. *Physics Review* **1918**, *11*, 316-324.

4.9 Bass, M. J.; Brouard, M.; Clark, A. P.; Vallance, C.; Martinez-Haya, B. Angular momentum alignment of Cl(P-2(3/2)) in the 308 nm photolysis of Cl-2 determined using Fourier moment velocity-map imaging. *Physical Chemistry Chemical Physics* **2003**, *5*, 856-864.

4.10 Bellm, S. M.; Lawrance, W. D. The partitioning of energy amongst vibration, rotation, and translation during the dissociation of p-difluorobenzene-Ar neutral and cation complexes. *Journal of Chemical Physics* **2003**, *118*, 2581-2589.

4.11 Aguirre, F.; Pratt, S. T. Velocity map imaging of the photodissociation of CF3I: Vibrational energy dependence of the recoil anisotropy. *Journal of Chemical Physics* **2003**, *118*, 1175-1183.

4.12 Dinu, L.; Eppink, A.; Rosca-Pruna, F.; Offerhaus, H. L.; van der Zande, W. J. et al. Application of a time-resolved event counting technique in velocity map imaging. *Review of Scientific Instruments* **2002**, *73*, 4206-4213.

4.13 Reichert, E. L.; Thurau, G.; Weisshaar, J. C. Velocity map imaging of ion-molecule reaction products: Co+(F- 3(4))+isobutane. *Journal of Chemical Physics* **2002**, *117*, 653-665.

4.14 Offerhaus, H. L.; Nicole, C.; Lepine, F.; Bordas, C.; Rosca-Pruna, F. et al. A magnifying lens for velocity map imaging of electrons and ions. *Review of Scientific Instruments* **2001**, *72*, 3245-3248.

4.15 Suits, A.; Continetti, R. *Imaging In Chemical dynamics*; Oxford University Press: Washington, 2001; 411.

4.16 Read, F. H. 'Zero Gap' electrostatic aperture lenses. *Journal of Physics E: Scientific Instruments* **1971**, *4*, 562-566.

4.17 Read, F. H. Calculated properties of electrostatic einzel lenses of three aperatures. *Journal of Physics E: Scientific Instruments* **1971**, *2*, 679-684.

4.18 Dahl, D. A.; Delmore, J. E.; Appelhans, A. D. Simion PC/PS2 electrostatic lens design program. *Review of Scientific Instruments* **1990**, *61*, 607-609.

4.19 Braun, M.; Beckert, M.; Muller, U. Novel photofragment spectrometer for the investigation of molecular three-body decay. *Review of Scientific Instruments* **2000**, *71*, 4535-4544.

4.20 Koch, K. D.; Mohan, C. V.; Erskine, J. L.; Sprunger, P. T.; Scott, J. D. CAMD 6-m toroidal grating monochromator beamline. *Nuclear Instruments & Methods in Physics Research Section a- Accelerators Spectrometers Detectors and Associated Equipment* **2002**, *483*, 821-829.

4.21 Mergel, V.; Jagutzki, O.; Spielberger, L.; Ullmann-pfleger, K.; Dorner, R. et al. Particle and UV-imaging with position sensitive MCP-detectors-three-dimensional momentum space imaging. *Materials Research Society*: Boston, MA, 1997.

4.22 *CRC Handbook of Chemistry and Physics*; 73 ed.; CRC Press: Ann Arbor, 1992.

Appendix A: Tabulated Data

G_1

y	$G_1(y)$
0.001	9.599 e-2
0.0010	2.131 e-1
0.0100	4.450 e-1
0.1000	8.182 e-1
0.3000	9.177 e-1
0.5000	8.708 e-1
0.7000	7.879 e-1
1.000	6.514 e-1
1.500	4.506 e-1
2.000	3.016 e-1
3.000	1.286 e-1
4.000	5.283 e-2
5.000	2.125 e-2
7.000	3.308 e-3
10.000	1.922 e-4

Where y= energy/ critical energy

Table adapted from: Attwood, D. *SOFT X-RAYS AND EXTREME ULTRAVIOLET RADIATION*; Cambridge University Press: Cambridge, 2000; 470.

K- and L- edge ionization energies for elements 1-40

Element	K 1s	L_1 2s	L_2 $2p_{1/2}$	L_3 $2p_{3/2}$
1 H	13.6			
2 He	24.6			
3 Li	54.7			
4 Be	111.5			
5 B	188			
6 C	284.2			
7 N	409.9	37.3		
8 O	543.1	41.6		
9 F	696.7			
10 Ne	870.2	48.5	21.7	21.6
11 Na	1070.8	63.5	30.65	30.81
12 Mg	1303.0	88.7	49.78	49.50
13 Al	1559.6	117.8	72.95	72.55
14 Si	1839	149.7	99.82	99.42
15 P	2145.5	189	136	135
16 S	2472	230.9	163.6	162.5
17 Cl	2822.4	270	202	200
18 Ar	3205.9	326.3	250.6	248.4
19 K	3608.4	378.6	297.3	294.6
20 Ca	4038.5	438.4	349.7	346.2
21 Sc	4492	498.0	403.6	398.7
22 Ti	4966	560.9	460.2	453.8
23 V	5465	626.7	519.8	512.1
24 Cr	5989	696.0	583.8	574.1
25 Mn	6539	769.1	649.9	638.7
26 Fe	7112	844.6	719.9	706.8
27 Co	7709	925.1	793.2	778.1
28 Ni	8333	1008.6	870.0	852.7
29 Cu	8979	1096.7	952.3	932.7
30 Zn	9659	1196.2	1044.9	1021.8
31 Ga	10367	1299.0	1143.2	1116.4
32 Ge	11103	1414.6	1248.1	1217.0
33 As	11867	1527.0	1359.1	1323.6
34 Se	12658	1652.0	1474.3	1433.9
35 Br	13474	1782	1596	1550
36 Kr	14326	1921	1730.9	1678.4
37 Rb	15200	2065	1864	1804
38 Sr	16105	2216	2007	1940
39 Y	17038	2373	2156	2080
40 Zr	17998	2532	2307	2223

Values adapted from: Gullikson *X-Ray Data Booklet*; Lawrence Berkeley Nationl Lab: Berkeley, 2001.

Appendix B: Differential Pumping

In order to evaluate the differential pumping used in Chapter two, a diagram of the apparatus is shown below.

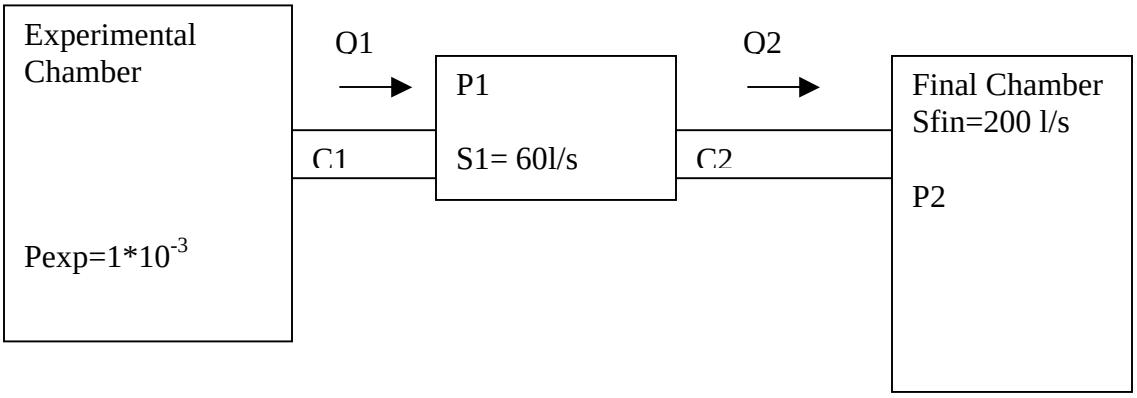

A set of calculations is provided below to show that the experimental pressure differential can be modeled with calculation.

Pressure of experimental chamber (Pexp) =$1*10^{-3}$ torr

Pumping speed of intermediate pump (S1) =60 l/s

Pumping speed of final pump (S2)=200 l/s

Conductance is calculated for the capillary tubes: $C=(12D^3)/L$ in centimeters

Conductance of first capillary (C1)= $(12*(0.2)^3)/40=2.4*10^{-3}$ l/s

Conductance of second capillary (C2)= $(12*(0.2)^3)/30=3.2*10^{-3}$ l/s

Q1/C1=Pexp-P1 and if P1 is low Q1/C1~Pexp

The gas load (Q1) for the intermediate chamber = Pexp * C1= $2.4 * 10^{-6}$

Pressure in the intermediate chamber (P1=Q1/S1)=$4*10^{-8}$

Q2/C2=P1

The gas load (Q2) for the final chamber= P1*C2=$1.3*10^{-10}$

Pressure in the final chamber (P2=Q2/S2)=$6.5*10^{-13}$

Applications of this system yield a final pressure of $1*10^{-9}$. The calculations show that the gas introduced from the experimental chamber is small and has a insignificant effect on the pressure of the final pumping stage. The experimentally determined final pressure is mostly due to degassing from the chamber walls.

Appendix C: Technical Drawings

The following appendix contains the technical drawings that were produced in order to construct the velocity map imaging experiment. Three of the drawings were completed in part or fully by a former graduate student and are included for completeness. For those drawings credit is fully noted in the drawing legend. Below is a photo of the apparatus consisting of all of the technical drawings and electronic components discussed in the text. The photo was taken at CAMD, at the 6-m TGM beamline.

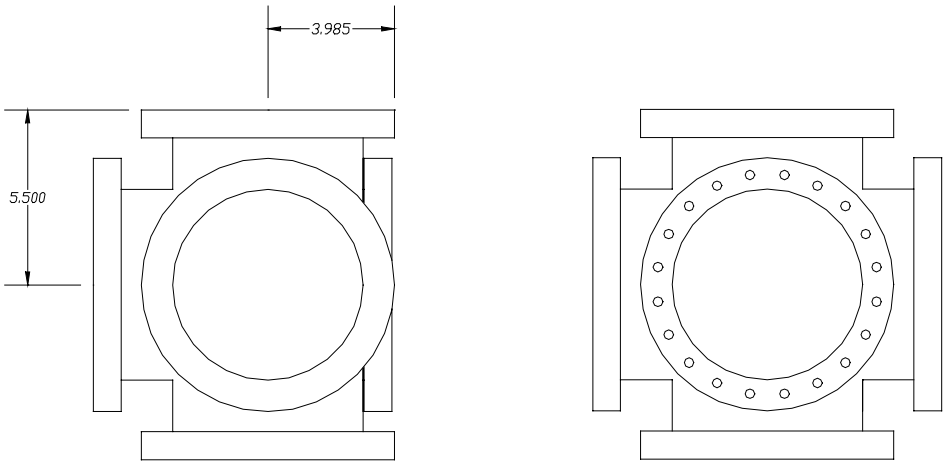

Note: Remove non-rotatable flange and relace with 8" tapped flange to length. Use standard bolt pattern (i.e. split the bolt pattern). All materials will be supplied.

REVISION DATE	
DIMENSIONS ARE IN INCHES DECIMAL TOL: ± .020 FRACTIONAL TOL: ± 1/64 ANGULAR TOL: ± 1/2°	LSU POLIAKOFF LABORATORY
DRAWN BY George Farquar	TITLE 8 IN CROSS
DATE	
SCALE QUARTER	SERIES / DRAWING NUMBER / FILE NAME: 8 in cross
QUANTITY	
MATERIAL SS	

Note: Thickness 3/4, Cut into two parts and tap holes. Up to 1/16" material may be removed for the cut.

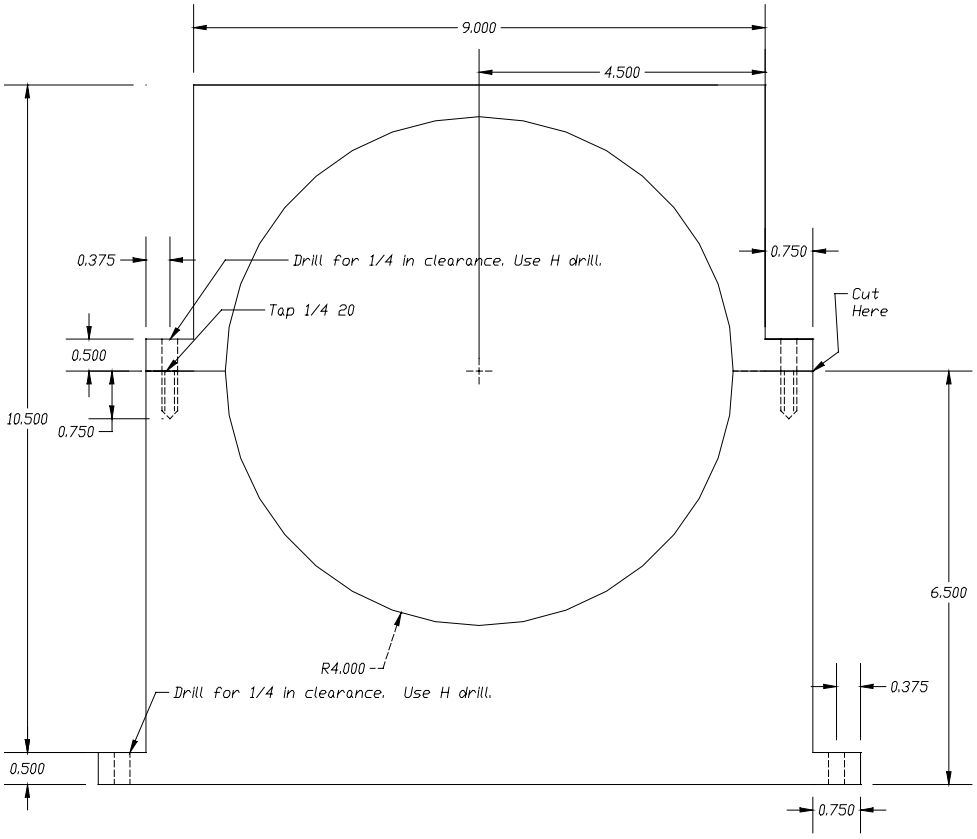

REVISION DATE	
DIMENSIONS ARE IN INCHES DECIMAL TOL: ± .020 FRACTIONAL TOL: ± 1/64 ANGULAR TOL: ± 1/2°	LSU POLIAKOFF LABORATORY
DRAWN BY George Farquar	TITLE: 8 IN CROSS MOUNT
DATE	
SCALE HALF	SERIES / DRAWING NUMBER / FILE NAME: 8 in cross mount
QUANTITY Two	
MATERIAL AL	

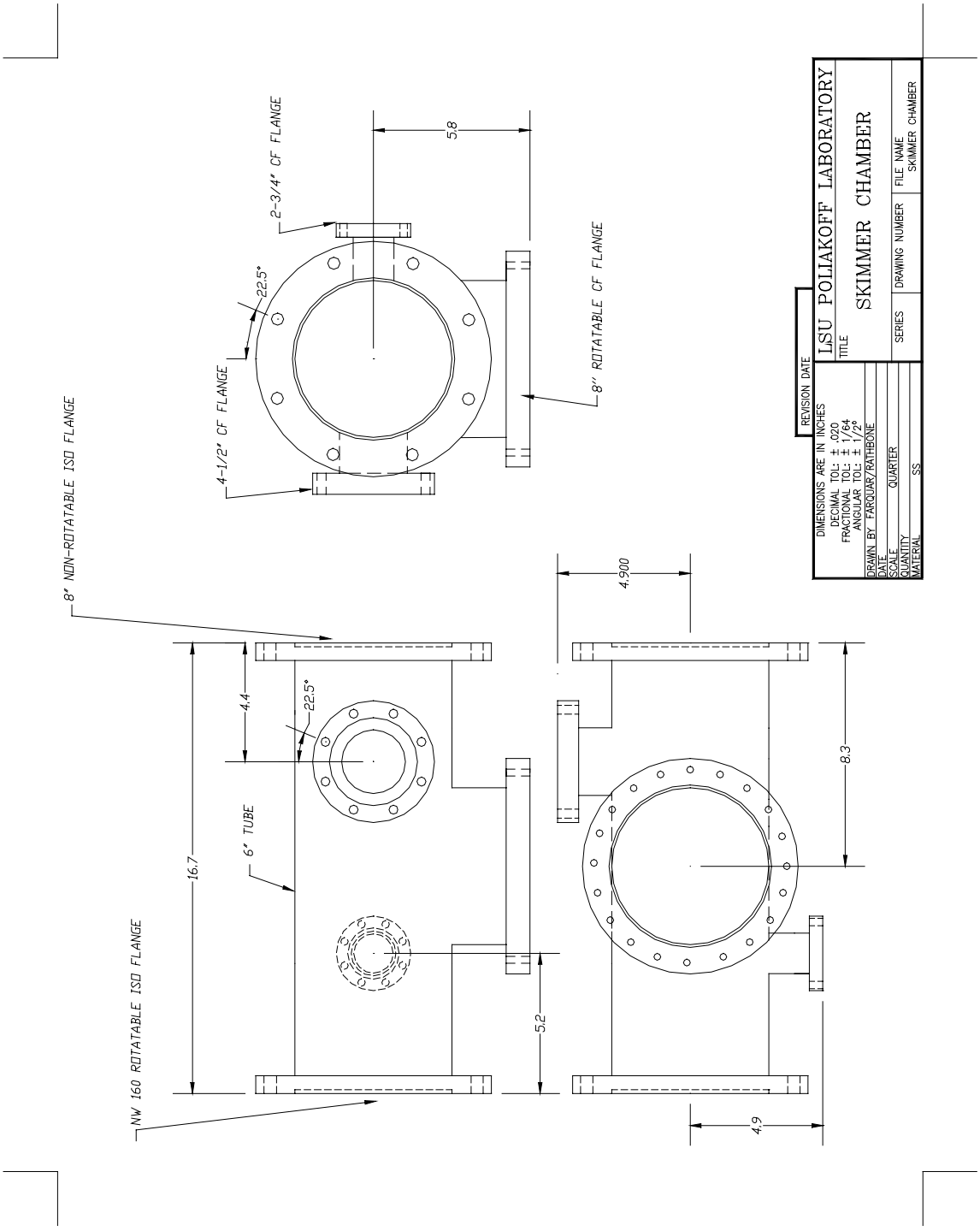
2-3/4" CF FLANGE
5.8
22.5°
4-1/2" CF FLANGE
8" ROTATABLE CF FLANGE
8" NON-ROTATABLE ISO FLANGE
4.900
4.4
22.5°
16.7
6" TUBE
8.3
5.2
NW 160 ROTATABLE ISO FLANGE
4.9
REVISION DATE
DIMENSIONS ARE IN INCHES
DECIMAL TOL: ± .020
FRACTIONAL TOL: ± 1/64
ANGULAR TOL: ± 1/2°
DRAWN BY FARQUAR/RATHBONE
DATE
SCALE QUARTER
QUANTITY
MATERIAL SS
LSU POLIAKOFF LABORATORY
TITLE
SKIMMER CHAMBER
SERIES
DRAWING NUMBER
FILE NAME
SKIMMER CHAMBER

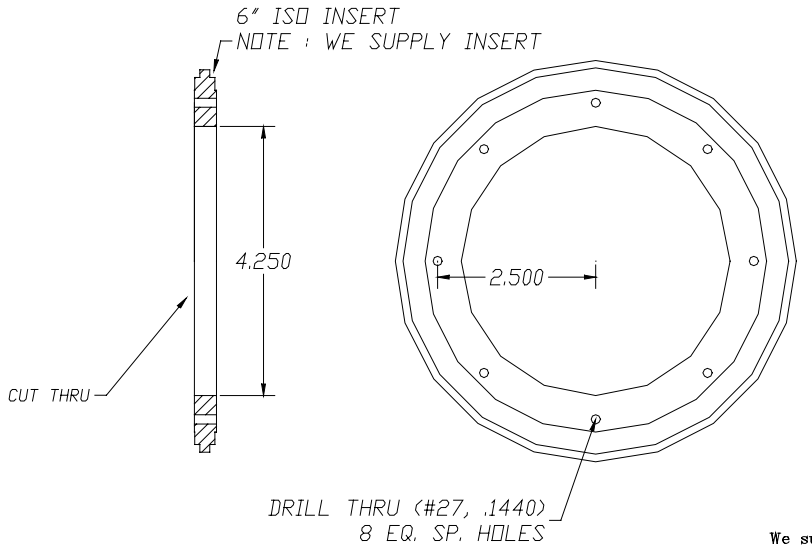

We supply insert
1. Drill through 8 holes on 5 in center
2. Cut out center 4.25 in circle

REVISION DATE	
DIMENSIONS ARE IN INCHES DECIMAL TOL: ± .020 FRACTIONAL TOL: ± 1/64 ANGULAR TOL: ± 1/2°	LSU POLIAKOFF LABORATORY
DRAWN BY GEORGE FARQUAR	TITLE SKIMMER EXT RING
DATE	
SCALE HALF	SERIES / DRAWING NUMBER / FILE NAME: SKIMMER EXT RING
QUANTITY	
MATERIAL SS	

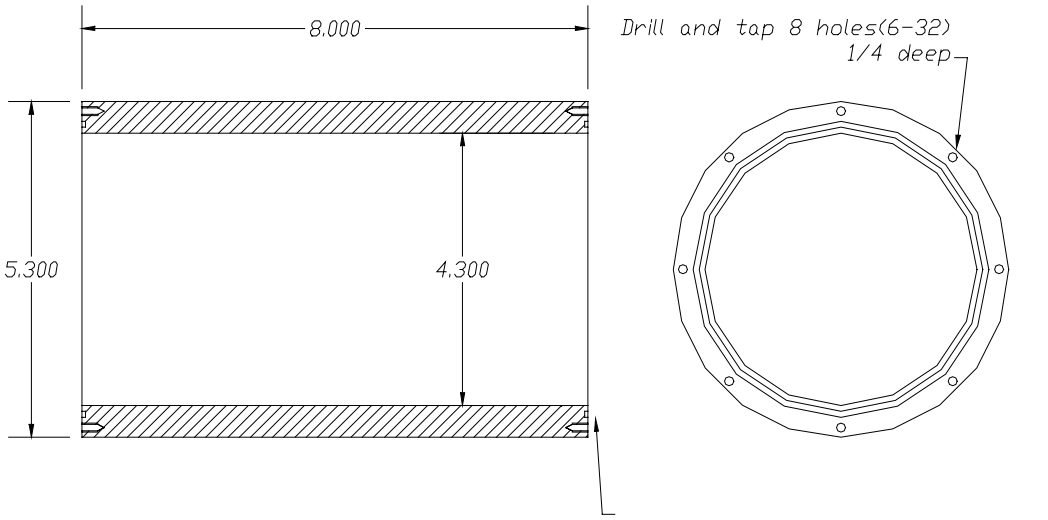

O-RING GROOVE I.D. = 4.489 +-0.005
WIDTH 0.093 +0.005 -0.00
DEPTH 0.052 +- 0.002
PARKER O-RING 2-047

REVISION DATE		
DIMENSIONS ARE IN INCHES DECIMAL TOL: ± .020 FRACTIONAL TOL: ± 1/64 ANGULAR TOL: ± 1/2°	LSU POLIAKOFF LABORATORY	
DRAWN BY George Farquar	TITLE SKIMMER EXTENSION	
DATE		
SCALE HALF		
QUANTITY	SERIES	DRAWING NUMBER
MATERIAL Al		FILE NAME SKIMMER EXTENSION

Note: Thickness 3/4, Cut into two parts and tap holes. Up to 1/16" material may be removed for the cut.

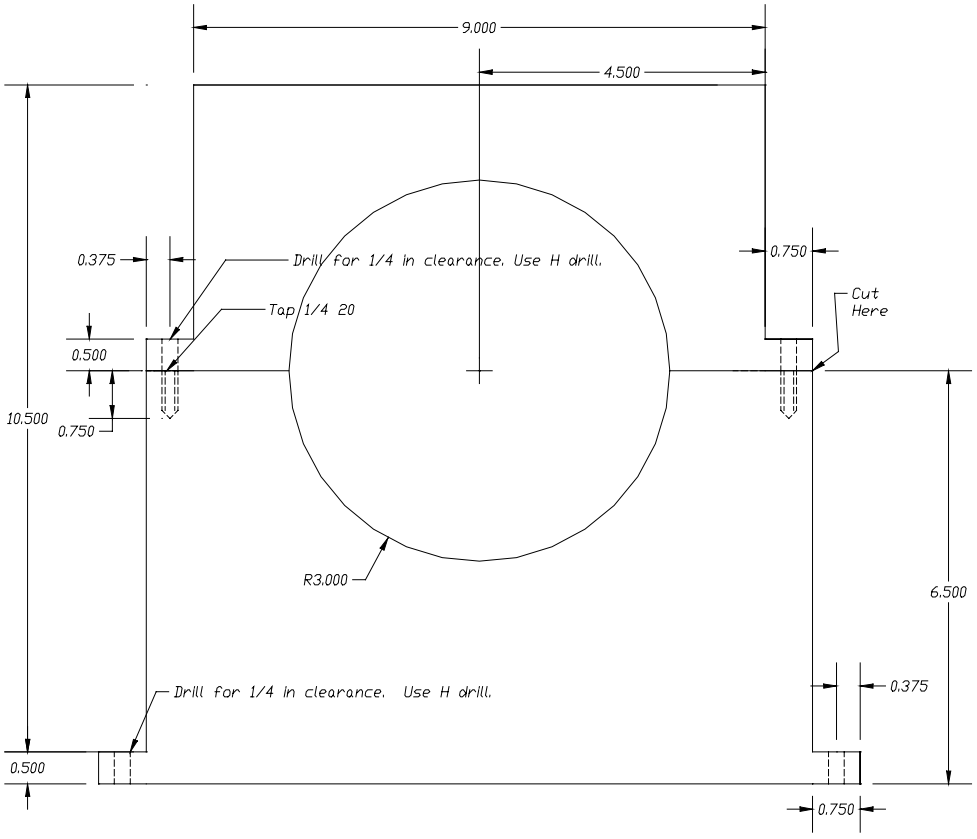

REVISION DATE		
DIMENSIONS ARE IN INCHES DECIMAL TOL: ± .020 FRACTIONAL TOL: ± 1/64 ANGULAR TOL: ± 1/2° DRAWN BY George Farquar DATE SCALE HALF QUANTITY Two MATERIAL Al	LSU POLIAKOFF LABORATORY TITLE SKIMMER CHAMBER MOUNT	
	SERIES	DRAWING NUMBER
		FILE NAME Skimmer mount 6 in

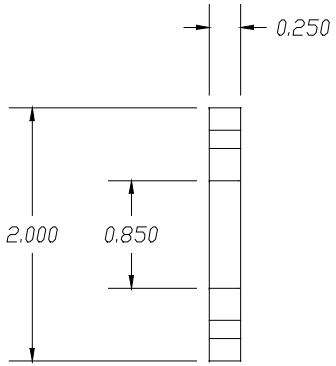

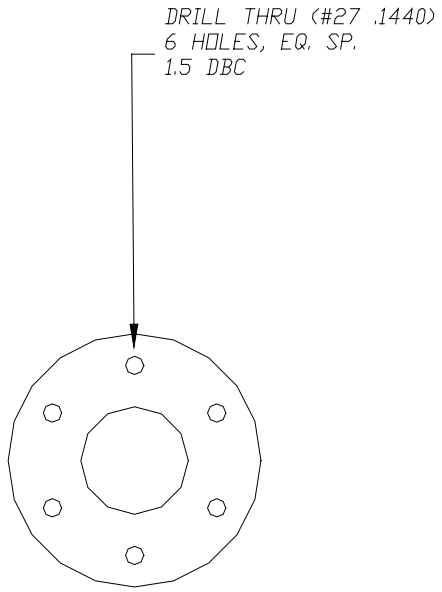

REVISION DATE	
DIMENSIONS ARE IN INCHES DECIMAL TOL: ± .020 FRACTIONAL TOL: ± 1/64 ANGULAR TOL: ± 1/2°	LSU POLIAKOFF LABORATORY
DRAWN BY: Jeff Rathbone DATE: 01/15/01 SCALE: FULL QUANTITY: 1 MATERIAL: 304 SS	TITLE: Skimmer Clamp SERIES / DRAWING NUMBER / FILE NAME: skimmerclamp.dwg

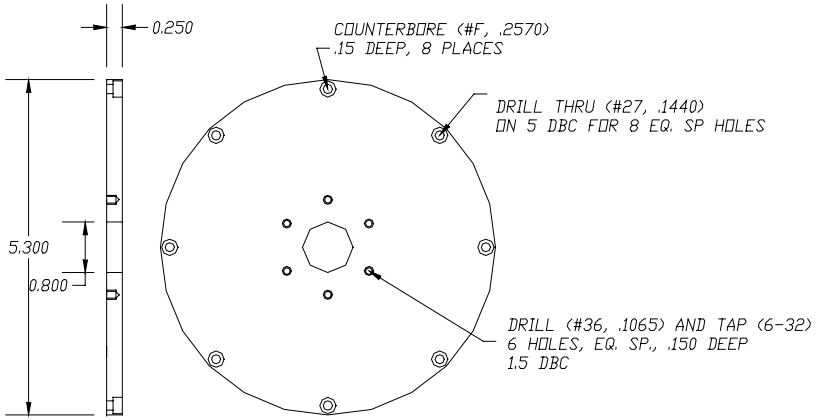

REVISION DATE	
DIMENSIONS ARE IN INCHES DECIMAL TOL: ± .020 FRACTIONAL TOL: ± 1/64 ANGULAR TOL: ± 1/2°	LSU POLIAKOFF LABORATORY
DRAWN BY JEFF RATHBONE	TITLE SKIMMER MOUNTING PLATE
DATE 10/13/01	
SCALE HALF	SERIES / DRAWING NUMBER / FILE NAME
QUANTITY 1	
MATERIAL 304 SS	SKIMMERMOUNT.DWG

NOTE: OUTER AND INNER DIAMATERS ARE FOR SLIP FITTINGS. I.E. 3.75 AND 4.25 TUBES WILL SLIP OVER.

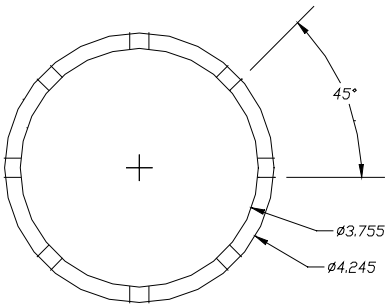

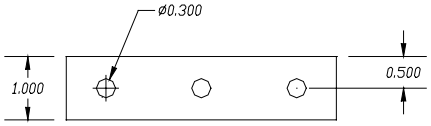

REVISION DATE		
DIMENSIONS ARE IN INCHES DECIMAL TOL: ± .020 FRACTIONAL TOL: ± 1/64 ANGULAR TOL: ± 1/2°	LSU POLIAKOFF LABORATORY	
DRAWN BY George Farquar	TITLE TOF TUBE SPACER	
DATE		
SCALE HALF	SERIES	DRAWING NUMBER
QUANTITY		FILE NAME Teflon Spacer
MATERIAL TEFLON		

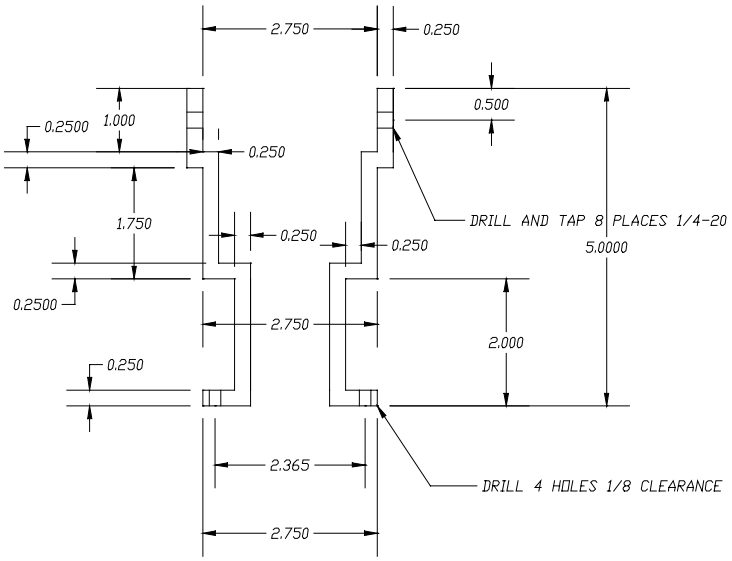

REVISION DATE	
DIMENSIONS ARE IN INCHES DECIMAL TOL: ± .020 FRACTIONAL TOL: ± 1/64 ANGULAR TOL: ± 1/2°	LSU POLIAKOFF LABORATORY
DRAWN BY George Farquar	TITLE TOF BOTTOM
DATE	
SCALE HALF	SERIES / DRAWING NUMBER / FILE NAME: TOF BOTTOM
QUANTITY	
MATERIAL SS	

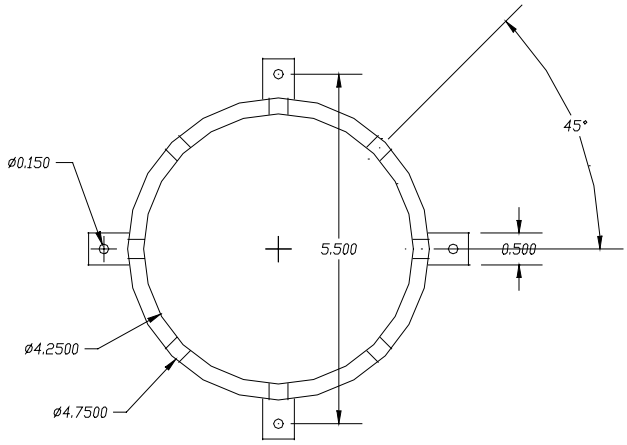

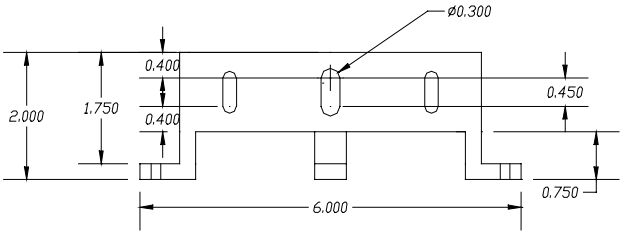

REVISION DATE		
DIMENSIONS ARE IN INCHES DECIMAL TOL: ± .020 FRACTIONAL TOL: ± 1/64 ANGULAR TOL: ± 1/2° DRAWN BY GEORGE FARQUAR DATE SCALE HALF QUANTITY MATERIAL AL	LSU POLIAKOFF LABORATORY TITLE TOF MOUNT	
	SERIES	DRAWING NUMBER / FILE NAME TOF MOUNT

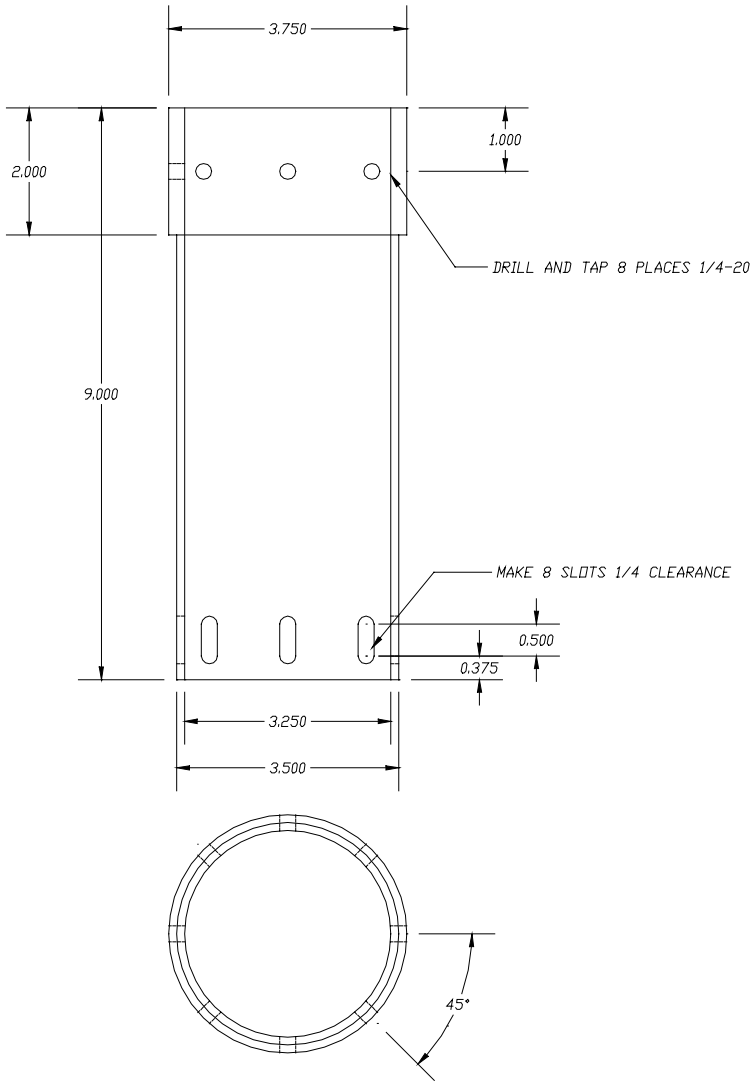

REVISION DATE	
DIMENSIONS ARE IN INCHES DECIMAL TOL: ± .020 FRACTIONAL TOL: ± 1/64 ANGULAR TOL: ± 1/2° DRAWN BY George Farquar DATE SCALE HALF QUANTITY MATERIAL SS	LSU POLIAKOFF LABORATORY TITLE TOF TOP SERIES / DRAWING NUMBER / FILE NAME TOF TOP

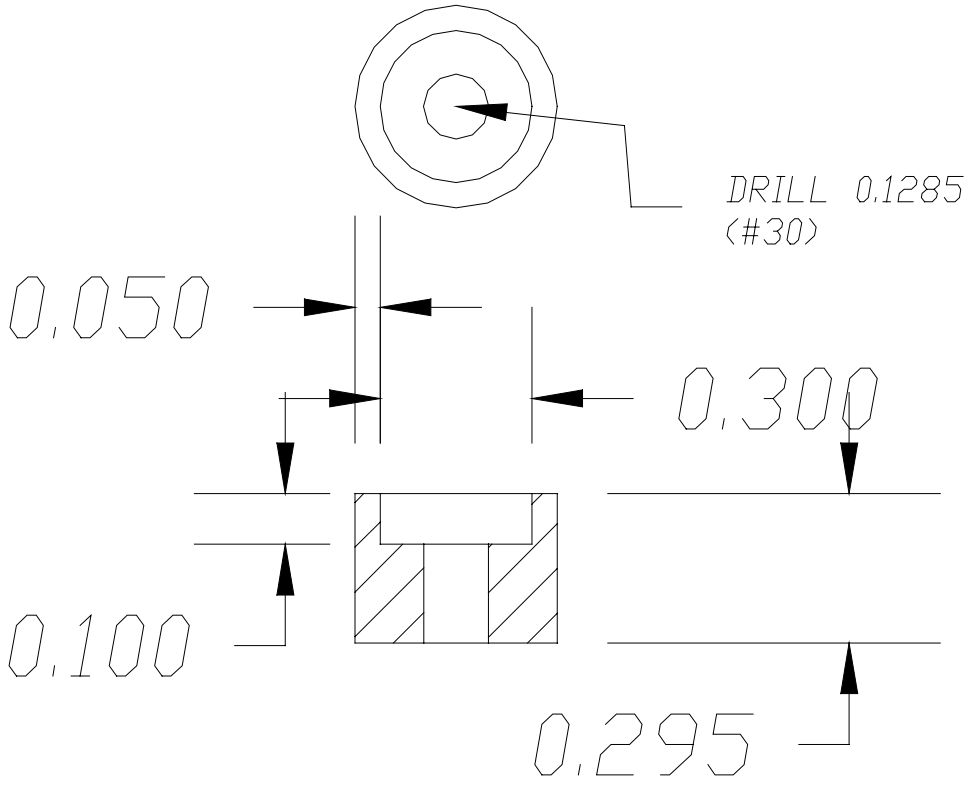

REVISION DATE		
DIMENSIONS ARE IN INCHES DECIMAL TOL: ± .020 FRACTIONAL TOL: ± 1/64 ANGULAR TOL: ± 1/2°	LSU POLIAKOFF LABORATORY	
DRAWN BY: GEORGE FARQUAR	TITLE: VMI FEMALE PLATE SPACER	
DATE:		
SCALE: QUADRUPLE	SERIES	DRAWING NUMBER
QUANTITY:		FILE NAME: VMI FEMALE SPACER
MATERIAL: SS		

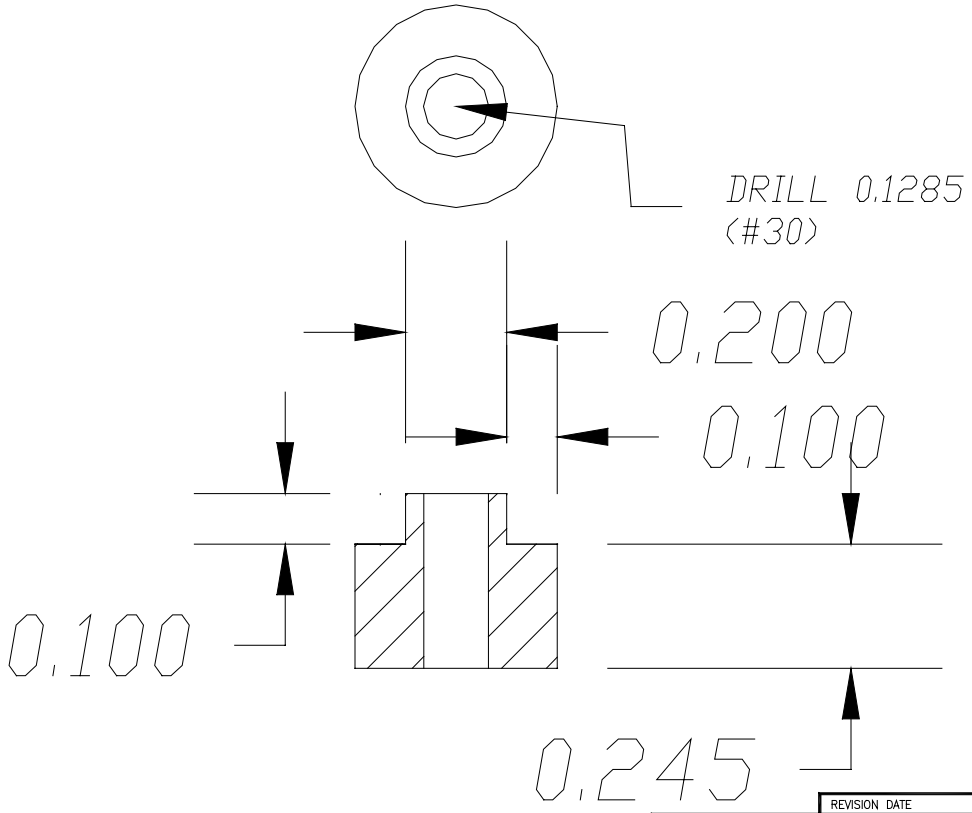

REVISION DATE		
DIMENSIONS ARE IN INCHES DECIMAL TOL: ± .020 FRACTIONAL TOL: ± 1/64 ANGULAR TOL: ± 1/2°	LSU POLIAKOFF LABORATORY	
DRAWN BY GEORGE FARQUAR	TITLE VMI MALE PLATE SPACER	
DATE		
SCALE QUADRUPLE		
QUANTITY		
MATERIAL SS	SERIES	DRAWING NUMBER / FILE NAME: VMI MALE SPACER

NOTE: THICKNESS 2MM

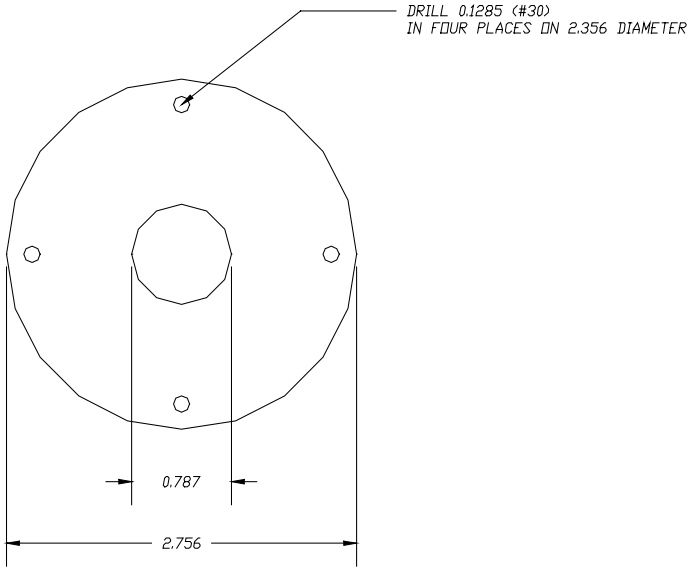

REVISION DATE		
DIMENSIONS ARE IN INCHES DECIMAL TOL: ± .020 FRACTIONAL TOL: ± 1/64 ANGULAR TOL: ± 1/2° DRAWN BY GEORGE FARQUAR DATE SCALE FULL QUANTITY MATERIAL SS	LSU POLIAKOFF LABORATORY TITLE VMI INTERACTION REGION	
	SERIES	DRAWING NUMBER
		FILE NAME VMI OPTICS

Vita

George R. Farquar was born in Sacramento, California, on May 14, 1973. He was raised in Auburn, California. Upon completion of three years of high school he continued on to earn an associates degree in liberal arts from Sierra College in Rocklin, California (1993). While attending Sierra College he was an exchange student at the University of Guadalajara, Mexico. During his studies in Mexico the love of chemistry was rekindled along with a newfound admiration for foreign cultures. After returning home to complete his studies he traveled north to earn a bachelor of science degree in chemistry from Humboldt State University in Arcata, California, in 1997. After graduation he traveled for one cycle of the moon to Baton Rouge, Louisiana, and continued on with his love of foreign cultures. In Louisiana he began pursuing a doctoral degree from Louisiana State University Agricultural and Mechanical College. In Baton Rouge he married Hannah D. Andrepont.

George Farquar has decided to continue on with his quest for education beyond the confines of Louisiana. The degree of Doctor of Philosophy will be conferred at the 2003 December Commencement.